POSTSEISMIC RESPONSE FOLLOWING THE 2012 M_W 7.6 NICOYA, COSTA RICA EARTHQUAKE

A Dissertation
Presented to
The Academic Faculty

By

Tiegan E. Hobbs

In Partial Fulfillment
of the Requirements for the Degree
Doctor of Philosophy in the
School of Earth and Atmospheric Sciences

Georgia Institute of Technology

May 2019

POSTSEISMIC RESPONSE FOLLOWING THE 2012 M_W 7.6 NICOYA, COSTA RICA EARTHQUAKE

Approved by:

Dr. Andrew Newman, Advisor
School of Earth and Atmospheric Sciences
Georgia Institute of Technology

Dr. Zhigang Peng
School of Earth and Atmospheric Sciences
Georgia Institute of Technology

Dr. J. David Frost
School of Civil and Environmental Engineering
Georgia Institute of Technology

Dr. Marino Protti
Observatorio Volcanologico y Sismologico de Costa Rica
Universidad Nacional de Costa Rica

Dr. Timothy Dixon
School of Geosciences
University of South Florida

Date Approved: March 8, 2019

"[A]lthough seismology provides a great deal of detail about the slip that occurs during an earthquake, we still have only general ideas about how earthquakes are related to tectonics, little understanding of the actual faulting process, no ability to predict earthquakes on time scales shorter than a hundred years, and only rudimentary methods to estimate earthquake hazards ... Our best response seems to be to show humility in face of the complexity of nature, recognize what we presently know and what we do not, use statistical techniques to assess what what we can say with differing degrees of confidence from the data, and develop new data and techniques to do better."

Seth Stein & Michael Wysession

An Introduction to Seismology, Earthquakes, and Earth Structure

For Mickey, Brittany, and Tylor Hobbs

ACKNOWLEDGEMENTS

My time at Georgia Tech has been incredibly rewarding, due primarily to the exceptional people I have had the pleasure of working with. I would like to firstly thank Dr. Andrew Newman, my thesis supervisor, for his expertise, support, and for constantly challenging me to be better. Specifically, I am thankful for his trust in me, and for the opportunity to learn how to lead. I would also like to thank Drs. Zhigang Peng and J. David Frost for their time and their willingness to teach me something new. I am grateful to Dr. Tim Dixon for his attention to this dissertation. I would like to thank Dr. Marino Protti for sharing his knowledge and wisdom with me, and for teaching me to do the famous 'Marino pose'. To everyone who I have had the privilege to conduct field work with: I thank you for your good humor, your tireless efforts, and your rigorous attention to detail. And to the beautiful country of Costa Rica: gracias por todas las lindas puestas de sol que me regalaste.

I would also like to thank the friends I have made during my tenure at Tech. Amy Williamson, I am so grateful to have gotten to know you. Thank you for your encouragement, your friendship, your accompaniment all the way to the front row of a lecture, for all the laughs, for all the lunges, and for the time you stole my textbooks before my comprehensive exam. I am deeply appreciative to Jacob Buffo, for everything. Specifically, thank you for the Type II fun and all our dumb ideas. To Meaghan Roberts, thank you for your intense brand of friendship, your frankness, and your unwavering support. I am thankful to Lucas Liuzzo for always being on my team, and also for our late night Matlab sessions and his infamous antics. Justin Lawrence, thank you for all of the cheese and the Antarctic Ambulance. Louisa Barama, I am in awe of how a human can be so close to perfect. To Gabe, Chastity, George, Dongdong, Chenyu, Zach, Amelia, Miguel, Elizabeth, and JMin: Thank you for for making grad school such a fun, supportive environment. I would also like to thank Ryan Cahalan, Katy Bernazal, Emily Saad, and John Charbonneau for their

friendship, for the 2 year Christmas, and for the nerf gun fights. To the AACSE Team and the Sikuliaq Crew: thank you for letting me be a sailor. To Britney Schmidt, Matt Meister, the Icefin team: thank you for letting me be an engineer. To all the folks in McMurdo: thank you and stay frosty.

Finally, I would never have made it to this point without my family and friends outside of Atlanta. Thank you to the friends who always took my calls and who shared their time with me so freely. To my mom and stepdad, for supporting me every step of the way. To my sister, for always being my person, and to baby Kora in her NASA socks. To my brothers, who have the biggest hearts. To my dad, who I wish could've been here to see this. To my extended family, who are too numerous to name, I thank you for your support and for your love. FU4L. Especially, I would like to thank Barbara Hobbs for being the matriarch of a wonderful family — full to bursting with other incredible women and also incredible fellows.

TABLE OF CONTENTS

Acknowledgments v

List of Tables xii

List of Figures xiii

List of Acronyms xxvi

Chapter 1: Introduction and Background 1

1.1 Great Earthquakes 1

1.2 Understanding Subduction Physics through the Seismic Cycle 3

1.3 The Nicoya Peninsula as a Natural Laboratory 5

1.3.1 Tectonic Setting 5

1.3.2 The Nicoya Megathrust 6

1.3.3 The 2012 Moment Magnitude (M_w) 7.6 Earthquake 7

1.4 Outstanding Questions 9

1.4.1 Seismic Data 11

1.4.2 Aftershock Detection 11

1.4.3 Geodetic Data 12

1.4.4 Geodetic Inversion 14

1.5 Outline 15

Chapter 2: Large and primarily updip afterslip following the 2012 M_w 7.6 Nicoya, Costa Rica earthquake 31

2.1 Key Points 31

2.2 Abstract 31

2.3 Introduction 32

2.4 Methods 34

2.4.1 Data Collection 34

2.4.2 Afterslip Inversion 36

2.5 Results & Discussion 40

2.5.1 Surface Displacements 40

2.5.2 Afterslip Inversion 41

2.5.3 Comparison to Aftershocks 42

2.5.4 Comparison to Inter- and Coseismic Slip 44

2.5.5 Comparison to Slow Slip 45

2.5.6 Potential Anelastic Contributions 46

2.5.7 Spatially Variable Fault Behavior on the Nicoya Megathrust 47

2.5.8 Continuing Postseismic Deformation 49

2.6 Conclusions 50

2.7 Acknowledgement 51

Chapter 3: Enigmatic Upper-Plate Sliver Transport Paused by Megathrust Earthquake and Afterslip 63

3.1 Highlights 63

3.2 Abstract 63
3.3 Introduction 64
3.4 Methods 65
3.4.1 Global Navigation Satellite System (GNSS) Velocities 65
3.4.2 Backslip Inversion for Megathrust Locking 66
3.5 Results 68
3.5.1 Relocking Period Features Unexpected Trench Parallel Motions . . 68
3.5.2 Relocking in Two Phases 68
3.6 Discussion 69
3.6.1 Relocking Timeline 69
3.6.2 Novel Observation of Variable Trench-parallel Velocity 70
3.6.3 Tectonic Drivers 73
3.7 Conclusions 74
3.8 Acknowledgements 75

Chapter 4: Defining the Temporal Relationship Between Afterslip and Aftershocks Using Dense Seismic and Geodetic Networks in Nicoya, Costa Rica 79

4.1 Abstract 79
4.2 Introduction 80
4.3 Methods 83
4.3.1 Geodesy: GPS Timeseries Analysis and Slip Inversion 83
4.3.2 Seismology: Aftershock Detection 87
4.4 Results 89

4.4.1 Evaluation of New Interpolation Method 89
4.4.2 Progression of Afterslip & Relocking 90
4.4.3 Aftershocks & Repeaters 91
4.4.4 Afterslip & Aftershocks 92
4.5 Discussion 92
4.5.1 GPS Network Design 92
4.5.2 Anticorrelation of Afterslip and Repeating Aftershocks 93
4.5.3 Megathrust Stress and b-value 94
4.5.4 Aftershock and Afterslip Forecasts Need Interface Mapping 95
4.6 Conclusion 97
4.7 Acknowledgements 98

Chapter 5: Conclusion 112

5.1 Primary Findings 112
5.2 Impact 114
5.2.1 Megathrust Behavior Driven By Physical Properties of Interface . . 114
5.2.2 Asperities Remain Through Multiple Seismic Cycles 115
5.2.3 Repeating Aftershocks Do Not Match Afterslip 116
5.2.4 Sliver Motion is Not Constant 116
5.2.5 Afterslip and Sliver Transient Refute Tectonic Escape Model of Central American Tectonics 117
5.3 Future Research and Outstanding Questions 117
5.3.1 B-value Mapping with the Nicoya Aftershock Catalog 118
5.3.2 Consideration of the Effect of Hurricane Season on Aftershocks . . 118

5.3.3 Evaluate Potential Relationship Between Obliquity of Subduction Zones and Geodetic Locking 119

5.3.4 Look for Transient Sliver Motion at Other Subduction Zones 120

5.3.5 Continue Evaluating Repeating Aftershock Slip Against Geodetic Slip 120

Appendix A: Supplement to Chapter 2: "Large and primarily updip afterslip following the 2012 M_w 7.6 Nicoya, Costa Rica earthquake" 123

Appendix B: Supplement to Chapter 3: "Enigmatic Upper-Plate Sliver Transport Paused by Megathrust Earthquake and Afterslip" 127

References 157

Vita 158

LIST OF TABLES

1.1 Seismic stations in the Nicoya Peninsula Network (YZ) in 2013. 29

1.2 Global Positioning System (GPS) stations in the Nicoya Peninsula Network between 2012 and 2017. Does not include Fault Transect described in Section 1.3.1, or Arenal Volcano Network. 30

2.1 Displacements and errors from 2012 to 2015 at Campaign and Continuous GPS stations used in this study. Dates in decimal years, displacements relative to stable Caribbean plate. 61

2.2 Displacements and errors from 2015 to 2016 at Campaign and Continuous GPS stations used in this study. Dates in decimal years, displacements relative to stable Caribbean plate. 62

4.1 Goodness of Fit Evaluation for Gnuplot Fitting Algorithm 111

B.1 All stations used in this study. Information is provided about the location, operating mode, number of days of data used, and regional grouping of each station. 139

B.2 Average trench-parallel velocities across network for 6 representative times described in text and illustrated in Figures 3.1, 3.2, B.3, and B.4. 140

LIST OF FIGURES

1.1 Figure reproduced from Stein and Wysession (2003). Normalized total slip, as distributed across an idealized, vertical strike slip fault. Interseismic strain accumulates across the locked fault at '0' on the x-axis, as a result of far-field motion. Coseismic slip is focused close to the fault, relieving the interseismic stress accumulation, such that the total slip is equal at all distances from the fault after a full seismic cycle. 17

1.2 Figure reproduced from Wang, Hu, and He (2012). Surface deformations of the postseismic period, with reference to the region of the subduction zone in which they are generated. Immediately after the mainshock, (1) afterslip starts driving wholesale seaward motion at the surface. (2) Viscoelastic relaxation has opposing motions, with coastal sites being the first to show landward motion. (3) Relocking, ultimately, drives all surface deformations in a landward direction. 18

1.3 A schematic image showing surface displacements, or positions, through the seismic cycle. The effect of including postseismic behavior is illustrated as the difference in displacement at time 't', as well as the relative amount of total interseismic strain accumulation that would be inferred at that time (inset). 19

1.4 Nicoya Peninsula study area in northern Costa Rica. Cocos Plate subducts beneath the Caribbean Plate along the Middle America Trench (MAT) at 82 mm/yr (DeMets, Gordon, and Argus 2010), shown by 'CO-CA' convergence vectors. Previously estimated sliver transport rate of 11 mm/yr (Feng et al. 2012) shown as small blue arrow on green 'Trench Parallel' vector, with 'Trench Normal' in purple. East Pacific Rise (EPR) and Cocos-Nazca Spreading Center (CNS) crustal provenance differentiated by dashed black line. Relevant prior seismicity indicated by beach balls, with epicenters indicated by stars (see Feng et al. 2012, and references therein). Black star corresponds to the initial 2012 hypocenter (Yue et al. 2013). Coseismic slip for the 2012 event, in smoothed 1 m increments, shown in blue contours over the central Nicoya Peninsula (Kyriakopoulos and Newman 2016). Volcanoes shown as red triangles. Best estimates of the faults delineating the back of the Central American Forearc (Kyriakopoulos and Newman 2016; Montero, Lewis, and Araya 2017) indicated by coarse dashed lines: Haciendas-Chiripa Fault System (HCFS - blue), Candelaria Fault (CF - pink) and a hypothesized connector ('?' - black). Newly erected GPS transect of that connector shown as purple squares. Seafloor bathymetry and crustal topography shaded in grey (Ryan et al. 2009). 20

1.5 Figure reproduced from Kyriakopoulos et al. (2015). West-looking view of the three dimensional (3D) megathrust geometry for the Nicoya Peninsula portion of the Middle America Trench, determined using the Maximum Seismicity Method. Coastlines and country boundaries shown as red lines. Noticeable change in subduction angle between the more steeply-dipping EPR sourced crust in the north (right side of this image) and the more shallow CNS sourced crust in the south (left side). 21

1.6 Figure reproduced from Kobayashi et al. (2014). Red vectors are resultant motions from a tectonic escape model for Central American Forearc (CAFA) motion. Panama Block (PB) also shows outward motion, with a backstop from the North Andes (ND) block. Also pictures are the North American (NA), Caribbean (CA), Nazca (NZ), and Choco (CH) plates. White arrows show the dominant forces suggested to be controlling motion within this system. 22

1.7 Map of GPS (white/grey) and seismic (green) network in Nicoya, Costa Rica. MAT shown as black line with triangles, volcanos shown as red triangles. Arenal Volcano is labelled, as it is the site of a small network of 5 GPS. 'NP' is the Nicoya Peninsula and 'GN' indicates the Gulf of Nicoya. . 23

1.8 Typical seismic station configuration with buried sensor vault. (a) shows entire site whereas (b) is a zoomed in view of seismic box showing components. Seismic sensor is connected to datalogger by wiring run through a PVC pipe. Timing uses GPS clock. Data are telemetered directly to Observatorio Vulcanológico y Sismológico de Costa Rica (OVSICORI). System is powered by solar panel and batteries, run through a solar controller. 24

1.9 Schematic illustration of the Waveform Matched Filter (WMF) technique. Template events are used to detect other earthquakes from within a continuous waveform, using cross correlation. When the cross correlation coefficient is very high the events are said to be repeating events, sharing a common source and path to generate an almost identical waveform. 25

1.10 Typical campaign GPS occupation. Antenna is fixed to monument pin via metal frame, which is leveled and weighted. Coaxial cable attaches antenna to receiver, which is in turn linked to controller. Power system, which is run through the controller, also includes a single battery and flexible solar panel staked into the soil. Temporary fencing shown in background. 26

1.11 Typical joint continuous GPS and seismic station configuration. (a) shows entire site with solar panels, buried seismic sensor vault and adjacent domed GPS antenna structure. (b) is a zoomed in view of operations box showing components. Seismic sensor is connected to datalogger and GPS antenna is connected to its receiver by wiring run through a PVC pipe. Timing uses GPS clock. Data are telemetered directly to OVSICORI. System is powered by solar panel and batteries, run through a controller. 27

1.12 Schematic image illustrating the concept of inversion. Whereas forward modeling uses parameters and a model (Green's functions) to synthesize data, inversion uses data and an inverted model to uniquely determine the parameters necessary to have created that data. 28

2.1 Tectonic configuration of Nicoya study area, with Cocos Plate subducting beneath Caribbean Plate along the MAT in azimuth shown at a rate of 7.7 cm per year [DeMets et al., 2010]. Transition is shown from oceanic crust sourced at the EPR and CNS (Barckhausen et al. 2001). At this location there is a transition from steep subduction of relatively cold EPR crust to the more shallowly downgoing and warmer CNS crust. Cumulative slow slip contours of Dixon et al. (2014) shown from blue to pink in 100 cm intervals. Centroid (Ekström, Nettles, and Dziewoński 2012) and relocated hypocenter (Yue et al. 2013) for 2012 M_w 7.6 Nicoya earthquake shown by pink and black stars, respectively. The 1990 M_w 7.0 Gulf of Nicoya earthquake (Protti et al. 1995) shown in green, and 1978 M_w 7.0 Samara earthquake (International Seismological Centre 2014) shown in blue. Global centroid-moment tensor solutions (Ekström, Nettles, and Dziewoński 2012) shown by beachballs, scaled by magnitude. Fisher Seamount Chain can be seen from bathymetry beneath the word 'convergence', heading toward the southern tip of the Nicoya peninsula. 52

2.2 Displacement, relative to Caribbean plate, at campaign (orange) and continuous (yellow) GPS sites for 2012-2015 (a) and 2015-2016 (b). Horizontal displacements in black, upwards in red, and downwards in blue. Shown are the 22 available campaign measurements from 2012-2015, compared to only 7 campaign sites successfully occupied in 2016. 53

2.3 Displacement [meters] relative to the first day after the 2012 earthquake for a subset of continuous GPS stations having good temporal coverage. All offsets are given for a fixed Caribbean reference frame. Stations are arranged (left to right, starting from top row and working down) by distance from the trench. North, east, and vertical components are displayed in black, blue, and green, respectively. Postseismic daily displacements are large at first, diminishing with time, and ultimately reversing by approximately the start of 2015. Potential Slow Slip Events (SSEs) are visible as short-term reversals in direction of motion. 54

2.4 Results of checkerboard recoverability testing for input model (a) and resultant slip (b) using preferred smoothing value ($\kappa = 9000$). Depth contours are overlain in blue over input slip panel. Output slip panel shows annotated contours of resolvability (in km) as well as a dark purple, angular polygon surrounding area for which there is good recoverability based on checkerboard test. For more information about resolution and recoverability tests please see Section 2.4.2. EPR-CNS suture shown as dashed line, MAT as solid line with teeth. 55

2.5 Roughness versus misfit for inversion of 2012-2015 GPS displacements. Preferred solution of κ = 9000 indicated by purple star. Blue stars indicate under- and oversmoothed solutions of κ = 4000 and 18000. Resulting maps of afterslip are shown as insets. From left to right they represent oversmoothed, preferred, and undersmoothed results. 56

2.6 GPS displacements for 2012-2015 time period, shown for comparison against model predictions for preferred slip result with free surface. Observations shown by colored arrows, with predictions indicated by black arrows. Left panel shows horizontal displacement, right shows vertical. Dashed line in right panel shows modeled zero vertical deformation, separating uplift from subsidence. 57

2.7 Both panels show result of 2012-2015 inversion where slip is allowed at the trench (non-fixed surface). Magnitude of total postseismic slip on the subduction interface is scaled by color, with arrows showing direction of hanging wall motion at each patch. White lines show 50 cm contours of slip. Thick black line with teeth marks the MAT, while thin grey lines show depth in 10 km intervals (Kyriakopoulos et al. 2015). Dashed line shows EPR-CNS transition (Barckhausen et al. 2001). Purple polygon denotes zone of recoverability, outside of which we are unable to resolve structures uniquely. (a) Aftershocks until end of 2012 shown as grey dots, with purple stars representing locations of repeating aftershock clusters (Yao et al. 2017). (b) 2012 coseismic slip contours shown in pink (every 100 cm), with percentage of pre-2012 locking annotated and shown in green (20% intervals, starting at 50%) (Kyriakopoulos and Newman 2016). 58

2.8 Same as for Figure 2.7, except with inversion not allowing slip to rupture the trench (fixed surface). Again, slip on the subduction interface is scaled by color, with arrows showing direction of hanging wall motion at each patch. White lines show 50 cm contours of slip. Purple polygon denotes zone of recoverability, outside of which we are unable to resolve structures uniquely. (a) Aftershocks until end of 2012 shown as grey dots, with purple stars representing locations of repeating aftershock clusters (Yao et al. 2017). (b) 2012 coseismic slip contours shown in pink (every 100 cm), with percentage of pre-2012 locking annotated and shown in green (20% intervals, starting at 50%) (Kyriakopoulos and Newman 2016). 59

2.9 Slip deficit as difference between interseismic locking, coseismic slip, and afterslip. Interseismic slip accumulation is calculated as percentage of interseismic locking (Kyriakopoulos and Newman 2016) multiplied by the full tectonic convergence rate over 62 years. Afterslip is from non-fixed surface model. Negative slip deficit represents slip overshoot. Overlain are aftershocks (grey dots) and repeating events (purple stars) from Figures 2.7a and 2.8a (Yao et al. 2017). Pink polygon shows the region of significant stored strain near the elbow in the coastline, as discussed in Section 2.5.4. Purple polygon shows area of recoverability, dashed black line is EPR-CNS transition from (Barckhausen et al. 2001), and thick black line with teeth marks the MAT. 60

3.1 Surface velocities, in stable Caribbean reference frame, are calculated for a one year period following the time shown at the top left of each panel. Network averaged trench-parallel (TP) motion indicated in bottom right corner of each panel, but not removed from Global Navigational Satellite System (GNSS) velocities. Haciendas-Chiripa Fault System (HCFS) shown as dashed blue line (Kyriakopoulos and Newman 2016; Montero, Lewis, and Araya 2017), and Middle America Trench as black line with triangles. All available times are shown in Movie B.11. Time periods are colored as follows: (a - red) strong seaward motion in January 2013, (b - orange) diminished seaward motion in December 2013, (c) slight trench-parallel motion in March 2014, (d) peak trench-parallel motion in April 2015, (e) diminished trench-parallel motion in October 2015, and (f) oblique landward motion in May 2016. Interseismic results of Feng et al. (2012) shown with white arrows on panel (f). Convergence vector and its trench-normal, trench-parallel, and sliver motion components indicated in black, purple, green, and blue arrows, respectively (DeMets, Gordon, and Argus 2010; Feng et al. 2012) and displayed in panel (e). Coastal stations are shown in pink, mid-peninsula stations in teal, mainland stations in purple, Gulf of Nicoya stations in blue, and backarc station in grey (Table B.1). 76

3.2 Result of backslip inversions during (a) Postseismic Sliver Transient (PST) initiation, (b) maximum PST, (c) post PST, and (d) the end of the study period, including red contour showing the area of greater than 1 m coseismic slip (Kyriakopoulos and Newman 2016). Proportion of maximum total coupling is colored and contoured, relative to 83 mm/yr convergence (DeMets, Gordon, and Argus 2010), with vectors indicating the direction of hanging wall motion. Average trench-parallel velocities for each time period are removed prior to inversions, as discussed in method, but locking is allowed in either trench-parallel direction and normal faulting (backslip). Interface geometry shown by grey contours (Kyriakopoulos et al. 2015). Middle America Trench shown as solid line with triangles, and area of recoverability indicated by the thick white line (Figure B.6). Model misfit evaluations and comparison of observed to predicted surface velocities can be found in Figures B.4 and B.5, respectively. 77

3.3 Conceptual model of forearc motions observed herein, delineated along the megathrust interface (inclined plane) and arc-bounding fault (vertical). This model is generalized beyond the study area, but surface velocities are consistent with those observed in Figure 3.1 and B.7. The incoming oceanic plate, marked by vector "o", maintains oblique convergence. Representative surface velocities shown as vector "s". Blue faults are poorly coupled or unclamped, and red indicates that the fault is relatively well-coupled or strong. During (1) afterslip, the forearc moves seaward in a trench-normal direction, sliding along a weakly-coupled megathrust and unclamping the arc fault. The afterslip is driven by stored elastic stress and coseismic stress changes. As (2) relocking initiates, coupling increases in the shallow megathrust and seaward velocities are diminished or gently reversed. (3) During the PST, coupling is low on the megathrust and arc fault but stored compressional stresses were already released by afterslip. Partitioning of slip during the PST thus results in purely trench-parallel sliver motion. (4) Relocking reinitiates, and eventually the megathrust is highly coupled. Slip is no longer partitioned, and stress accumulates in the direction of convergence, regardless of the state of the arc-bounding fault. 78

4.1 Availability of daily waveforms, through 2013, at all stations used in this study. 100

4.2 Functional fits to observed continuous GPS data, as described in Section 4.3.1. North is shown in purple, east in blue, and upwards in pink. Data are dots with vertical error bars, and fitting functions are shown as lines. 101

4.3 Example of corrected campaign GPS data for station MATA, with east component in blue and north in black. Observations (x's) are better fit by corrected data (solid line) than by the dashed lines which were output from the two dimensional (2D) interpolation alone. Note that resulting time series (solid lines) are still richer in information than a simple relaxation curve for these same data. 102

4.5 Result of slip inversion, taken at the time of the 2015 campaign, using interpolation method (left) and real data (right, from Hobbs et al. 2017). Region of high recoverability and resolution indicated by purple polygon. Repeating earthquakes from immediately after earthquake to end of 2013 shown as purple stars, all other seismicity shown as grey circles. EPR-CNS boundary shown as dashed black line. Slip, scaled from blue to red as 0-1.6 meters. 105

4.6 All aftershocks from this catalog and that of Yao et al. (2017), from immediately after the 2012 M_w 7.6 event until the end of 2013. Top panel shows the number of events through time, while bottom panel shows the magnitudes (Local Magnitudes (M_Ls)). Note that all events with magnitude below Magnitude of Completeness (M_C) are shown in green. 106

4.7 Gutenberg-Richter relation for all aftershocks shown in Figure 4.6. Excluded events, with magnitude below M_C, are shown in green. Line of best fit is shown in red, for data shown as blue dots. 107

4.8 Cumulative slip for each family of repeating earthquakes, from 2012 (Yao et al. 2017) through 2013 (Section 4.3.2). 108

4.9 Comparison of afterslip / 2012-2013 aftershocks against (left) b-value mapping of Ghosh et al. (2008) and (right) results of Coulomb stress calculation. Afterslip is shown as navy blue contours ranging from 0-1.5 m slip. Grey points are all seismicity, with repeating aftershocks shown by purple stars. Purple polygon is the region of good recoverability for afterslip. . . . 109

4.10 Full movie can be found at `http://geophysics.eas.gatech.edu/people/thobbs/outputs/3DInterp_2012-2017_final.gif` — above is only a still representation. Movie is the full version of Figure 4.4, showing monthly progression of cumulative afterslip and overlain aftershocks (grey for regular events, purple stars for repeaters). Polygon shows region of good recoverability. 110

5.1 Figure from (Energía 2017). Average rainfall, by month, from 1957-2017 in Liberia, Costa Rica just inland of the Nicoya Peninsula (within the study area). Wet season extends from April to December. Two peaks in rainfall can be seen, with the second and higher peak resulting from the effect of Hurricane season. The period between the two peaks is referred to as the 'veranillo' or little summer. 121

A.1 Postseismic slip for 2D geometry of Nicoya subduction zone, allowing for slip at the trench (free surface). κ of 9000 is used for comparison against 3D models in main text. Interface geometry consistent with Feng et al. (2012) and Protti et al. (2014). Magnitude of slip scaled by color, with arrows showing direction of hanging wall motion at each patch. Aftershocks until end of 2012 shown as grey dots, with purple stars representing locations of repeating aftershock clusters (Yao et al. 2017). Thick black line with teeth marks the Middle America Trench, while thin grey lines show depth in 10 km intervals. EPR-CNS suture shown as dashed line (Barckhausen et al. 2001). Comparing with Figure 2.7, there is little discrepancy between the simpler 2D geometry shown here and the full 3D model reported in the main text. 124

A.2 GPS displacements for 2012-2015 time period, shown for comparison against model predictions for preferred slip result with fixed surface. Observations shown by colored arrows, with predictions indicated by black arrows. Left panel shows horizontal displacement, right shows vertical. Dashed line in right panel shows modeled zero vertical deformation, separating uplift from subsidence. Compare to Figure 2.8 of main text, showing same data compared to predicted vectors using non-fixed surface model. Results are almost identical, indicating that the data is unable to resolve between models with and without slip at the interface. 125

A.3 Time series of GPS displacements for continuous station BIJA, located on the southeast side of the Gulf of Nicoya. This non-peninsula site does not display a strong postseismic response, but the general northeast trend is interrupted in early 2014 by a southwest transient lasting up to one third of the year. As discussed in the main text, this matches observations at other stations surrounding the Gulf of Nicoya and points to a slow slip event in that region. 126

B.1 Tectonic overview of the study area, wherein Cocos (CO) and Nazca (NZ) plates subduct beneath Caribbean (CA) plate and proposed Panama Microblock (PM) (Bird et al. 2002). Separation of crust sourced at the EPR and CNS Center is marked by thin dashed black line (Barckhausen et al. 2001). The Central Costa Rica Deformed Belt (CCRDB) is bounded by dashed green lines (Marshall, Fisher, and Gardner 2000). The Middle America Trench (MAT) is marked by a black line with triangles in the direction of subduction. Volcanoes shown as red triangles. Haciendas-Chiripa Fault System (HCFS) and potential Candelaria Fault connector are shown as blue dashed line (Kyriakopoulos and Newman 2016; Montero, Lewis, and Araya 2017). Plate motions are shown for stable Caribbean reference frame (DeMets, Gordon, and Argus 2010), indicated by cyan vectors. Seafloor bathymetry and crustal topography shaded in grey (Ryan et al. 2009). Country boundaries shown as thin black lines. (b) Zoomed in view of Nicoya study area. Nicoya peninsula (NP) and Gulf of Nicoya (GN) are labelled. Cumulative slip, in meters, from 2014 and 2015 slow slip events indicated by purple contours (Voss et al. 2017). 128

B.2 Averaged azimuth, trench-normal velocities, and trench-parallel velocities, in stable Caribbean reference frame. Daily velocities, calculated over the following year, are the weighted average of individual GNSS stations grouped by location. Coastal stations in pink, mid peninsula stations in teal, mainland stations in purple, Gulf of Nicoya stations in blue (Table B.1). Standard deviations are shown as transparent regions. PST indicated by grey rectangle from 2013.95-2015.80. The 2014 and 2015 SSEs indicated by blue and red rectangles, respectively (Voss et al. 2017). For reference, azimuth of oblique seaward convergence, trench-normal, trench-parallel, and oblique landward convergence are plotted in the top panel and inset. The range of previously observed interseismic velocities is shown in the second panel, and the third shows the measured average sliver transport rate from the previous interseismic (Feng et al. 2012). 129

B.3 North and East horizontal error [mm] for daily positions at all stations. Colors are randomly generated. Blue horizontal line represents the 3 mm error threshold used in this study. Clearly errors are largest near the start and end of data availability for any station, with a steep increase in error before and after data gaps. The threshold selected aims to preserve data from as many stations as possible while minimizing spurious datapoints. . . 130

B.4 Comparison of a sampling of different inversion strategies, all computed for the maximum PST time period starting at 2015.29 (green), for the same smoothing parameter. Leftmost column shows results presented in main text (Figure 3.2d), wherein the average trench-parallel velocity is subtracted prior to inversion. Far right column also subtracts the average trench-parallel motion. Center columns show the results if 11 mm/yr is subtracted instead, to represent the previously-recorded sliver transport rate (Feng et al. 2012). The two right columns shows the result where the contribution from the 2015 SSE (Voss et al. 2017) is also removed, for available stations. The top row shows the results when slip is allowed at the trench (free surface), while the bottom shows the same results where slip is set to zero at the free surface. Model misfit indicated at topleft of each panel. All results show less than 50% coupling anywhere inside the polygon of recoverability (thick white line), suggesting the results presented herein are not an artifact of the inversion strategy. The outcome is similar even with different assumptions about the rate of sliver motion and impact of slow slip event, as shown by the similar misfits. These do not constitute all possible inversions strategies, but rather are selected as a representative set to show that the key findings are the same irrespective of the inversion details. 131

B.5 L-curves of roughness versus misfit for backslip inversions at (a) 2014.22, (b) 2015.30, (c) 2015.80, and (d) 2016.40. Kappa (κ) of 60,000, indicated by stars, is selected to jointly minimize roughness and model misfit. Resulting backslips are shown in Figure 3.2. 132

B.6 Horizontal and vertical surface velocities at (a) initiation of PST, (b) maximum PST, (c) after PST completion, and (d) at the end of the study period. Observed GNSS velocities are shown in red/blue with 95% error ellipses, and velocities predicted by backslip model are shown as black vectors for horizontal components and dash-delimited zones of uplift/subsidence for the vertical. 133

B.7 Resolution spread parameter (defined in Menke (1989) and implemented in Kyriakopoulos et al. (2015) and Hobbs et al. (2017)), which demonstrates the distance over which the model is sensitive to data. Plotted over top of slip results for maximum PST (2015.30 – green) with average trench parallel motion subtracted (consistent with Figure 3.2b). A larger spread means the model is sensitive to data over a larger area. Thus, the areas over which the model is sensitive only to nearby data are the areas over which the model has better recoverability. We select the 150 km contour for plotting for the 16 stations used in this study, with a smoothing parameter (κ) of 60,000. For comparison, the thick black line shows the polygon of recoverability corresponding to resolution spread of 20-25 km from Hobbs et al. (2017), which used a smoothing parameter of 9,000 and 40 stations. Despite showing roughly the same shape, resolution is diminished both by the reduced number of stations and the high level of smoothing. The resolution spread parameter is strongly affected by the smoothing, such that the relatively large smoothing implemented in this study (Figure B.4) results in a relatively large resolution spread even though our data are still able to constrain slip in the area near the Nicoya Peninsula and immediately offshore. 134

B.8 Number of recorded earthquakes (bar) and their magnitudes (circle) for the (a) OVSICORI network and (b) Haciendas-Chiripa catalogue (Montero, Lewis, and Araya 2017). A M_C of $M_L \geq 2.5$ is selected from the full OVSICORI catalog. Black vertical line shows timing of the 2012 M_w 7.6 Nicoya earthquake. PST shown by grey rectangle, during which time no clear change in seismicity is observed. 135

B.9 Focal mechanisms for nearby events following the 2012 Nicoya mainshock (Chaves et al. 2017). Temporal evolution shows no discernable aberration during the PST (2013.95-2015.80). 136

B.10 Eruptions of volcanoes in study area (Fig B.1b) through the 20th century, as recorded by the Global Volcanism Program database. Volcano names are plotted at their latitude, with grey text indicating a volcano that did not erupt over the time period considered. Superimposed are megathrust earthquakes $M_w \geq 7.0$. Non-eruptive activites such as seismic swarms and fumarolic activity are not indicated here. 137

B.11 Full movie can be found at `http://geophysics.eas.gatech.edu/people/thobbs/outputs/oneyear_vels_2018.gif` — above is only a still representation. Velocities, through time, at all available GNSS stations. Immediately after the 2012 mainshock velocities are large and seaward, diminishing through late 2013. Velocities are then seen to point NW, for a period of pure sliver transport in 2014 and 2015. Following this, velocities rotate landward, starting at coastal sites, to resume oblique, interseismic motions. Interseismic results of (Feng et al. 2012) shown in white. Convergence vector and its trench-normal, trench-parallel, and sliver motion components indicated in black, purple, green, and blue arrows, respectively (DeMets, Gordon, and Argus 2010). (b) Raw northward displacements (ITRF2008 reference) for selected stations, labeled in (a). Coastal stations shown in pink, Gulf of Nicoya stations in blue, and backarc station in teal. All other stations, on and around the peninsula, in purple. 138

LIST OF ACRONYMS

2D two dimensional 114

3D three dimensional 114

CNS Cocos-Nazca Spreading Center 6

EPR East Pacific Rise 6

FEM Finite Element Model 38

GT Georgia Institute of Technology 11

GNSS Global Navigational Satellite System 12

GPS Global Positioning System 112

MAD Median Absolute Deviation 88

MAT Middle America Trench xiv

$\mathbf{M_C}$ Magnitude of Completeness 112

$\mathbf{M_L}$ Local Magnitude 88

$\mathbf{M_o}$ Moment 41

$\mathbf{M_w}$ Moment Magnitude 112

OVSICORI Observatorio Vulcanológico y Sismológico de Costa Rica 11

PST Postseismic Sliver Transient 113

RMS Root Mean Squared 37

SSE Slow Slip Event 123

UCSC University of California Santa Cruz 11

UNAVCO University NAVSTAR Consortium — `http://www.unavco.org` 13

USF University of South Florida 35

USGS United States Geological Survey 8

UTC Coordinated Universal Time 35

WMF Waveform Matched Filter 12

SUMMARY

The 2012 Moment Magnitude (M_w) 7.6 Nicoya Earthquake provides an unprecedented opportunity to observe the postseismic recovery and relocking of a megathrust, due primarily to the close proximity of land to the coseismic rupture area. Whereas it is common for the coast to be over a hundred kilometers from the trench, in Nicoya this distance is a mere 60 km. Additionally, a dense network of Global Positioning System (GPS) and seismic instruments has existed since prior to the mainshock. Capitalizing on the existing infrastructure, this course of research undertook to augment continuous GPS observations by completing 3 sets of campaign GPS occupations, more than doubling the number of stations in the network at those times.

The multiyear postseismic period and eventual relocking of the megathrust were characterized primarily through measurements of the surface deformation, with seismic observations also included to cumulatively elucidate the temporal and spatial evolution of fault behavior. Combining rich data with sophisticated inversion techniques, I was able to determine corresponding slip and locking on a fully three dimensional (3D) megathrust geometry. Additionally, a new interpolation methodology was developed to fully utilize campaign and continuous GPS data despite heterogeneous spatiotemporal sampling intervals.

Afterslip, with equivalent M_w of 7.5 within the zone of recoverability, was shown to exist in patches that were distinct from aftershocks. Both afterslip and aftershocks were most abundant immediately updip of the coseismic rupture patch, with more diffuse afterslip posited to occur at depth. This was an important, albeit failed, test of the applicability of using repeating aftershocks as a proxy for slip. As trench-normal afterslip waned, relocking was initiated and subsequently interrupted by a period of exclusively trench-parallel motion across the Nicoya forearc. This was a novel observation, proving that trench-parallel velocity of the forearc can be variable. Combined with results of a backslip inversion, these findings suggest that slip partitioning may be controlled by megathrust coupling rather than

being a static feature of a subduction zone. By 2016 the surface velocities returned to pre-seismic levels, indicating a return to stable interseismic conditions.

This study provides the most detailed measurement of afterslip to date, by incorporating densely spaced seismogeodetic observations from directly above the seismogenic zone. Findings are able to exclude the previously invoked 'tectonic escape' model of Central American Forearc motion, and cast doubt on the use of repeating aftershocks as a proxy for fault slip. By improving our understanding of the heterogeneous nature of megathrust slip in Nicoya, this work augments our knowledge of subduction zones elsewhere which may have lower resolvability due to limitations in data.

CHAPTER 1
INTRODUCTION AND BACKGROUND

1.1 Great Earthquakes

The top 10 most fatal earthquakes between 1900 and 2010 claimed roughly 1.5 million lives cumulatively (Daniell et al. 2011). As global population continues to rise, so too will the number of earthquakes with large human death tolls (Holzer and Savage 2013). This is particularly true in most developing nations and in poorly-constructed dwellings in rural areas (Wyss 2018). These facts highlight the need for improved understanding of where, when, and how earthquakes rupture, so as to improve preparedness and mitigate future disasters.

A subduction zone is a place where one tectonic plate slides beneath another, along a ramp-like surface called a megathrust. This is the only structure capable of producing the largest earthquakes with Moment Magnitude (M_w) ≥ 9. Therefore, subduction earthquakes, and their associated secondary hazards, can be particularly devastating and are worth additional focus. The 11 March 2011 M_w 9.0 Tohoku-Oki earthquake and tsunami produced over 18,000 fatalities (Fujii et al. 2011; Khazai and Daniell 2011), while the even larger 26 December 2004 M_w 9.2 Sumatra-Andaman earthquake and tsunami claimed over 220,000 lives (Lay et al. 2005; Daniell et al. 2011). Although the Sumatra earthquake sadly occurred in a place with little or no hazard warning system, the Tohoku-Oki disaster was particularly sobering because it occurred in Japan: arguably the country which is most prepared for earthquakes (Cyranoski 2011). Tsunami warnings were issued within minutes after the event, and yet many people died inside of or behind tsunami protection structures (Plümper, Flores, and Neumayer 2017). This was due to our insufficient understanding of the subduction zone, leading to a belief that a M_w 9.0 earthquake was not possible (Ozawa

et al. 2011). However, the fault slip in the shallow portion of the megathrust was estimated at a staggering 60 m (Ide, Baltay, and Beroza 2011; Fujii et al. 2011; Lay et al. 2011). This was unexpected given standard scaling relations of earthquake slip to fault length (e.g. Wells and Coppersmith 1994; Liu-Zeng, Heaton, and DiCaprio 2005), but we now know that clay minerals on the fault surface can contribute to such large offsets (Chester et al. 2013). For the 2004 Sumatra earthquake and tsunami, scientists took the first ever satellite measurements of tsunami height in the open ocean, showing an unanticipated channeling of tsunami energy along mid-ocean ridges and enabling researchers to confirm their propagation models (Geist, Titov, and Synolakis 2006; Synolakis and Bernard 2006). Thus by studying the 2004 and 2011 disasters, and other very large events, there have been incredible breakthroughs in our understanding of earthquake physics in a subduction environment. Accordingly, expanding our knowledge will help with refining models of seismic hazard and optimizing disaster response strategies.

Trying to understand subduction stresses by looking only at the coseismic motions from really large events as they happen is an imperfect way to prepare for future destructive events, however. This is because (1) most of them are too far offshore to be studied well (Williamson and Newman 2018), (2) in most cases we don't know where an event is going to happen and as such cannot always ensure dense instrumentation prior to an earthquake (e.g. Chen et al. 2009), (3) even if we do have instruments and they are close enough to record a great earthquake they may be clipped or damaged in the event itself (e.g. Bilich, Cassidy, and Larson 2008; Zheng et al. 2012), and (4) M_w 9.0 events occur 1–2 orders of magnitude less frequently than M_w 7.0–8.0 events. The final and most compelling reason, (5), is that by looking at coseismic data we miss out on so much of the total signal from the converging of plates. Stresses for great earthquakes accumulate over decades, centuries, or perhaps millenia (McCaffrey 2008). And as instruments have become more sensitive, as networks have expanded, and as offshore geophysics has become more cost-effective we have recorded a surfeit of new megathrust behaviors during all stages of the seismic cycle

(e.g. Dragert, Wang, and James 2001; Khazaradze et al. 2002; Obara 2002; Shelly et al. 2006; Schwartz and Rokosky 2007; Kato et al. 2012). While the central goal of earthquake science may be to reduce the damage caused by very destructive events, contributing to that goal requires consideration of the entire subduction system through time. Such studies are helping us to, for instance, forecast the spatial extent of an earthquake before it happens (e.g. Feng et al. 2012), understand the range of dynamic behaviors that the megathrust can display besides large earthquake shaking (e.g. Beroza and Ide 2011), and to understand how those behaviors might interact with eventual large earthquakes (e.g. Radiguet et al. 2016).

1.2 Understanding Subduction Physics through the Seismic Cycle

As shown in Figure 1.1, the seismic cycle describes the conditions of the fault through time: the interseismic, in which the relative motion of the two plates is stored as strain across a locked fault; the coseismic, in which coupling on the fault is lost and dislocation occurs rapidly; and the postseismic, in which the fault returns to the quasi-stable interseismic conditions over timescales that vary with the magnitude of the mainshock. After a large earthquake a number of processes contribute to the observed postseismic deformation field. In addition to aftershocks, smaller earthquakes caused by the mainshock, it is also important to consider afterslip, the aseismic continuation of slip along the fault interface over weeks to months, and relocking, the process by which coupling increases on the fault such that stress can begin accumulating for the next event. There are also inelastic processes acting through this time: poroelastic rebound, in which the coseismic pore fluid overpressurization is diffused, and viscoelastic relaxation, in which the earth's mantle responds to the stresses imparted during the mainshock. The dominant plate motions that occur through the postseismic period are featured in Figure 1.2. Although much attention is paid to the coseismic signal, afterslip can account for almost as much (Uchida et al. 2004) or potentially even more (Hobbs et al. 2017) slip than the mainshock itself.

A working knowledge of the physical conditions in the near-surface has already led to development of methodologies considered sufficient for the description of the general, time-dependent character of afterslip and aftershocks (e.g. Freed 2007; Johnson, Bürgmann, and Freymueller 2009; Malservisi et al. 2015). Stress heterogeneities at the edges of regions of strong coseismic slip contribute to rapid afterslip and high aftershock productivity immediately following the mainshock rupture, with exponential (e.g. Freed 2007; Malservisi et al. 2015) and power law (Omori 1895; Utsu 1970) decay, respectively. As such, measuring afterslip and aftershocks allows one to directly map the stresses on the fault as they are relieved over weeks or months. However, the methods used to study regions rich in postseismic activity are only sensitive to nearby fault slips. Accordingly, many models of afterslip are unable to comment on deformation in the shallow megathrust, which is often tens or hundreds of kilometers offshore (Williamson and Newman 2018). Accurately constraining the extent of afterslip may be particularly important in the near-trench region, where unrelieved stress may contribute towards the nucleation of tsunami earthquakes. These are a class of slowly rupturing, shallow earthquakes that generate tsunami which are disproportionately large and dangerous for their comparatively small seismic energy release (Kanamori and Kikuchi 1993). Hence, providing a detailed description of afterslip in the region updip of the coseismic rupture has remained an outstanding problem in the field.

Similarly, relocking estimates are important for seismic hazard characterization at convergent margins with long recurrence intervals. If one aims to determine the maximum seismic potential it is common to use the current interseismic strain accumulation rate to estimate total accumulated slip since the last major earthquake. Such calculations overpredict for subduction zones that experience an extended postseismic relaxation, as in schematic Figure 1.3. For a constant intereseismic rate (interseismic A), the accumulated displacement considered at time t after an earthquake (shown in inset) would be very different for an over-simplified model without well-known postseismic deformation (interseismic B) than

for the more realistic case of interseismic C. This illustrates the importance of improving our understanding of the processes and characteristic timescales of postseismic processes as they contribute to our knowledge of seismic potential and therefore improves estimates of realistic seismic hazard.

1.3 The Nicoya Peninsula as a Natural Laboratory

1.3.1 Tectonic Setting

As shown in Figure 1.4, Costa Rica is an ideal location for studying the megathrust. Here the Cocos Plate subducts beneath the Caribbean Plate at approximately 82 mm/yr at N45^{o} (DeMets, Gordon, and Argus 2010). This margin is oblique by roughly 25^{o}, with obliquity increasing along strike to the northwest and decreasing to the southeast. Several geodetic surveys (e.g. Lundgren et al. 1999; Iinuma et al. 2004; Norabuena et al. 2004; Feng et al. 2012) have confirmed that northwestward translation of the Central American Forearc is occurring, with modeling suggesting that it is driven either by the obliquity of the incoming plate or by a process called 'tectonic escape' (Kobayashi et al. 2014). The subducting Cocos Ridge, a 2 km high bathymetric feature, is being rigidly indented into southern Costa Rica (Walther 2003). It has been posited by Kobayashi et al. (2014) that this drives outward, escaping motion of the Panama Block and Central American Forearc (Figure 1.6), although previous data have been unable to distinguish between the obliquity and tectonic escape models.

Regardless of the driver, the result is roughly 11 mm/yr (Feng et al. 2012) of sliver transport to the northwest. This motion is thought to be accommodated along a fault system that runs through the arc volcanics of Costa Rica (Montero, Lewis, and Araya 2017). Shown in Figure 1.4, the Haciendas-Chiripa and Candelaria are both dextral strike slip faults with an ignimbrite deposit covering the region between them. Thus, it is suspected that the two fault strands connect (Kyriakopoulos et al. 2015). Though there is no record of this fault system generating large earthquakes, Montero, Lewis, and Araya (2017) recorded

fresh fault scarps and a group of moderate sized earthquakes in July 2016. Given that the steep hills of poorly-cemented soil surrounding this fault are so well populated, determining the seismic potential here is an outstanding an urgent task for scientists. To this end, we have installed a network of 5 campaign GPS monuments transecting the fault (Figure 1.4). The monuments are 6 inch steel pins drilled and epoxied into bedrock. Sites were selected based on, in order: location along the planned transect, bedrock availability, safety, and good sky view. It is our hope that in the coming years, campaign displacements at these locations will be sufficient to constrain if strain is being accumulated along this fault. If so, we also hope to determine the depth of locking for a precise estimate of seismic potential.

1.3.2 The Nicoya Megathrust

The Nicoya Peninsula extends to within 60 km of the trench. This means surface measurements of megathrust activity can be taken from much closer to their source regions than would be possible in other areas. As a result of this preferred land geometry, Nicoya has been the focus of numerous geophysical investigations over the past 20 years. Previous studies have utilized seismic (e.g. Protti, Güendel, and Malavassi 2001; DeShon et al. 2006; Dinc et al. 2010) and geodetic networks (e.g. Lundgren et al. 1999; LaFemina et al. 2009; Feng et al. 2012), ocean drilling (e.g. Vannucchi et al. 2001), heat flow (e.g. Harris et al. 2010), and geomorphological observations (Marshall and Anderson 1995; Protti et al. 2014) to characterize the megathrust in great detail. Most recently, Kyriakopoulos et al. (2015) aggregated seismic data from several studies to produce a fully three dimensional (3D) model of the slab interface (Figure 1.5). It showed complex topography, with a change in the steepness of the downgoing slab across the East Pacific Rise (EPR)-Cocos-Nazca Spreading Center (CNS) boundary. This change in oceanic crust provenance also corresponds to a change in inherited faulting direction and therefore temperature between the relatively cooler material sourced at the EPR and the warmer crustal material being generated at the CNS (Barckhausen et al. 2001; Newman et al. 2002). Despite these differ-

ences, both the EPR and CNS crust are roughly the same age (Fisher et al. 2003). Further to the southeast, the continuation of the Fisher Seamount Chain is subducted beneath the tip of the Nicoya Peninsula (Barckhausen, Roeser, and Huene 1998). Overall, though the incoming plate in Nicoya is far from featureless, it still shares enough commonality with many other subduction zones so as to be representative.

Nicoya is an excellent location to study megathrusts not only due to the rare and proximal location of land relative to the trench, but also because the tectonic motions are sufficiently rapid to generate large (magnitude $\geq$ 7.5) earthquakes roughly every 50 years since 1853 (Protti et al. 1995; Protti, Güendel, and Malavassi 2001; Feng et al. 2012). Nicoya exhibits other flavors of tectonic activity, including concurrent episodic tremor and slow slip (Outerbridge et al. 2010; Walter et al. 2013). Nicoya was identified by Nishenko (1991) as a seismic gap with a 93% probability of rupturing in a magnitude 7.4 earthquake before 2009. The 1990 M_w 7.0 Cobano earthquake at the entrance to the Gulf of Nicoya (Protti et al. 1995) and the 1992 M_w 7.6 Nicaragua tsunami earthquake (Kanamori and Kikuchi 1993) define the along-strike extent of the Nicoya gap (Protti, Güendel, and Malavassi 2001). Only one notable earthquake occurred between 1950 and 2012 within this gap: the 1978 M_w 7.0 Samara earthquake. This event relieved only up to 16% of the accumulated strain (1950-2010) assuming 100% locking on the interface (Feng et al. 2012). The remainder of the energy was released by the 2012 Nicoya earthquake. These features have, together, led to the establishment of Nicoya as a rich natural laboratory for subduction zone studies (`http://nicoya.eas.gatech.edu`) since 1995 (Protti, Güendel, and Malavassi 2001).

1.3.3 The 2012 M_w 7.6 Earthquake

The 5 September 2012 M_w 7.6 Nicoya event, on which this work focuses, initiated 10 km offshore (9.76^o N, 85.56^o W) and 13 km deep (Figure 1.4 herein; Yue et al. 2013, based on joint geodetic and seismic inversion). The main slip area extended for roughly 70 km

along strike and 20 km downdip (Yue et al. 2013), with a maximum slip of 4.4 m (Protti et al. 2014). Strike/dip/rake defining the fault plane, according to the focal mechanism (290/25/90), and centroid moment tensor (317/19/118) from the United States Geological Survey (USGS) catalogue (ComCat 2012b) are consistent with rupture on a shallowly-dipping megathrust interface, accommodating mainly pure thrust (margin-normal) motion. Given oblique convergence, this indicates that the missing component of margin-parallel motion may be accommodated by some other means, such as inelastic deformation of the forearc in the interseismic or postseismic periods (LaFemina et al. 2009).

From the elastic rebound theorem (Reid 1911), coseismic slip occurs to relieve locked portions of the fault. Interestingly, the rupture did overlap significantly with the predicted locked portion of the megathrust as imaged by interseismic deformation (Feng et al. 2012; Protti et al. 2014; Kyriakopoulos and Newman 2016). Although there is limited resolution, the shallow portion of the megathrust (offshore) appears to have been deficient in coseismic slip (Protti et al. 2014; Malservisi et al. 2015). This, as well as the paucity of vertical seafloor deformation (Chacón-Barrantes and Protti 2011), explains the absence of a large tsunami following the 2012 event, but leaves unresolved questions about the possibility of either shallow megathrust rupture or slow slip to relieve this stress (Dixon et al. 2014). Voss et al. (2018) did find compelling evidence for a Slow Slip Event (SSE) which began in late February 2012 in the deeper portion of the megathrust and ultimately migrated to the hypocentral region of the September 2012 mainshock. This SSE was similar in spatial extent to previous SSEs which reoccur approximately every 22 months in Nicoya (Outerbridge et al. 2010; Dixon et al. 2014; Voss et al. 2017).

The largest aftershock was a M_w 6.5 event on 24 October 2012 (ComCat 2012a), with most aftershocks occurring along a trench-parallel band at approximately 15-25 km depth along the slab (Yue et al. 2013; Protti et al. 2014; Chaves et al. 2017; Yao et al. 2017). This sequence was noted to be relatively depleted in large events, with only 5 M_w greater than 5.0 events. Outward propagation of the aftershock front was also observed in both the

along trench and down dip directions (Yao et al. 2017). Within the first 4 months after the mainshock there were repeating aftershocks, those with very similar waveforms (cross correlation coefficient ≥ 0.9), detected near the 'elbow' in the coastline near Punta Guiones (Figure 1.4) by Yao et al. (2017). Repeating earthquakes are produced on small patches of slip-weakening material embedded in an otherwise slip-strengthening environment. In other words: a small piece of earthquake-generating material in an otherwise stably sliding regime. For this reason, repeating earthquakes are thought to be evidence of slip in regions where there are insufficient geodetic data to estimate slip directly and have been broadly applied as such (for a recent review, see Uchida and Bürgmann 2019, and references therein).

Early characterization of the postseismic signal indicates complex overlapping of signals, as anticipated. Malservisi et al. (2015) observed what they interpret as multiple characteristic timescales of postseismic relaxation, potentially representing poroelastic rebound, afterslip, and viscoelastic relaxation signals within the first 2 years. That study was limited mainly to data from high-rate continuous Global Positioning System (GPS), of which there were 9 operating on or near the Nicoya peninsula in the time period they considered. This GPS distribution results in lower spatial resolution than is possible using the full GPS network shown in Figure 1.7. Using all available data is especially important in Nicoya, where we have the unique opportunity to image the subduction zone from directly above and thus create the most detailed model of afterslip available anywhere.

1.4 Outstanding Questions

The aim of this dissertation is to elucidate precise information about postseismic deformation in Nicoya, using dense geodetic and seismic networks (Figure 1.7). Specifically, this work intends to address the following open questions in subduction science:

- Where does afterslip occur, and when?
- Is there residual stress, especially in the near trench region, that could contribute to

potential future earthquakes?

- Where do aftershocks occur, and when?
- How are aftershocks and afterslip related?
- Is it possible to use repeating earthquakes as a proxy for afterslip on the subduction interface?
- Where and when does relocking initiate?
- How long does it take for the megathrust to fully return to interseismic conditions?
- How does the relocking scale with earthquake size relative to great megathrust earthquakes such as Chile 1960, Alaska 1964, and Sumatra 2004?
- Can we learn anything about Central American Tectonics by piecing together information from the previous interseismic, coseismic, and now the postseismic periods?

To answer the questions above I consider the timing and temporal evolution of surface deformation for several years following the 2012 Nicoya earthquake. With campaign GPS, continuous GPS, and a well-maintained seismic network, this dataset is rich both in terms of the amount of data and the proximity of the observations to the seismogenic zone. By using advanced inversion and modeling techniques I can directly relate surface deformation to displacements on the subduction interface, allowing for a quantitative estimate of time-dependent postseismic phenomena including aftershocks, afterslip, and relocking. By accounting for these signals it will be possible to better understand how motion is accommodated or accumulated over the course of the entire seismic cycle at this natural subduction zone laboratory. This has clear consequences for estimating seismic potential of a quiescent megathrust — both in Nicoya and at other subduction zones. As a whole, this work and others will contribute to an improved understanding of subduction zone dynamics in addition to contributing a rich new dataset for future studies of Nicoya.

1.4.1 Seismic Data

Seismometers have been used for hundreds of years to study the motions of the ground. In earthquake seismology, one is interested in measuring the elastic waves that are generated by a fault slip event. Seismograms record three dimensional information about the earthquake source and its path. By using three or more seismometers as well as some information about the speed that seismic waves travel, one can determine the location of an earthquake. This process is called triangulation. However, location determinations are sensitive to the network configuration relative to the earthquake epicenter: it is best to use seismometers that are close by and which have a good azimuthal distribution around the source. As shown in Figure 1.7 and Table 1.1, the 14 station Nicoya Network (YZ) was operating across much of the peninsula, and therefore relatively close to the subduction trench, during the postseismic period of the 2012 mainshock. The majority of the stations are broadband or intermediate sensitivity range, with only one short period instrument (Table 1.1). This network has existed in some form since 1999 (Newman et al. 2002), being in its current configuration since 2008 (Outerbridge et al. 2010). Currently it is maintained by Observatorio Vulcanológico y Sismológico de Costa Rica (OVSICORI), Georgia Institute of Technology (GT), and University of California Santa Cruz (UCSC). Although several stations are telemetering data in real time, servicing of these stations was conducted by our group to check system health, update operational parameters, fix telemetry issues, and replace flash cards for local storage. A typical seismic station setup is shown in Figure 1.8, with buried sensor vault and nearby instrument housing box for power, datalogging, and telemetry.

1.4.2 Aftershock Detection

Waveforms from the YZ network are stored within an Antelope database (`http://www.brtt.com`). An automatic detection algorithm was used to build an initial catalog of aftershocks (Walter et al. 2015). Subsequently, seismic recordings from the Nicoya network

were utilized by Yao et al. (2017), to identify aftershocks from the mainshock until the end of 2012 using a Waveform Matched Filter (WMF) technique (Peng and Zhao 2009; Meng, Peng, and Hardebeck 2013). This methodology relies on previously-identified template event waveforms which are then cross correlated with continuous seismic waveforms. When several stations identify a cross correlation coefficient that is sufficiently higher than the average, an event has been detected (Figure 1.9). When the cross correlation coefficient is greater than 0.9, a 'repeating earthquake' is said to have occurred. As discussed in Section 1.3.3, these events are thought to be important indicators of slip on the megathrust and are therefore of great interest in a place where we are able to compare seismically-determined slip against gedetically-determined slip. As it uses the similarity of waveforms rather than the amplitude of incoming phases, the WMF technique has been shown to detect roughly an order of magnitude more events than other earthquake detection algorithms (Peng and Zhao 2009). Therefore, with 7890 template events (Walter et al. 2015), Yao et al. (2017) detected another 132,900. Those authors also performed a relocation using TomoDD (Zhang and Thurber 2003) with an updated regional 3D velocity model (Moore-Driskell et al. 2013) to improve location accuracy. Repeating earthquake clusters were relocated with HypoDD (Waldhauser and Ellsworth 2000) to ensure events within a family occurred in the same location.

1.4.3 Geodetic Data

The term 'geodesy' refers to measurements of the earth's position and shape. There are several ways to do this, both ground- and satellite-based, including photogrammetry, Light Detection And Ranging (LiDAR), and Interferometric Synthetic Aperture Radar (InSAR), and Global Navigational Satellite System (GNSS). The GPS, which will be the focus of this work, is a specific type of GNSS satellite constellation, operated by the United States. A ground based GPS (equivalently referred to as GNSS) receiver can detect a modulated signal being broadcast from a satellite orbiting 20,200 km above the surface of the earth

(https://www.gps.gov/systems/gps/). Based on the time offset of the modulated signal compared to a reference signal, one can calculate the time that the signal spent traveling from satellite to receiver, and thus calculate the psuedorange (distance). Precise orbital information is known for satellites, with reference to a network of reference GPS stations, and corrections can be routinely made for the effect of the ionosphere, troposphere, and clock biases. Then, much like with earthquake locating, triangulation can be performed with 3 or more satellites to determine the precise location of the receiver in a terrestrial reference frame. Differencing these positions over time tracks the displacement of the ground at the location of the GPS unit or campaign monument.

The Nicoya Peninsula has had a GPS network operating since 2002 (Outerbridge et al. 2010), although some stations were built and operating by the early 1990's. Between 2012 and 2017 there existed a backbone network of 18 continuous stations operated by OVSICORI, in addition to GT campaign occupations at another 22 sites (Figure 1.7 and Table 1.2). Continuous data are telemetered to OVSICORI and stored with University NAVSTAR Consortium — http://www.unavco.org (UNAVCO). As a part of this dissertation research, Trimble R7 and NetR9 receivers are used with Trimble Zephyr and Zephyr 2 antennas (https://www.trimble.com/Monitoring-Solutions/Index.aspx) for campaign occupations in 2012, 2015, 2016, and 2017. A typical campaign station setup is shown in Figure 1.10, with a comparable joint continuous GPS and seismic station displayed in Figure 1.11. For campaign deployment the antenna is affixed to a rigid frame that connects it to the 1 mm dimple in a steel monument pin which has been drilled into the bedrock and affixed with epoxy. The frame is precisely leveled and then weighted to ensure it stays in place. The antenna is connected via coaxial cable to the receiver, which is stored in a foam-insulated pelican case (https://www.pelican.com/us/en/products/cases/protector-cases). Inside of the case are one or two 12 V lead acid batteries and a solar regulator to connect the solar/batteries power system to the receiver. Campaign stations are often fenced, using barbed wire and pointed steel poles,

to protect the sensitive equipment from livestock. An occupation usually lasts 2-5 days, allowing for precise location to within $\sim$ 1-2 mm horizontally and $\sim$ 1 cm on the vertical component. Before ending an occupation, records were backed up to a tablet via ethernet cable.

1.4.4 Geodetic Inversion

Observations of the earth's deformation tell us how the surface is moving with time, but what we are most interested in is the motion occurring at depth on the subduction interface. For that we perform an inversion. As shown in Figure 1.12, a forward modeling approach uses some chosen parameters with an earth model to produce synthetic observations at the surface. An inversion is the opposite of this, taking known data and an inverted model of the earth behavior to determine what the corresponding parameter would be. In this case, the data are the surface displacements, the parameter is slip on the megathrust, and the earth model is a mathematical relationship between the two — called a Green's function. This inversion is completed using the program GTdef, written by T. Chen and L. Feng (Chen et al. 2009), which implements the analytic equations for elastic dislocation presented by Okada (1985). Green's functions are calculated, with a pre-defined fault, for each node–station pair assuming unit (1 m) slip at the fault node. Expressed mathematically: surface displacement observations ($\mathbf{d}$) are weighted ($\mathbf{W}$) by their errors ($\mathbf{d}' = \mathbf{W}\mathbf{d}$), and the weighted Green's functions ($\mathbf{G}' = \mathbf{W}\mathbf{G}$) are used to solve the linear system $\mathbf{d}' = \mathbf{G}'\mathbf{m}$ for slip at depth $\mathbf{m}$ (Jónsson et al. 2002).

For the case when slip is not occurring, one may wish to determine the amount of locking on the interface instead. For this, one would use the backslip approximation of Savage (1983). If the megathrust is fully locked (100% coupling between the downgoing slab and overriding crust) then surface displacements will be landward at the convergence rate. If there is no communication across the fault then the overriding crust would show no landward velocity. Therefore, by inverting interseismic data one can use the resulting

amount of normal (extensional) slip as a measure of the amount of locking. The greater the landward velocity, the greater the locking, and the greater the normal slip — referred to as the backslip.

1.5 Outline

Using the techniques described above, in this dissertation I will examine the full postseismic recovery of the Nicoya megathrust to better understand how stress is released and stored at depth. Firstly, in Chapter 2, I will assess the cumulative afterslip over a 2.5 year period, using the first full campaign and continuous GPS measurements available. Given the density of the GPS network in Nicoya, this study provides the most detailed image of afterslip yet, taken from directly above a megathrust.

While examining the evolution of surface velocities with time, a curious phenomenon was observed between afterslip and relocking. In Chapter 3 I will describe the first ever recording of a postseismic sliver transient, in which purely trench-parallel sliver velocity is observed across the entire forearc. I will also discuss the spatial evolution of locking on the megathrust through this time, as it pertains to the reinitiated accumulation of stress on the Nicoya asperity.

In order to better consider the full time-evolving character of the postseismic signal, in Chapter 4 I will build a new methodology for aggregating GPS datasets that have spatially and temporally heterogeneous sampling. I also use a WMF technique to expand the aftershock catalog of Yao et al. (2017) through another year of the postseismic period. Comparing these results allows us to evaluate the relationship between repeating aftershocks and afterslip; a task which can often be difficult or impossible in the offshore megathrust environment.

Finally, in Chapter 5 I will tie these studies together to illuminate the cumulative results of this work. I will discuss not only the broader impacts of these findings, but also suggestions for future research using these rich datasets, and those from other subduction

zones.

Chapter 2 was published in the Journal of Geophysical Research: Solid Earth and is therefore reproduced here in its published format. Chapter 3 has currently been submitted for publication to Earth and Planetary Science Letters, and Chapter 4 is being prepared for imminent submission to the Journal of Geophysical Research: Solid Earth.

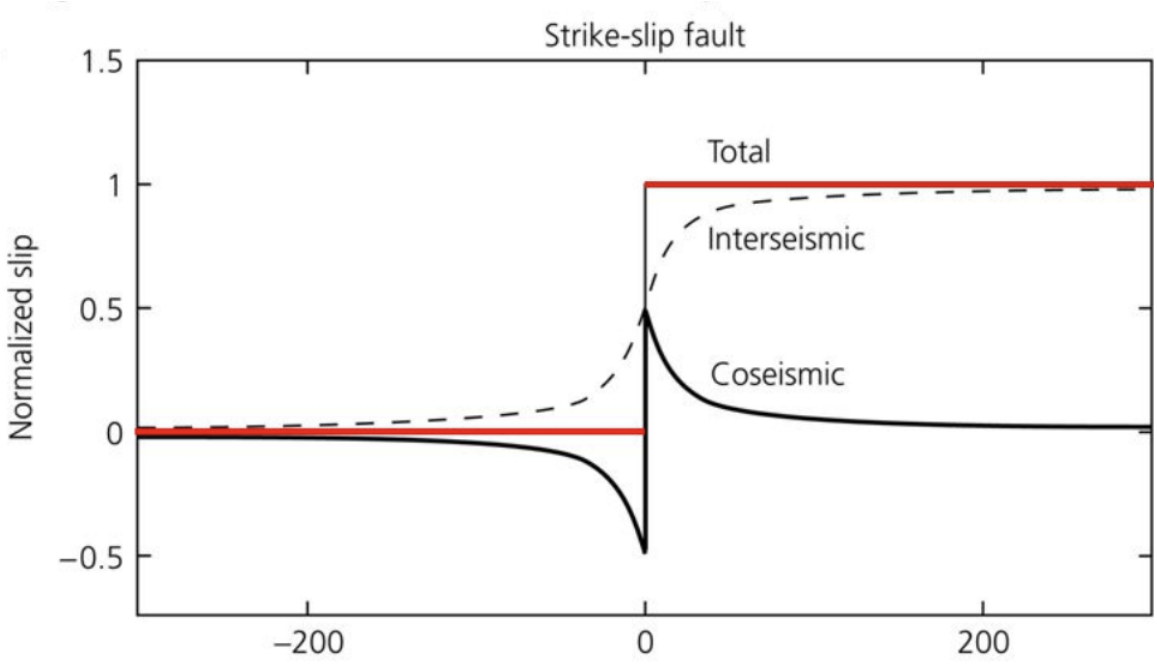

Figure 1.1: Figure reproduced from Stein and Wysession (2003). Normalized total slip, as distributed across an idealized, vertical strike slip fault. Interseismic strain accumulates across the locked fault at '0' on the x-axis, as a result of far-field motion. Coseismic slip is focused close to the fault, relieving the interseismic stress accumulation, such that the total slip is equal at all distances from the fault after a full seismic cycle.

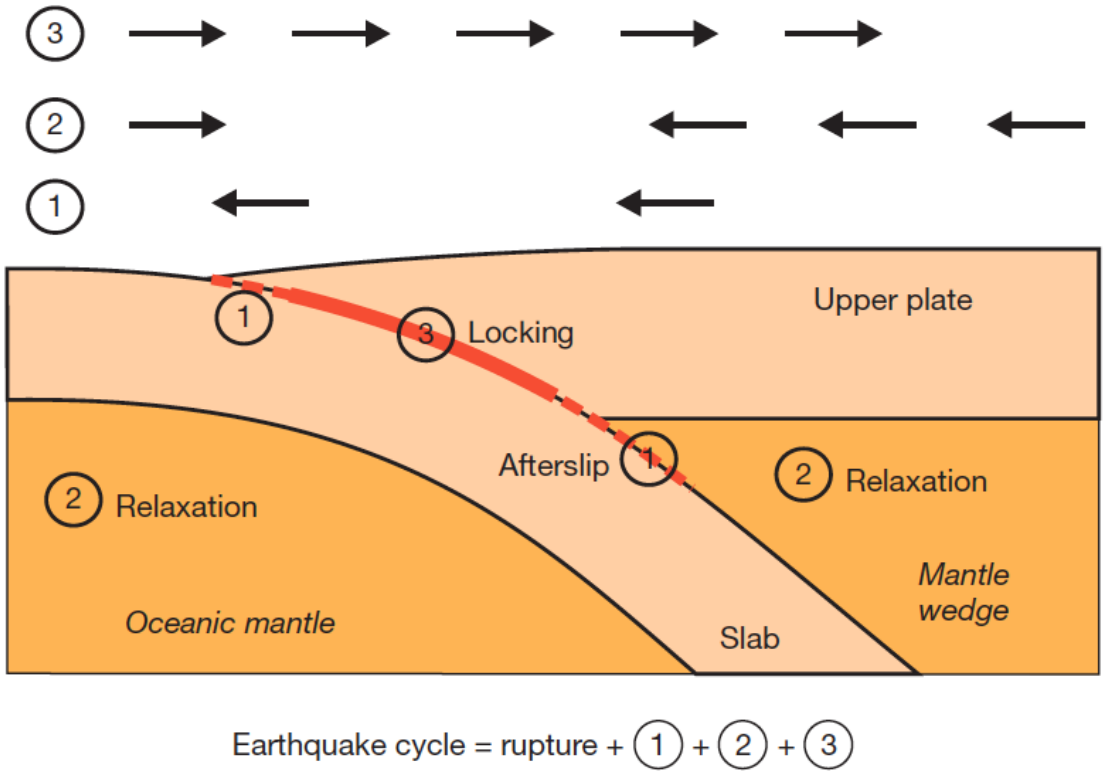

Figure 1.2: Figure reproduced from Wang, Hu, and He (2012). Surface deformations of the postseismic period, with reference to the region of the subduction zone in which they are generated. Immediately after the mainshock, (1) afterslip starts driving wholesale seaward motion at the surface. (2) Viscoelastic relaxation has opposing motions, with coastal sites being the first to show landward motion. (3) Relocking, ultimately, drives all surface deformations in a landward direction.

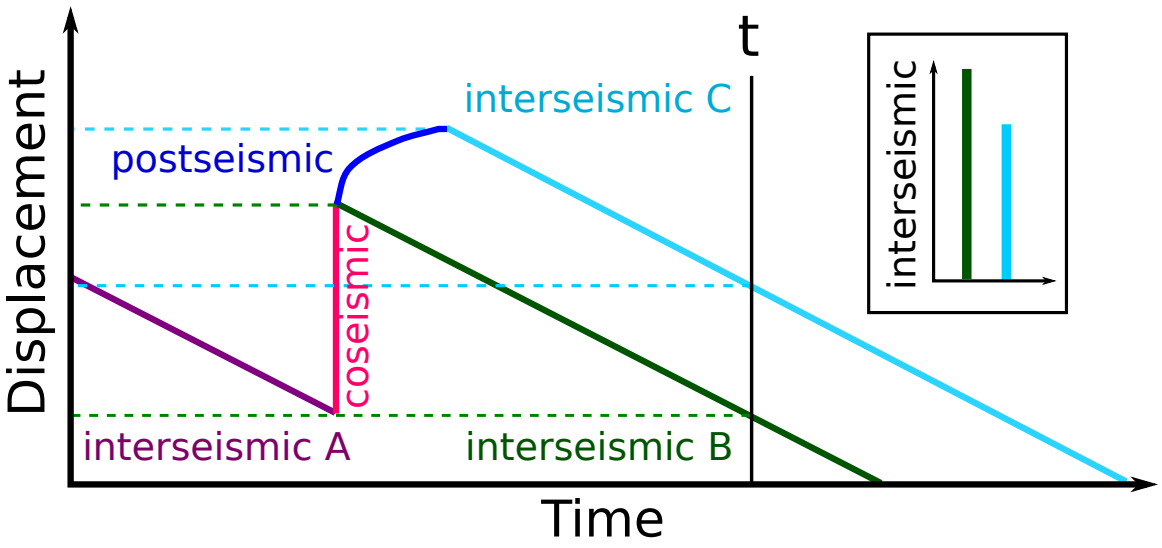

Figure 1.3: A schematic image showing surface displacements, or positions, through the seismic cycle. The effect of including postseismic behavior is illustrated as the difference in displacement at time 't', as well as the relative amount of total interseismic strain accumulation that would be inferred at that time (inset).

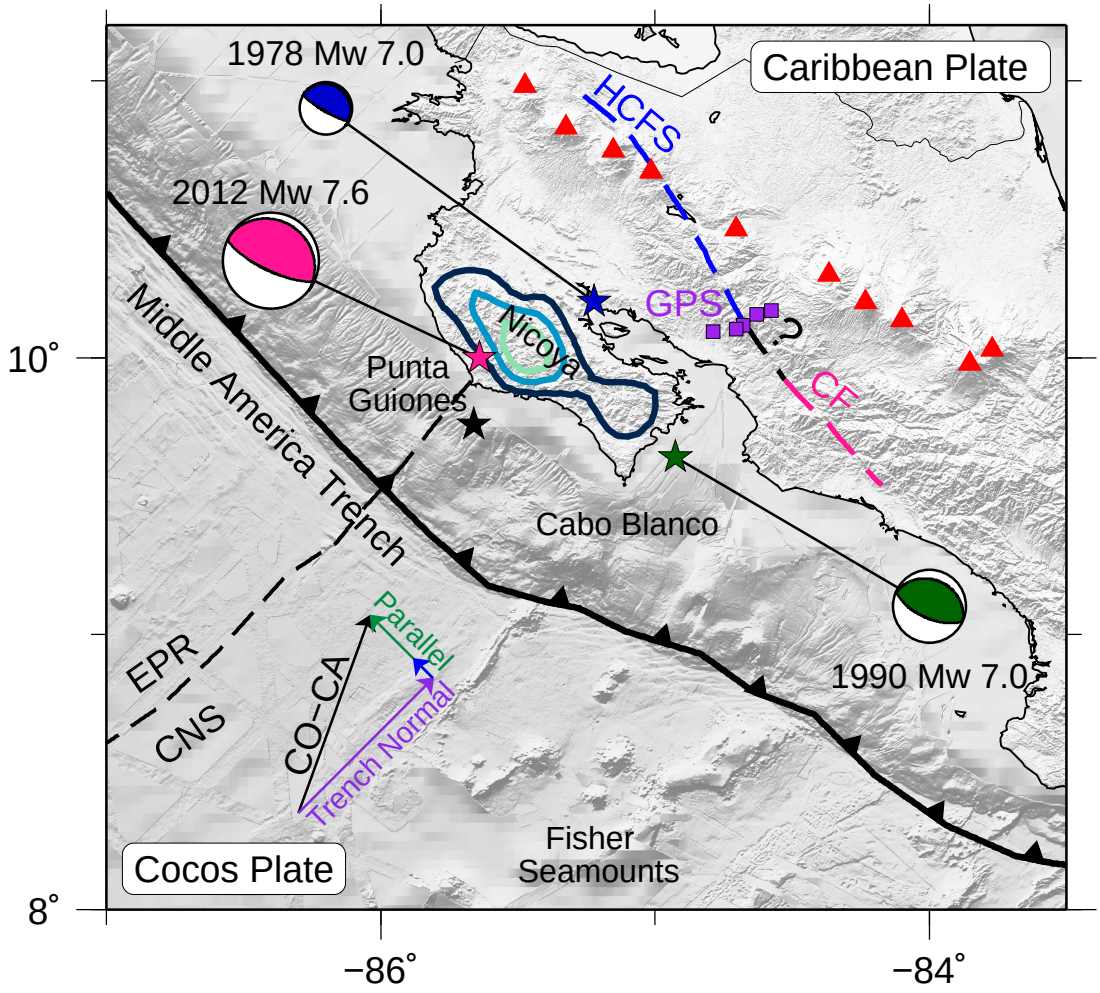

Figure 1.4: Nicoya Peninsula study area in northern Costa Rica. Cocos Plate subducts beneath the Caribbean Plate along the MAT at 82 mm/yr (DeMets, Gordon, and Argus 2010), shown by 'CO-CA' convergence vectors. Previously estimated sliver transport rate of 11 mm/yr (Feng et al. 2012) shown as small blue arrow on green 'Trench Parallel' vector, with 'Trench Normal' in purple. EPR and CNS crustal provenance differentiated by dashed black line. Relevant prior seismicity indicated by beach balls, with epicenters indicated by stars (see Feng et al. 2012, and references therein). Black star corresponds to the initial 2012 hypocenter (Yue et al. 2013). Coseismic slip for the 2012 event, in smoothed 1 m increments, shown in blue contours over the central Nicoya Peninsula (Kyriakopoulos and Newman 2016). Volcanoes shown as red triangles. Best estimates of the faults delineating the back of the Central American Forearc (Kyriakopoulos and Newman 2016; Montero, Lewis, and Araya 2017) indicated by coarse dashed lines: Haciendas-Chiripa Fault System (HCFS - blue), Candelaria Fault (CF - pink) and a hypothesized connector ('?' - black). Newly erected GPS transect of that connector shown as purple squares. Seafloor bathymetry and crustal topography shaded in grey (Ryan et al. 2009).

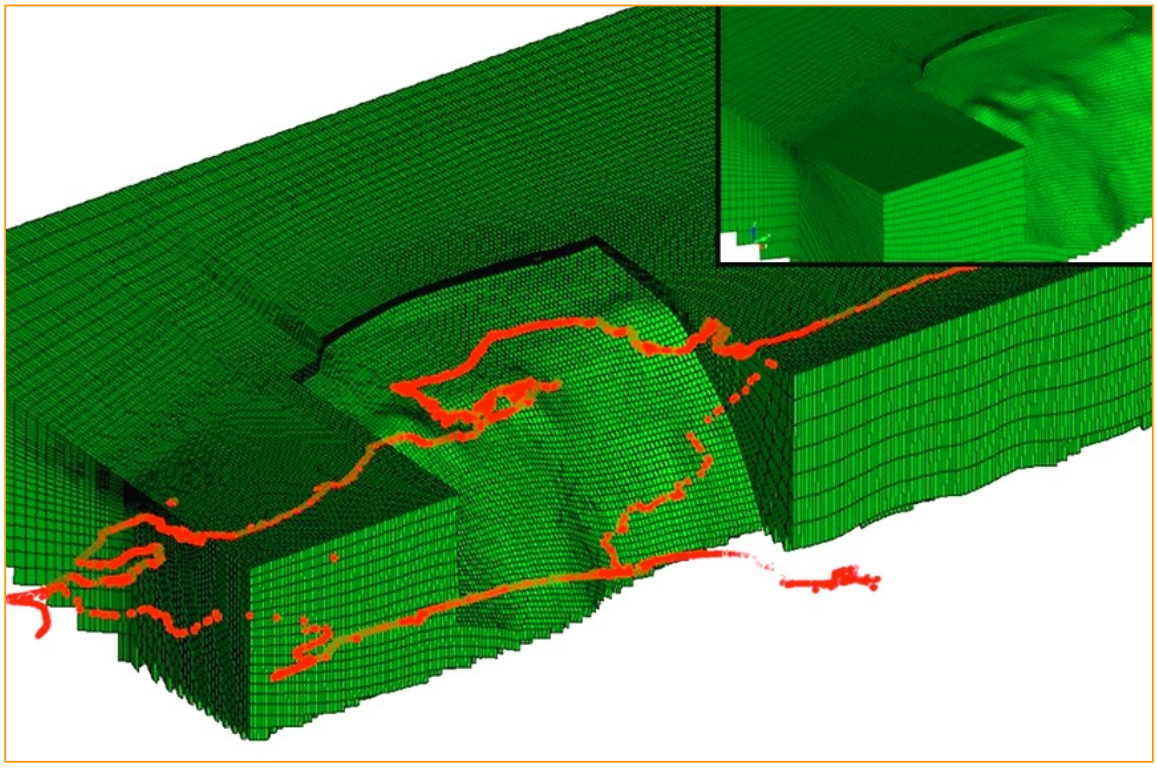

Figure 1.5: Figure reproduced from Kyriakopoulos et al. (2015). West-looking view of the 3D megathrust geometry for the Nicoya Peninsula portion of the Middle America Trench, determined using the Maximum Seismicity Method. Coastlines and country boundaries shown as red lines. Noticeable change in subduction angle between the more steeply-dipping EPR sourced crust in the north (right side of this image) and the more shallow CNS sourced crust in the south (left side).

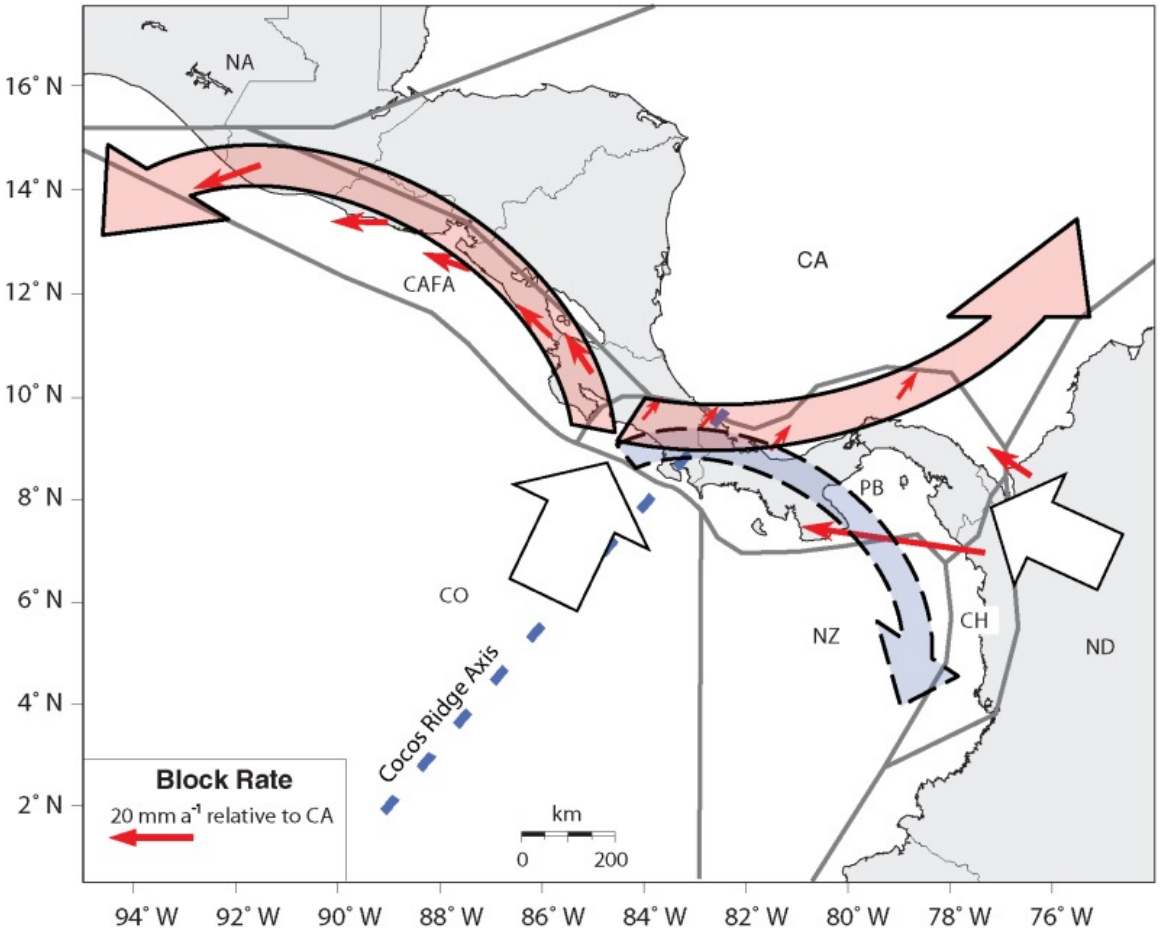

Figure 1.6: Figure reproduced from Kobayashi et al. (2014). Red vectors are resultant motions from a tectonic escape model for Central American Forearc (CAFA) motion. Panama Block (PB) also shows outward motion, with a backstop from the North Andes (ND) block. Also pictures are the North American (NA), Caribbean (CA), Nazca (NZ), and Choco (CH) plates. White arrows show the dominant forces suggested to be controlling motion within this system.

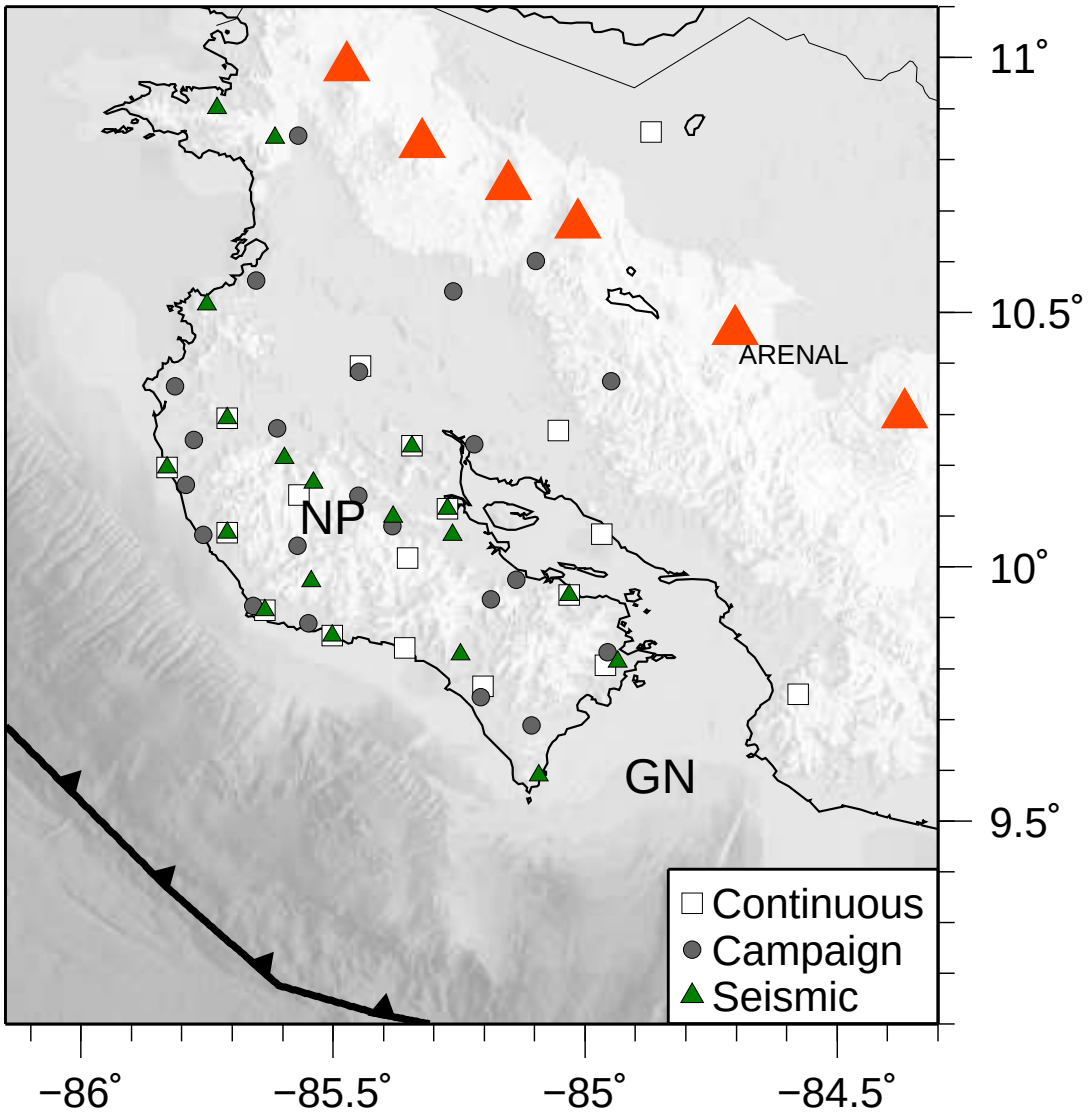

Figure 1.7: Map of GPS (white/grey) and seismic (green) network in Nicoya, Costa Rica. MAT shown as black line with triangles, volcanos shown as red triangles. Arenal Volcano is labelled, as it is the site of a small network of 5 GPS. 'NP' is the Nicoya Peninsula and 'GN' indicates the Gulf of Nicoya.

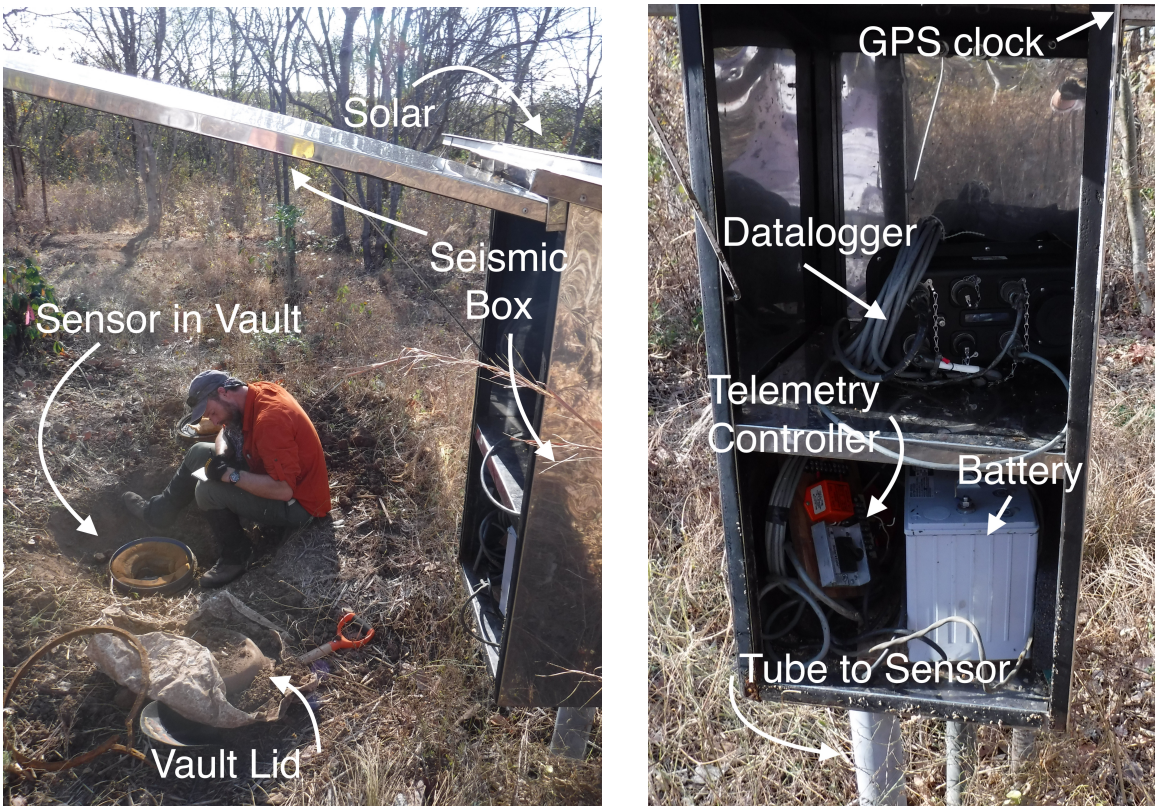

(a) (b)

Figure 1.8: Typical seismic station configuration with buried sensor vault. (a) shows entire site whereas (b) is a zoomed in view of seismic box showing components. Seismic sensor is connected to datalogger by wiring run through a PVC pipe. Timing uses GPS clock. Data are telemetered directly to OVSICORI. System is powered by solar panel and batteries, run through a solar controller.

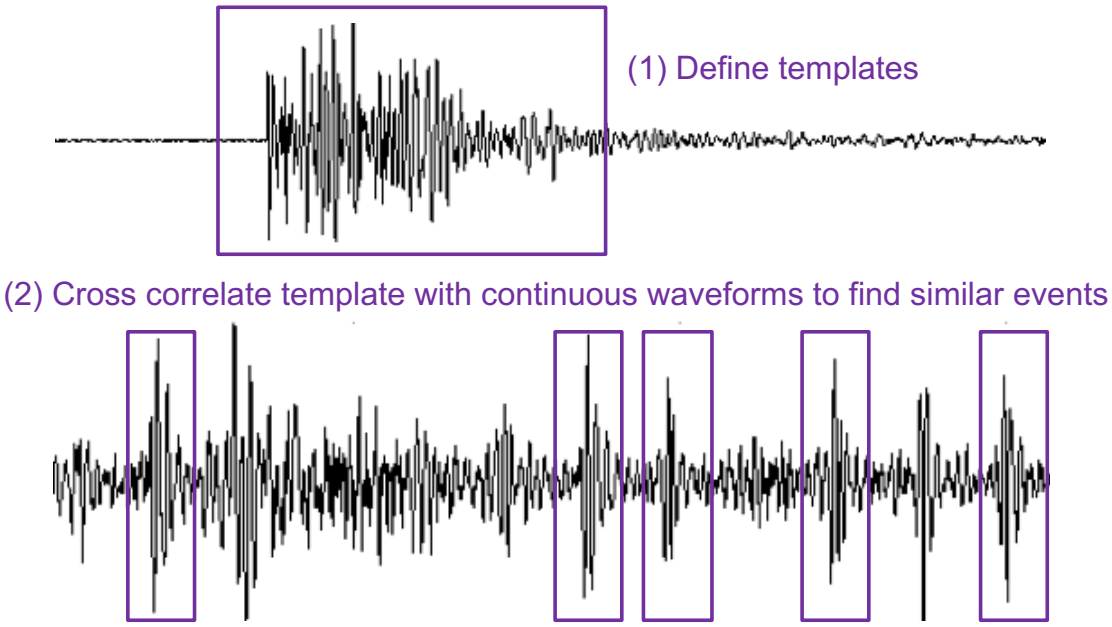

Figure 1.9: Schematic illustration of the WMF technique. Template events are used to detect other earthquakes from within a continuous waveform, using cross correlation. When the cross correlation coefficient is very high the events are said to be repeating events, sharing a common source and path to generate an almost identical waveform.

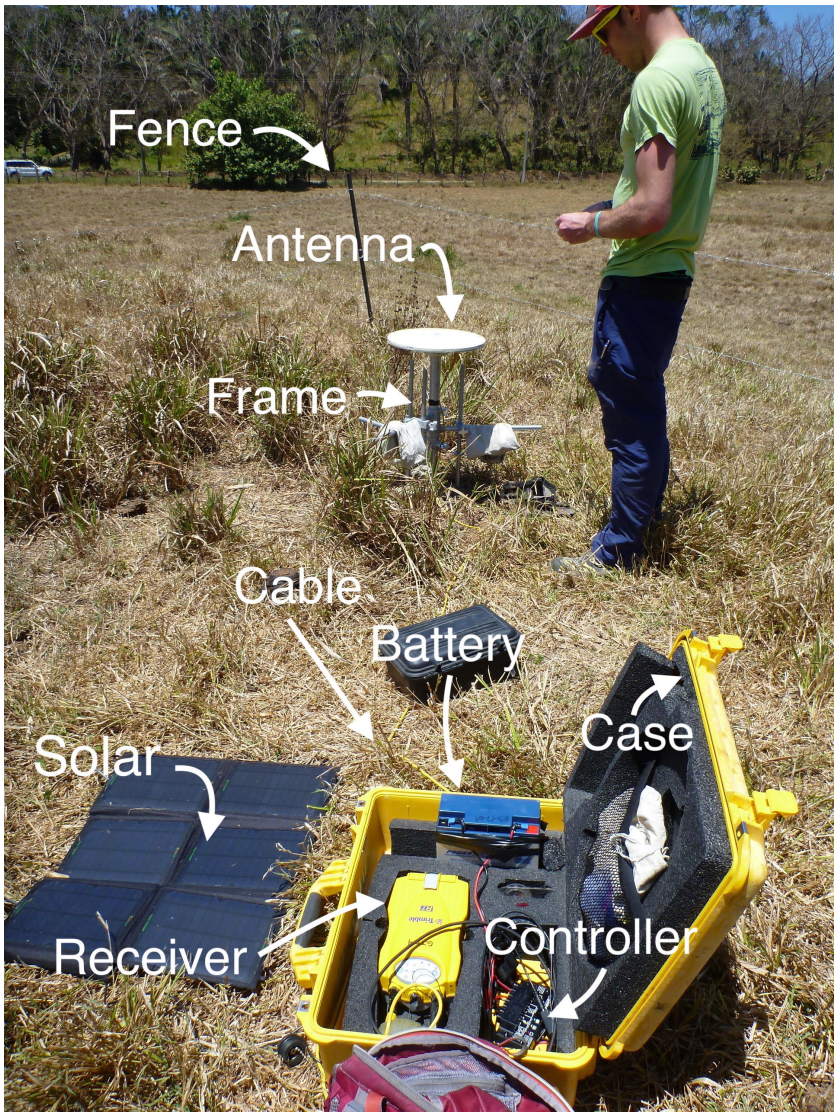

Figure 1.10: Typical campaign GPS occupation. Antenna is fixed to monument pin via metal frame, which is leveled and weighted. Coaxial cable attaches antenna to receiver, which is in turn linked to controller. Power system, which is run through the controller, also includes a single battery and flexible solar panel staked into the soil. Temporary fencing shown in background.

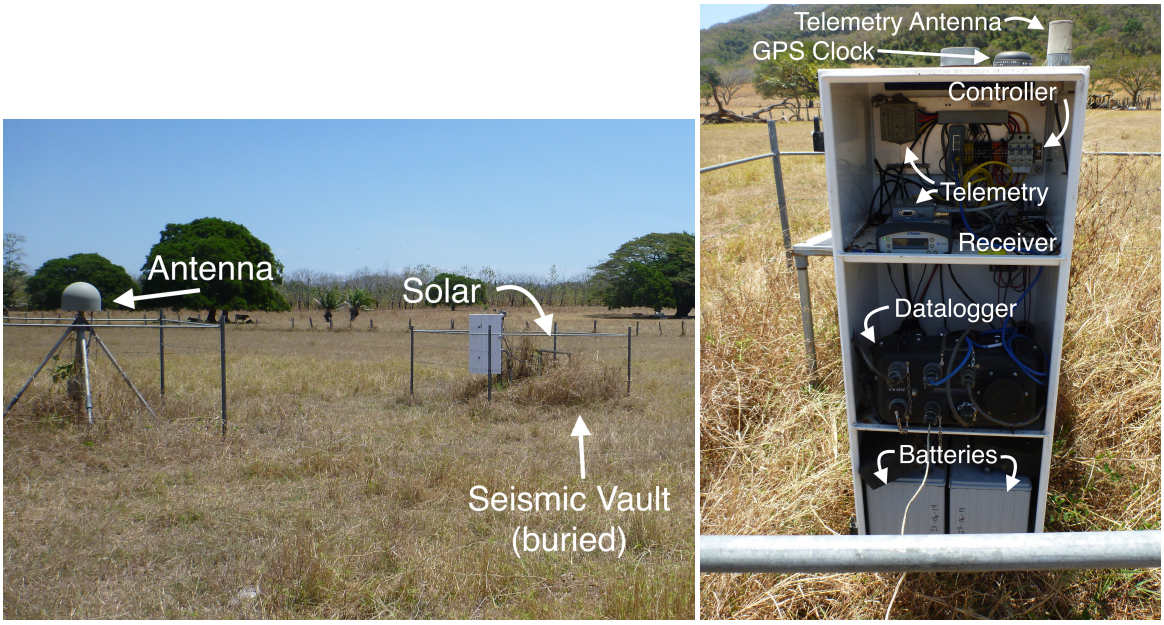

(a) (b)

Figure 1.11: Typical joint continuous GPS and seismic station configuration. (a) shows entire site with solar panels, buried seismic sensor vault and adjacent domed GPS antenna structure. (b) is a zoomed in view of operations box showing components. Seismic sensor is connected to datalogger and GPS antenna is connected to its receiver by wiring run through a PVC pipe. Timing uses GPS clock. Data are telemetered directly to OVSICORI. System is powered by solar panel and batteries, run through a controller.

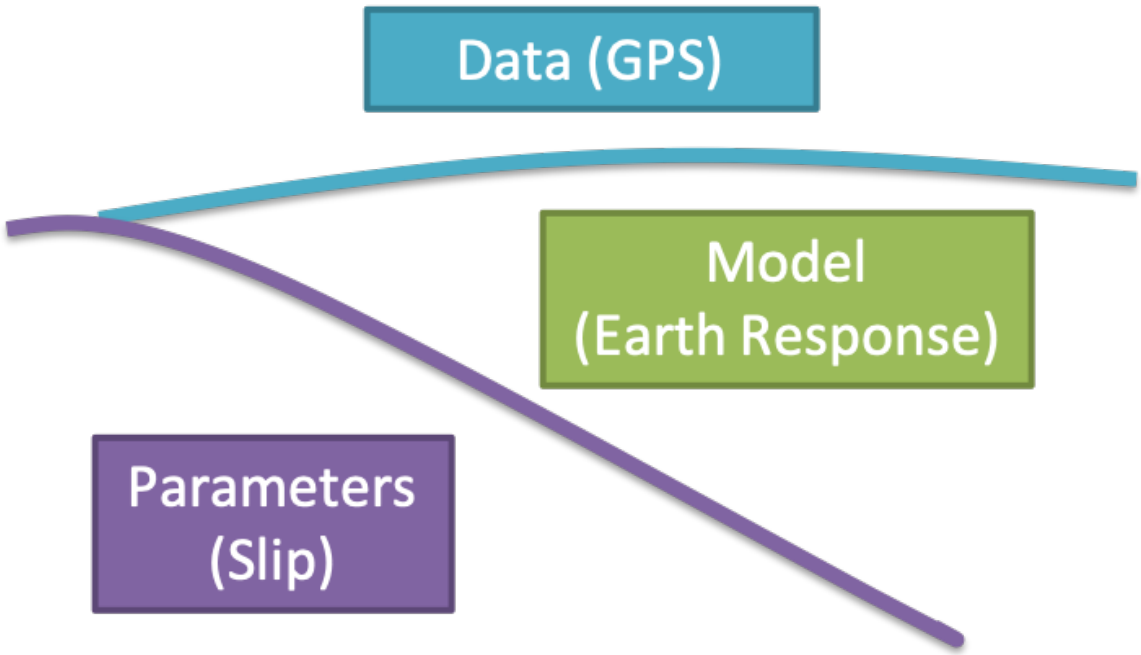

Figure 1.12: Schematic image illustrating the concept of inversion. Whereas forward modeling uses parameters and a model (Green's functions) to synthesize data, inversion uses data and an inverted model to uniquely determine the parameters necessary to have created that data.

Table 1.1: Seismic stations in the Nicoya Peninsula Network (YZ) in 2013.

Name	**Longitude [º]**	**Latitude [º]**	**Sensor Type**	**Sensor Range**
ACHA	-85.2476	9.8280	Guralp CMG3-ESP	Intermediate
ARDO	-85.5964	10.2138	Streckeisen STS-2	Broadband
CABA	-85.3435	10.2362	Streckeisen STS-2	Broadband
GRZA	-85.6356	9.9155	Guralp CMG3-ESP	Intermediate
HATI	-85.7101	10.2922	Sercel L-22	Short Period
HRIU	-85.7502	10.5158	Guralp 6T	Intermediate
INDI	-85.5023	9.8650	Streckeisen STS-2	Broadband
JUDI	-85.5388	10.1659	Guralp CMG3-ESP	Intermediate
LAFE	-84.9351	9.8132	Guralp 6T	Intermediate
LEPA	-85.0312	9.9453	Sercel L-28	Geophone
MANS	-85.3811	10.0985	Sercel L-22	Short Period
MURC	-85.7300	10.9008	Guralp 6T	Intermediate
NARJ	-85.5438	9.9722	Guralp CMG-3T	Broadband
PNCB	-85.0917	9.5895	Streckeisen STS-2	Broadband
PNE2	-85.8291	10.1955	Sercel L-28	Geophone
POPE	-85.2634	10.0634	Guralp CMG3-ESP	Intermediate
PUJE	-85.27247	10.11399	Sercel L-28	Geophone
SAJU	-85.7105	10.0672	Nanometrics Trillium 240	Broadband
SARO	-85.6158	10.843	Nanometrics Trillium 120	Broadband

Table 1.2: GPS stations in the Nicoya Peninsula Network between 2012 and 2017. Does not include Fault Transect described in Section 1.3.1, or Arenal Volcano Network.

Station	Longitude	Latitude	Type
ACOS	-84.6023	10.5485	Campaign
BAGA	-85.2612	10.5414	Campaign
BALL	-85.4484	10.3834	Campaign
BIJA	-84.5769	9.7500	Continuous
BON2	-85.2025	9.7645	Continuous
BONG	-85.2069	9.7438	Campaign
CABA	-85.3435	10.2379	Continuous
CABU	-84.7756	10.1358	Campaign
CEBA	-85.7761	10.2491	Campaign
COBA	-85.1069	9.6881	Campaign
CRUZ	-85.6337	11.0543	Campaign
DIRI	-85.6106	10.2718	Campaign
ELVI	-85.4458	10.3947	Continuous
EPZA	-85.5681	10.1409	Continuous
GRAN	-85.6530	10.5622	Campaign
GRZA	-85.6356	9.9155	Continuous
GUA2	-85.4501	10.1401	Campaign
GUIO	-85.6585	9.9231	Campaign
HATI	-85.7101	10.2922	Continuous
HOJA	-85.3824	10.0795	Campaign
HUA2	-85.3517	10.0177	Continuous
IND1	-85.5022	9.8646	Continuous
JICA	-85.1360	9.9751	Campaign
LAFE	-84.9603	9.8071	Continuous
LEON	-85.1868	9.9365	Campaign
LEPA	-85.0312	9.9454	Continuous
LMNL	-85.0533	10.2675	Continuous
MATA	-85.8129	10.3553	Campaign
MIRM	-85.5711	10.0421	Campaign
PALO	-85.2203	10.2415	Campaign
PAQU	-84.9551	9.8322	Campaign
PNE2	-85.8287	10.1952	Continuous
POTR	-85.5691	10.8474	Campaign
PUJE	-85.2725	10.1140	Continuous
PUMO	-84.9667	10.0645	Continuous
QSEC	-85.3573	9.8404	Continuous
SAJU	-85.7106	10.0671	Continuous
SAMA	-85.5488	9.8892	Campaign
SJOS	-84.9482	10.3656	Campaign
SJUA	-85.7569	10.0632	Campaign
TENO	-85.0983	10.6018	Campaign
VENA	-85.7917	10.1611	Campaign
VERA	-84.8690	10.8536	Continuous

CHAPTER 2

LARGE AND PRIMARILY UPDIP AFTERSLIP FOLLOWING THE 2012 M_W 7.6 NICOYA, COSTA RICA EARTHQUAKE

Citation: Hobbs, T.E., Kyriakopoulos, C., Newman, A.V., Protti, M., Yao, D. (2017), *Large and Primarily Updip Afterslip following the 2012 Mw 7.6 Nicoya, Costa Rica earthquake*. Journal of Geophysical Research: Solid Earth, *122*, doi:10.1002/2017JB014035.

2.1 Key Points

- Postseismic deformation is recorded for 3.5 years following the 2012 M_w 7.6 Nicoya earthquake in Costa Rica
- Up to 1.7 m of afterslip is observed at the periphery of coseismic slip and near the Gulf of Nicoya
- Afterslip and aftershocks appear to be anticorrelated and potentially linked to fault properties or subducted structures

2.2 Abstract

We present detailed surface measurements of the first 3.5 years of postseismic deformation following the 5 September 2012 M_w 7.6 Nicoya, Costa Rica earthquake. The dominant signal in the first 2.5 years is uniform horizontal trenchward motion totaling 7-26 cm across 40 stations. Trenchward velocity is strongly diminished by mid 2014 and appears by 2016 to have begun reversing. We invert the first 2.5 years to determine the corresponding afterslip on a detailed 3D interface. Results show significant afterslip both up and down dip of the main coseismic rupture zone, with as much as 1.7 m of offset in two patches at 15-20 km depth and immediately up-dip of the maximum coseismic slip. This updip slip

represents an important mechanism to address unrelieved interseismic locking, although sufficient strain energy remains to generate up to a M_w 7.1 event near the coastline. The afterslip patches are anticorrelated with strongly-clustered aftershocks at the same depth, which is indicative of varying frictional behavior along strike. An additional patch of slip is colocated with reoccurring slow slip events beneath the Gulf of Nicoya. The magnitude of the observed slip, however, cannot be sufficiently explained by the known slow-slip events. Ongoing measurements will be crucial to understanding the relocking process in Nicoya.

2.3 Introduction

In the quest to understand the seismic cycle, much attention is paid to coseismic motions and their potential precursors. While often less destructive, postseismic processes largely control deformation in the years to decades following a large earthquake (e.g. Khazaradze et al. 2002; Hu et al. 2004; Wang, Hu, and He 2012). Postseismic motion results from the combined effects of: afterslip, the aseismic continuation of coseismic motion; poroelastic relaxation, short-lived deformation related to postseismic porefluid flow; viscoelastic relaxation, the long term inelastic response of the mantle to coseismic stress; and relocking, the return to more stable interseismic accumulation of strain energy (Wang, Hu, and He 2012). Accounting for these processes is crucial to accurately estimate the accumulation of stress at later stages of the seismic cycle, that in turn improve assessments for earthquake and tsunami potential. To be reliable, postseismic deformation measurements require techniques sensitive enough to record small changes in position over years to decades that span an area of several thousand square kilometers or more. This is unavailable in the majority of subduction zones, where the seismogenic portion of the fault exists offshore and/or where funding prohibits operation of a temporally and spatially dense network.

Figure 2.1 highlights why the Nicoya Peninsula is particularly well situated to study a myriad of subduction zone processes. The Nicoya Peninsula sits immediately above the seismogenic zone and extends to within 60 km of the trench, allowing measurements

of crustal motions to be taken from much closer to their source regions than would be possible in most other areas (Protti, Güendel, and Malavassi 2001). As a result of this land geometry, Nicoya has been the focus of numerous geophysical investigations over the past 20 years. Previous studies have utilized seismic (e.g. Newman et al. 2002; DeShon et al. 2006; Dinc et al. 2010) and geodetic networks (e.g. LaFemina et al. 2009; Feng et al. 2012; Dixon et al. 2014), ocean drilling (e.g. Vannucchi et al. 2001; Davis, Villinger, and Sun 2015), heat flow measurements (e.g. Harris and Wang 2002; Harris et al. 2010) and geomorphological observations (e.g. Marshall and Anderson 1995; Sak et al. 2009; Protti et al. 2014) to characterize the megathrust in detail.

Convergence of the Cocos and Caribbean plates is sufficiently rapid to generate $M \geq 7$ earthquakes beneath the peninsula roughly every 50 years since 1853 (Protti et al. 1995; Feng et al. 2012). In addition to these larger earthquakes, the Nicoya megathrust exhibits persistent tremor activity and very low frequency microseismicity up- and downdip of the seismogenic zone (Walter et al. 2011; Walter et al. 2013). The low frequency earthquakes and tremor are sometimes coincident with slow slip events occurring about once a year between 2007 and 2012 (Outerbridge et al. 2010; Jiang et al. 2012; Dixon et al. 2014). This measurable complexity of fault behavior has established Nicoya as a rich natural laboratory for subduction zone studies (see `http://nicoya.eas.gatech.edu` for more information).

The most recent large earthquake was the 5 September 2012 M_w 7.6 Nicoya earthquake (Figure 2.1), which was preceded by a 9-day foreshock sequence (Walter et al. 2015). This event nucleated 10 km offshore at 13 km depth along the interface (Yue et al. 2013), with rupture concentrating downdip and beneath the peninsula (Yue et al. 2013; Protti et al. 2014; Liu et al. 2015; Kyriakopoulos and Newman 2016). The approximately 110 by 50 km coseismic rupture area (Liu et al. 2015) is shown by Protti et al. (2014) to roughly align with the region of significant ($\geq$ 50%) previous interseismic locking (Feng et al. 2012). A potential zone of unreleased slip in the Protti et al. (2014) model, located immediately

offshore and north west of the hypocenter (Figure 4b in Protti et al. 2014), was shown by Kyriakopoulos and Newman (2016) to be partially diminished in amplitude and spatial extent when a fully 3D slab geometry is implemented. It is expected that postseismic slip will release much of this remaining strain energy, effectively balancing the slip budget before Nicoya enters a new seismic cycle.

Here we use a novel dataset of campaign and continuous land-based GPS observations on and near the Nicoya Peninsula to measure ongoing postseismic deformation from 2012 to 2016. These data directly record the timing and spatial extent of surface deformation from the combined postseismic processes. Geodetic inversions are carried out and compared spatially against inter- and coseismic fault slip, aftershocks, and cumulative slow slip to establish the contribution of postseismic phenomena to the seismic cycle budget. Insights from well-instrumented locations like Nicoya are critical to understanding seismic cycle behavior in subduction zones like Cascadia (Wang and Tréhu 2016), which have relatively sparse near-trench coverage. In coming years, we expect to record accelerating landward motion as the subduction zone re-enters an interseismic state.

2.4 Methods

2.4.1 Data Collection

Following a post-earthquake deployment in 2012, field work was again completed in March 2015 and 2016 on the Nicoya Peninsula to obtain new campaign GPS data. By returning to these sites at the same time each year we minimize most seasonal variations that could otherwise affect GPS calculations. In the field campaign from March 6-19, 2015, GPS data were collected at 31 stations on and around the Nicoya Peninsula and Arenal volcano, with instruments recording continuously for 2-3 days at a 30 second sampling interval. Of interest to this study is the subset of 22 stations for which there are previous campaign data taken in 2012 right after the earthquake (Figure 2.2a, details provided in Table 2.1 and 2.2). Post-processing of the raw data is completed using the precise point positioning software

"GIPSY-OASIS", made available by the Jet Propulsion Laboratory (JPL). Final fiducial-free daily solutions are determined using precise satellite orbits provided by JPL and ocean loading coefficients from the FES2004 hydrodynamic model (Letellier 2005), with ambiguity resolution handled by AMBIZAP (Blewitt 2008). March 2016 measurements followed the same procedure for a subset of 7 campaign sites in the central peninsula, focusing on stations with poorer coverage during the 2015 campaign (Figure 2.2b).

These data follow the most recent prior campaign conducted in 2012, in rapid response to the 5 September 2012 Nicoya earthquake (Protti et al. 2014). Instruments were deployed between September 8-22, 2012, with all units recording a minimum of 3 complete Coordinated Universal Time (UTC) days. Several stations (COBA, DIRI, GUIO, MATA, and MIRM) were left in continuous mode to measure several consecutive months of postseismic deformation. In addition to campaign measurements, data were also collected from a network of 18 continuously recording GPS stations on and near the Nicoya Peninsula. This network is operated by the University of South Florida University of South Florida (USF) and the OVSICORI, with technical support from UNAVCO (Tables 2.1 and 2.2). Shown in Figure 2.3, time series of daily position solutions are created for a subset of continuous GPS station daily solutions for which there was good temporal coverage. It is immediately evident that there is a strongly non-linear displacement in the first several months, which flattens out at most stations by approximately 2014. By the start of 2015 most stations appear to show a gentle reversal in direction of their initial post-seismic motion, continuing until at least the end of the time series (31 May 2016).

Due to the sparsity of the data points for campaign measurements, non-linear post-seismic velocities cannot be well-constrained at each site. Instead, cumulative offsets are computed at all 40 stations by differencing start and end positions for the time periods: 2.5 years from immediately following the earthquake to March 2015, and 1 year from March 2015 to March 2016 (to match timing of campaign measurements). Only daily positions with formal horizontal error of less than 1 cm are used in calculating displacement. Earli-

est postseismic positions are taken as the average position over the first 2 days of available post-seismic recordings, corresponding to the date used in (Protti et al. 2014) to define the end of coseismic displacement. For the 2015 and 2016 campaigns we average over all available days, up to 4. Continuous datasets are sampled using a 4-day window corresponding to the average timing of the campaign measurements. The start period of 2 days was chosen to retain as much of the early postseismic signal as possible. Displacements at each station were converted from ITRF2008 reference frame [Altamimi et al., 2011], to a stable Caribbean plate using DeMets, Gordon, and Argus (2010). Beginning and end times, as well as displacements for each station are given in Table 2.1 for 2012-2015 and Table 2.2 for 2015-2016.

As we do not capture the first hours to days of afterslip, measurements herein are a lower bound on total afterslip, emphasizing the spatial distribution of slip over the course of several years. However, our 2012 'start' date reflects the 'end' date of previous coseismic geodetic studies (Protti et al. 2014; Kyriakopoulos and Newman 2016), allowing for direct comparison between those results and our observed postseismic deformation. For a discussion of earliest afterslip from high-rate GPS please see Malservisi et al. (2015). While we do not account for aftershocks independently, their contribution to total slip is included in and discussed in our results.

2.4.2 Afterslip Inversion

To quantify the subsurface processes responsible for postseismic displacements, we initially assume all postseismic deformation is the result of elastic deformation of the crust caused by slip occurring exclusively on the subduction interface. Cumulative displacements over the 2015-2016 period are not considered for inversion, as the magnitude of deformation is small and the data is limited (Figure 2.2b). GTdef (Chen et al. 2009) is used to perform an inversion of the 2012-2015 surface displacement vectors.

We perform a bounded, weighted linear least squares inversion, similar to previous

Nicoya deformation studies (Feng et al. 2012; Protti et al. 2014; Kyriakopoulos and Newman 2016). For a subduction interface defined by coincident pair nodes, Green's functions are obtained for each node-station pair assuming unit slip on each patch. For surface displacement observations (d) weighted (W) by their errors ($d' = Wd$), the weighted Green's functions ($G' = WG$) are used to solve the linear system $d' = G'm$ for slip on the interface (m) (Jónsson et al. 2002; Feng et al. 2012; Kyriakopoulos and Newman 2016).

Allowing hundreds of fault solutions with independent slips results in an underdetermined problem for the 120 observations available (40 stations, each with 3 components). To allay this and avoid unrealistic variations in slip over small distances on the fault, the full inversion also applies smoothing conditions along strike and dip:

$$\begin{bmatrix} d' \\ 0 \end{bmatrix} = \begin{bmatrix} G' \\ \kappa^2 D \end{bmatrix} m$$

which includes a Lagrangian smoothness weighting multiplier (κ) and the second order Laplacian smoothing operator (D) (for details see Jónsson et al. 2002). In all cases, a Poisson's ratio of 0.25 is assumed over a range of κ values.

Generally model misfit increases with smoothing, resulting in a tradeoff between smoothness of the fault solution and residual error. This leads to a non-unique suite of results, dependent on κ, from which the preferred solution must be selected (e.g. Gubbins 2004). Most commonly the inflection point in a curve of roughness (ρ) versus Root Mean Squared (RMS) misfit is subjectively chosen for a preferred solution, such that additional smoothing produces an unacceptably large increase in misfit (e.g. Jónsson et al. 2002; Chen et al. 2009). Here:

$$\rho = \frac{\sum_i |p_i|}{2N}$$

for $p = Dm$ for each patch, i, for a total of N fault patches, and normally described in cm/km^2.

The inversion is performed first with a simplified, two dimensional (2D) curviplanar geometry consistent with Feng et al. (2012), and then with a detailed fully 3D model consistent with Kyriakopoulos and Newman (2016). We implement high-resolution 3D fault geometry to better represent subduction heterogeneities like the East Pacific Rise-Cocos Nazca Spreading Center (EPR-CNS) transition (Figure 2.1) or potential subducted seamounts (e.g. Protti et al. 1995; Husen, Kissling, and Quintero 2002; Wang and Bilek 2011). Specifically, we use the slab surface of Kyriakopoulos et al. (2015), determined using the Maximum Seismicity Method described therein. This model, which represents the most recent, detailed characterization of the interface is superior in Nicoya where the main coseismic rupture area straddles crustal material of heterogeneous providence (Barckhausen et al. 2001). Due to the higher resolution of the 3D model, we leave details of the model based on the 2D geometry for the electronic supplement and Figure A.1. We present the 2D geometry to highlight that slip details are largely similar between geometries and are not substantially affected by complexity in the topographically diverse 3D interface of Kyriakopoulos et al. (2015). Subsequent discussion will correspond to the 3D model and results.

As detailed in Kyriakopoulos and Newman (2016), the subduction surface is discretized into a Finite Element Model (FEM) with 43 along-strike by 21 along-dip coincident pair nodes, each patch having an area of approximately 5x5 km. Maximum depth varies between 36 km in the south and 67 km at the northern edge, resulting from an angle of subduction which is dramatically steeper in the northern EPR crust (Figure 6a in Kyriakopoulos et al. 2015). Green's functions are subsequently calculated within FEM software, ABAQUS (`http://www.simulia.com/`). For the bounded least-squares inversion, we allow up to 10 m of positive thrust or as strike-slip motion in either direction. These slip limits are several times larger than expected (and ultimately modeled) postseismic slip, and more than a factor of 2 greater than the maximum coseismic slip determined to be about 4.4 m (Protti et al. 2014; Kyriakopoulos and Newman 2016). The edges of the model are permit-

ted to slip freely, except in 'Fixed Surface' inversions where slip is forced to be zero at the trench. We view these two boundary conditions as end member models, while noting that this model and network geometry are unable to resolve between the two.

Spatial recoverability is limited by the distribution of GPS stations on the Nicoya Peninsula. The spatial recoverability is evaluated by performing a checkerboard test using an input grid with a cell size of 20x40 km, comparable to the size of features observed. Starting with an initial model with alternating unit slip patches (1 m), split equally between strike and dip slip components, we add white Gaussian noise corresponding to the calculated GPS errors to the forward model prediction at each site. The resultant displacements, plus error, are used as input for inversions that would ideally recover the initial input checkerboard.

We also consider the model resolution matrix, used to quantify the area over which individual model parameters affect one another (e.g. Gubbins 2004). The resolution matrix, $R = G^{-g}G$ (Menke 1989), is evaluated with the generalized inverse of the weighted, damped least squares problem: $G^{-g} = (G^T W G + \kappa D^T D)^{-1} G^T W$ (Jónsson et al. 2002; Kyriakopoulos and Newman 2016). If the inversion reproduced the true model then R would equal the identity matrix, but in practice the diagonals are somewhat less than 1 with non-zero off-diagonal elements representing dependence between model parameters (Gubbins 2004). The i-th row of the resulting resolution matrix provides a measure of the tradeoff between that parameter and all other j parameters ($j \neq i$), for a specified smoothness weighting. A useful characterization of the resolution matrix is a scalar field of the resolution spread parameter, r, described as:

$$r_i = \frac{L_i}{\sqrt{R_i}}$$

for patch length L_i and diagonals of R given by R_i (Funning et al. 2005). This value, r_i, is useful in visualizing the spatial interdependence of model parameters.

A comparison of our checkerboard testing and the resolution spread parameter is shown in Figure 2.4. We assign 'good' recoverability where the original checkerboard shape can be distinguished, as opposed to locations in which the checkerboard is smeared beyond

recognition. Beneath the 40 postseismic GPS sites at approximately 15-20 km spacing on the Nicoya Peninsula there is excellent recoverability over the western coast of the peninsula. Denoted by the thick purple line in Figure 2.4b, the maximum zone of recoverability extends to within $\sim$ 30 km of the trench and matches approximately with the 25 km resolution contour. This line denotes the points at which parameters on one patch have a tradeoff with parameters on patches in the surrounding 25 km. Any slip outside of this region cannot be appropriately estimated with this dataset and smoothing.

2.5 Results & Discussion

2.5.1 Surface Displacements

For the period for which we have the most complete GPS coverage, 2012-2015, GPS-determined horizontal surface displacements are primarily trenchward with offsets between 7 and 26 cm. As described in Wang, Hu, and He (2012), we expect that afterslip will cause wholesale seaward motion, while viscoelastic relaxation should increasingly push coastal stations landward and inland stations seaward. Accordingly, any seaward motion of coastal sites is likely to be the result of afterslip rather than relaxation. Large seaward displacements near the coast suggest that afterslip is occurring, and at least in the shallow subduction zone, may be a dominant mechanism operating over this period.

Comparing velocities over the last year of observation (Table 2.2) to late interseismic velocities of 15-25 mm/yr NNE (Table 1 of Feng et al. 2012), we identify that a transition to pre-seismic convergence rates has not yet occurred. As megathrust coupling reinitiates we should again expect to observe a transition from seaward to landward surface velocities, that should eventually approximate the prior interseismic rates, with clear landward motion initiating at coastal sites and propagating inland (Wang, Hu, and He 2012). In contrast, the 2015-2016 period shows dominantly trench-parallel motion of 4-27 mm/yr NW. Convergence, though not yet returned to interseismic rates, suggests that afterslip is ceasing and that there are likely overlapping contributions from minor continued afterslip, early

relocking, and viscoelastic relaxation to the observed surface deformation field.

2.5.2 Afterslip Inversion

We explored a range of κ values for this inversion (Figure 2.5), choosing the preferred κ value of 9000 near the inflection point in our models. This point is similar in both the freely-sliding and fixed surface models, because deviations in model results primarily occur in the near-trench environment where our data are insensitive to model variability; differences in parameters are outside of the area of recoverability. To demonstrate the effect of over- or undersmoothing, Figure 2.5 includes slip results for κ of 4000 and 18000, inset top right. While the maximum amount of slip varies only slightly between these three models, the rougher solution contains several segments of slip in small patches while the smoother solution averages slip over large areas to produce a map with only three slipping patches. The two patches of slip on the seaward coast of the peninsula remain in all three cases and are considered robust. Only the preferred result will be discussed further. We compare our observed surface displacements with those predicted from the freely-sliding trench inversion (Figure 2.6). Generally, the horizontal displacements are well matched while the smaller vertical vectors are more variable. Results are similar for the fixed surface model (Figure A.2).

Within the zone of recoverability, slip inversion results display a maximum of 1.7 m of reverse slip. This is true of both the freely-slipping and fixed trench surface cases (Figures 2.7 and 2.8, respectively). Fixed and freely-slipping boundary conditions both have a cumulative postseismic slip Moment (M_o) of 2.0 x 10^{20} Nm (M_w 7.5) inside the zone of recoverability, assuming rigidity of 30 GPa, with comparable RMS residuals (14.54 and 14.56 mm; Figure 2.5). The primary difference between these cases lies outside of the zone of recoverability (denoted by thick purple line in Figures 2.7 and 2.8), with more shallow slip suggested by the freely-slipping trench case. While we do not have data sufficiently close to the trench to determine the existence of slip there, Davis, Villinger, and Sun (2015)

use pressure changes from the time of the mainshock until the end of 2013 to estimate up to 0.76 m of postseismic slip at the toe. We therefore consider these two results as end members, but prefer the freely-slipping (non-fixed) trench model (Figure 2.7).

Three patches of significant afterslip both up and downdip of the coseismic rupture area (pink contour) are imaged in Figures 2.7b and 2.8b. The strongest slip is near the coastline in two distinct patches at roughly 15-20 km depth on either side of the EPR-CNS transition, with some slip extending seaward along the transition. Downdip there is a diffuse zone of up to 0.7 m slip, running parallel to strike between roughly 25-50 km depth. Lastly, a region of slip is imaged in the south end of the zone of recoverability, beneath the Gulf of Nicoya, with a maximum of 0.9 m of slip at 15-40 km depth.

2.5.3 Comparison to Aftershocks

Afterslip is a response to unrelieved interseismic stress and any additional coseismically induced stresses that are commonly thought to at least partially drive aftershocks (e.g. Hsu et al. 2006; Chan and Stein 2009; Helmstetter and Shaw 2009). If coseismic slip is assumed to drive postseismic behavior, then the occurrence of either aftershocks or afterslip is likely the result of differing frictional parameters on the fault surface. Afterslip is thought to be the preferred release mechanism for velocity-strengthening materials whereas aftershocks nucleate where the surface is velocity-weakening (e.g. Marone, Scholtz, and Bilham 1991; Helmstetter and Shaw 2009). This hypothesis requires the observed postseismic behaviors to be spatially separated at any point in time. To explore the veracity of this idea in the current case, we compare our preferred afterslip model with the aftershock distribution of Yao et al. (2017). This catalog contains 7747 events over 4 months from the 5 September mainshock to the end of 2012, with local magnitudes (M_L) up to 5.7 (corresponding to the largest M_w 6.4 aftershock). To reduce noise associated with more poorly determined events, we evaluate a subset of the catalog with a minimum of 10 associated P and S wave arrivals, each, and a formal RMS error of less than the average plus one standard deviation. The

resulting subset of 5381 events is plotted in Figures 2.7a and 2.8a, along with the repeating earthquakes of Yao et al. (2017).

Near the peninsula, the majority of aftershocks are concentrated in clusters immediately southeast of the EPR-CNS boundary near the "elbow" of the coastline and at the southern tip of the peninsula near Cabo Blanco Park. Notably both aftershock clusters have experienced episodic tremor prior to the 2012 earthquake (Walter et al. 2011). Areas of strong updip afterslip near the coastline are bounded laterally by aftershock clusters, with little aftershock activity in the regions of greatest afterslip. A similar anti-correlation of aftershocks and afterslip was previously observed for the 2004 Parkfield and 2005 Nias earthquake (Hsu et al. 2006), with the former being interpreted as the result of frictional properties that vary along strike (Barbot, Fialko, and Bock 2009). It is likely that the same is occurring at Nicoya over depths of 15-20 km where the anticorrelation is strongest. Almost all repeating earthquakes are located in this same depth range, although they also appear to be anticorrelated with strong afterslip. This is an unexpected finding, given that the current literature on repeating earthquakes suggests that they are commonly the result of small patches of slip-weakening material embedded within a broader slip-strengthening region (e.g. Nadeau and McEvilly 1999; Beeler, Lockner, and Hickman 2001; Chen and Lapusta 2009). The notion that these repeaters are the result of surrounding aseismic slip has even been implemented by Uchida and Matsuzawa (2013) to use repeating aftershocks as a proxy for afterslip following the 2011 M_w 9.0 Tohoku-Oki earthquake. It appears, however, that this technique is not uniformly applicable to all small, repeating aftershocks.

Over the coseismic depth range of roughly 20-30 km we see more distributed aftershocks occurring, albeit with a lower density of events than immediately above. This is consistent with a sustained velocity-weakening behavior in the seismogenic zone over the postseismic period. The shallowest 10 km of the subduction interface also experiences diffuse but poorly located aftershocks, while in the 10-15 km and 30-50 km range there is little observed seismicity and only modest afterslip. Total moment from aftershocks is not

calculated (Yao et al. 2017), but their contribution to slip is included in estimates herein.

Interseismic seismicity, as recorded by the CRSEIZE experiment (DeShon et al. 2006), is more dispersed along strike despite the majority of interplate events also locating between 15-20 km depth. This suggests that slip-strengthening behavior may be ephemeral at this depth, being initiated by the 2012 earthquake.

2.5.4 Comparison to Inter- and Coseismic Slip

When examining the entire seismic cycle 'slip budget' on the subduction interface, it is crucial to consider the spatial relationship of locking, coseismic slip, and afterslip. In the along-dip direction, afterslip occurs both above and below the coseismic slip region, with maximum afterslip (1.7 m) nearly one-half of the observed coseismic slip (4 m) (Kyriakopoulos and Newman 2016). Likewise, the moment released by afterslip within the region of recoverability (M_o = 2.0 x 10^{20} Nm, M_w 7.5) is about one-half of that observed coseismically (M_o = 3.7 x 10^{20} Nm, M_w 7.6) (Kyriakopoulos and Newman 2016). Following the 2012 earthquake, Protti et al. (2014) observed that a portion of the interseismically locked area just offshore remained unruptured during the mainshock (Figure 2.7b and 2.8b). While we observe that a large segment has slipped during the postseismic phase, a portion appears to remain locked. To quantify this, we estimate the spatial distribution of slip deficit since the most recent prior Nicoya megathrust earthquake.

Using a constant convergence at 83 mm/yr (DeMets, Gordon, and Argus 2010) and the interseismic locking model of Kyriakopoulos and Newman (2016), based on Feng et al. (2012), the maximum accumulated slip from 1950-2012 in regions of 100% coupling is estimated to be 5.15 m. From this we subtract coseismic slip ofKyriakopoulos and Newman (2016), based on Protti et al. (2014) and our preferred afterslip model. The total remaining moment at seismogenic depths between 10 and 30 km is M_o = 2.0 x 10^{20} Nm (M_w 7.5), and includes contributions from several patches (Figure 2.9). This value is likely an overestimate as it does not explicitly account for slip associated with intermediate sized

earthquakes (e.g. 1978, 1990), and assumes the late-interseismic locking as observed between about 2000 and 2010 to be constant through the interseismic period. Furthermore, slow slip events, which are implicitly included if they occurred during the observed late-interseismic period, may too change over time. Beneath most of the peninsula, it appears that interseismic strain energy is largely relieved by coseismic and postseismic slip, with $<$1 m residuals. However, a large slip deficit ($>$3 m) remains within the southeastern edge of the zone of recoverability. This overlaps a region of frequent slow slip (discussed in following section) and the 1990 M_w 7.0 earthquake at the entrance to the Gulf of Nicoya (Protti et al. 1995), which likely accounts for some of the deficit reported here.

Directly beneath the elbow of the peninsula (Punta Guiones), the approximate transition between EPR and CNS crust and the location of intense aftershock seismicity, we find more than 2 m of slip deficit still remains. As an update from the Protti et al. (2014) result, we find the patch of unresolved slip near Punta Guiones to have 5.3 x 10^{19} Nm of unrecovered moment, capable of up to an M_w 7.1 earthquake (indicated by pink polygon, Figure 2.9). While such an event certainly has an increased tsunami potential over the prior under-land rupture in 2012, we suspect it is unlikely to extend significantly toward the trench like the destructive 1992 Nicaragua tsunami earthquake that occurred immediately northwest of the Nicoya Peninsula (e.g. Kanamori and Kikuchi 1993; Satake et al. 1993; Ihmlé 1996). The lack of significant seismogenic coupling in this region, supported by seafloor pressure data of Davis, Villinger, and Sun (2015), suggests slip is being relieved aseismically near the trench.

2.5.5 Comparison to Slow Slip

The approximately 0.8 m of afterslip at the southernmost, downdip extent of the peninsula near the entrance to the Gulf of Nicoya, though possibly biased by the edge of the model, is intriguing. Nearby continuous GPS sites show a clear temporary reversal in very early 2014 and another potential event in 2015 (Figures 2.3, A.3) – transient southwestward

displacement consistent with the direction of coseismic, postseismic, and previous SSE displacements. This location has experienced SSEs in 2007, 2009, as well as in 2012 prior to and concurrent with the Nicoya earthquake (Dixon et al. 2014). Voss et al. (2017) find up to 0.14 m slip in the Gulf of Nicoya area during the 2014 SSE, accounting for only 18% of the observed afterslip in the Gulf. This suggests that afterslip and SSEs are both occurring in this region, which may be associated with a subducting seamount that nucleated the 1990 M_w 7.0 earthquake in the Gulf of Nicoya (Protti et al. 1995).

Frequent aseismic slips along the Nicoya margin may help relieve stored strain energy, and is likely tied to elevated fluid pressures. Extremely high Vp/Vs (Audet and Schwartz 2013) and abruptly reduced seismic velocities following the 2012 mainshock (Chaves and Schwartz 2016) indicate forearc pore pressures that may approach lithostatic, effectively weakening the upper plate and allowing slow slip events approximately every 1-2 years unless loaded coseismically (Audet and Schwartz 2013; Dixon et al. 2014).

2.5.6 Potential Anelastic Contributions

An elongate and diffuse region of up to 0.7 m of slip is observed near the downdip edge of the study region, with slip at depth greater than 30 km accounting for 22% of the total afterslip moment within the zone of recoverability. While our modeled slip may accurately represent elastic behavior of the subduction interface just downdip of coseismic slip, it is also likely that there is an appreciable anelastic contribution. Malservisi et al. (2015) found that the 2-year postseismic GPS time series across 18 continuous stations on the peninsula are well fit by combined relaxation functions with characteristic timescales of 7, 70, and greater than 400 days, suggesting contributions from poroelastic deformation, afterslip, and downdip viscoelastic relaxation, respectively. We identify that this idea is supported by the paucity of aftershock activity below $\sim$ 30 km depth (Figures 2.7b and 2.8b), although the CRSEIZE experiment recorded seismicity at these depths during the interseismic period (DeShon et al. 2006). A detailed tomographic model, developed by

DeShon et al. (2006), estimated that the Mohorovičić discontinuity intersects the slab at 30-40 km beneath Nicoya, updip of our observed deep afterslip.

Postseismic viscoelastic relaxation is expected following large megathrust events, though the relative proportions of relaxation and afterslip are difficult to determine due to their shared seaward motion of the upper plate (Wang, Hu, and He 2012). Because the current model assumes all deformation is on-fault and elastic, we are similarly unable to resolve between deep fault slip and distributed relaxation of the upper mantle. Estimates herein of deep afterslip should therefore be taken as an end member behavior. Evaluating the anelastic component of postseismic deformation will become increasingly important when considering longer time periods leading toward relocking of the megathrust.

Similarly, this model also makes no attempt to model poroelastic relaxation. While Malservisi et al. (2015) posit a short-period relaxation signal consistent with poroelastic effects, modeled displacements from poroelastic rebound were found to be significantly smaller than the displacements associated with that 7-day relaxation and directionally inconsistent with poroelastic stressing. We suspect that the poroelastic effect is likely to be only a modest contribution as compared to the dominant afterslip signal observed over the 2.5-year period.

2.5.7 Spatially Variable Fault Behavior on the Nicoya Megathrust

Synthesizing all of our observations about slip, there are substantial differences in afterslip along strike and dip. At the 15-20 km depth range along the entire Nicoya Peninsula, postseismic activity appears as either afterslip with little seismicity or as aftershock clusters with little observed cumulative slip. Given that this band experiences spatially similar loading by stress heterogeneities at the edge of the coseismic rupture area, such variable slip behavior along strike must be the result of changes in thermal, geological, frictional, and/or structural regime.

The thermal state of the Nicoya Peninsula is dominantly controlled by the change in

provenance of the oceanic crust between relatively warm CNS and abnormally cold EPR material (Harris and Wang 2002; Hutnak et al. 2007). Afterslip and aftershocks nucleating at the same depth along the southern CNS crust, where temperatures should be fairly constant, suggests that the spatial separation of afterslip and aftershocks at the same depth is not significantly thermally controlled. Similarly, hanging wall lithology is consistent in the along-strike direction across the Nicoya Peninsula (Bourgois et al. 1984) and subducting crusts are similar ages even across the EPR-CNS suture (Barckhausen et al. 2001). This suggests no substantial age-related or lithologic control.

Rate-and-state friction dictates that when a sufficient stress is applied to a fault it will fail seismically or aseismically depending on whether the interface material is velocity-weakening or velocity-strengthening, respectively (e.g. Dieterich 1972; Ruina 1983; Scholz 1998). If the subduction interface is velocity-weakening near Punta Guiones (elbow in coastline), it would resist slipping aseismically and instead nucleate aftershocks in a region surrounded by stress heterogeneities in the down dip and lateral directions. A similar contrast in frictional parameters in the along strike direction was previously observed by Barbot, Fialko, and Bock (2009) for the 2004 Parkfield earthquake, where afterslip was anticorrelated with aftershocks, and explains the disconnected nature of afterslip patches near the coast.

Other than the clear transition in material origin and thermal state across the downgoing plate, the only other notable difference is the existence of 'subducted topography' along the interface associated with the CNS crust (Kyriakopoulos et al. 2015). As discussed in Yao et al. (2017), aftershock clusters occur along and possibly within the microseismically-defined indenters immediately south of the elbow in the coast (the focus of most coseismic rupture in 2012), as well as near the continuation of the Fisher Seamount chain subducting at the southernmost tip of the peninsula near Cabo Blanco (just north of the 1990 earthquake, indicated in Figure 2.1) (Kyriakopoulos et al. 2015). Subducted seamounts, the most commonly discussed indenter, are often associated with abundant microseismicity

and occasionally larger earthquakes with complex rupture patterns (Wang and Bilek 2011). In the current study, we note that coseismic slip and aftershock activity appears to terminate above approximately 20 km depth, except in zones of significant slab topography, suggesting that topography primarily affects the updip extent of aftershock behavior.

2.5.8 Continuing Postseismic Deformation

Visual inspection of continuous GPS time series shows the postseismic response curve has flattened for many sites (Figure 2.3), suggesting that afterslip and postseismic relaxation may be approaching completion by 2015 (e.g. Wang, Hu, and He 2012). Continued observations are critical as the landward velocities increase toward interseismic values. This process may begin at the toe of the subduction zone and propagate inland, as is now observed in Chile following the 1960 M_w 9.5 Valdivia earthquake (Wang et al. 2007), rendering coastal observations particularly crucial for understanding the exact timing of relocking. This coastal initiation of landward motion is thought to be from superposition of both interseismic plate convergence and postseismic viscoelastic relaxation, which is expected to be landward at coastal stations and seaward at inland stations due to the opposing directions of relaxation between the oceanic mantle and mantle wedge (Wang, Hu, and He 2012). Because stress-related postseismic processes largely overlap both temporally and spatially, including afterslip, aftershocks, poroelastic and viscoelastic relaxation, it is difficult to uniquely isolate their individual contributions, particularly when the time scales of some behaviors may be stress dependent (e.g. Bürgmann and Dresen 2008). This can become further complicated later in the postseismic cycle as portions of the interface begin to relock, while others still slip, and postseismic relaxation processes are ongoing — this is where were we find Nicoya in 2015.

Keeping an updated budget of potential slip during the next megathrust event will improve seismic hazard assessments. Current GPS monument configuration may also prove useful for determining the spatiotemporal evolution of the early interseismic pe-

riod, wherein the width of the locked seismogenic zone is expected to narrow as downdip frictional locking decreases (Wang and Tréhu 2016). Evaluating more complex models (e.g. viscoelastic and pore-pressure response, rate-and-state friction law) has improved our understanding of the crustal and mantle response to rapid coseismic loading (e.g. Jonsson et al. 2003; Barbot, Fialko, and Bock 2009; Johnson, Bürgmann, and Freymueller 2009; Hu et al. 2016). Given the ideal geometry and rich data across the Nicoya Peninsula, application of such models to this dataset should provide quantitative estimates of the mantle rheology and characteristic timescale of recovery for Nicoya, ideal for comparison with measurements of megathrusts worldwide.

2.6 Conclusions

Using three and a half years of dense GPS measurements following the 5 September 2012 M_w 7.6 Nicoya Peninsula, Costa Rica earthquake, we identify distinct patterns of spatial and temporal evolution of postseismic deformation. Strong seaward displacements occur over the first 2.5-year period and diminish to almost zero trench-normal velocities by mid-2016. This indicates relocking has initiated, but GPS velocities have yet to return to interseismic rates observed in the decade prior to the mainshock.

Modeled afterslip, using the 3D subduction interface model of (Kyriakopoulos et al. 2015), found up to 1.7 m of motion in two slip patches immediately updip of coseismic rupture, below the western coast of the peninsula. Comparison with afterslip results from a model using the 2D geometry (Figure A.1 and accompanying text) are similar with the 3D results presented herein, suggesting the observed slip distribution is not an artifact of complex model geometry. Aftershock seismicity occurs in two clusters: between these coastal afterslip patches and directly southeast of the southern patch, forming a 15-20 km deep band of strong postseismic activity running the entire length of the peninsula. Differences in behavior along this band may be tied to varying frictional properties and/or the distribution of subducted topography. A region of deeper slip imaged at the downdip edge of

coseismic rupture may be real or could be the result of unmodeled viscoelastic relaxation. At the southeast edge of the study area, near the Gulf of Nicoya, another patch of significant afterslip exists near the locus of several slow slip events. One such event in 2014 is thought to account for less than 20% of the cumulative slip in this region, thus significant afterslip is still required to explain most deformation.

Ultimately, afterslip and aftershocks are spatially distinct, and primarily outline the updip edge of the 2012 coseismic rupture. While some aftershocks are seen to be repeating (Yao et al. 2017), the spatial distribution of aftershock behavior is insufficient to describe the afterslip signal.

Future measurements with this network will provide insights about the relocking and early interseismic behavior along this megathrust. Such details are useful for comparison with other subduction zones without such favorable land geometry, as well as for estimation of seismic and tsunami hazard in Costa Rica as the Nicoya megathrust enters another seismic cycle.

2.7 Acknowledgement

All GNSS data is available through UNAVCO archives (`http://unavco.org`). Model outputs are available from the Nicoya Seismic Cycle Observatory (`http://nicoya.eas.gatech.edu`).This project is funded through NSERC PGSD2-488063-2016 to T.E.H. and NSF 1447104, 1262267 to A.V.N. Figures prepared using Generic Mapping Tools (GMT) and Matlab. Field work would not have been possible without support from UNAVCO and OVSICORI, and the assistance of J. Buffo, B. Burgoa, K. Gardner, M.S. Kemmerlin, J. McAdams, C. Muller, and A. Williamson.

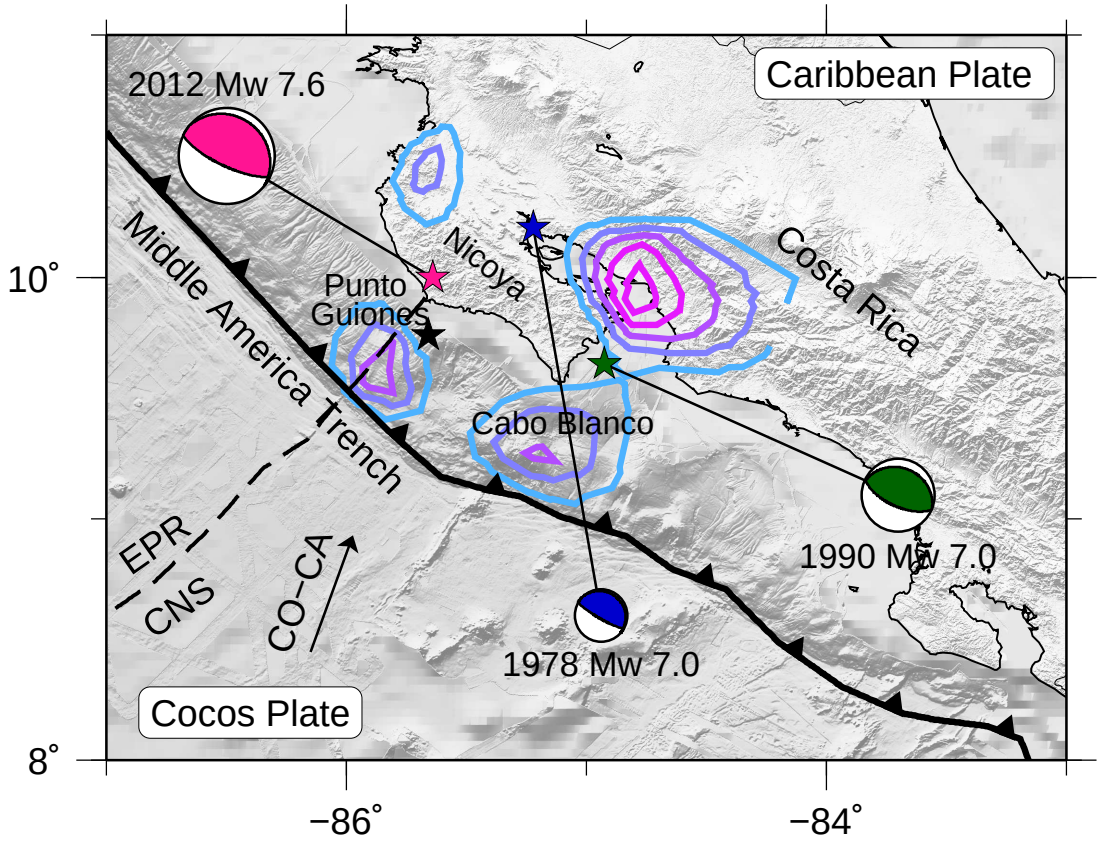

Figure 2.1: Tectonic configuration of Nicoya study area, with Cocos Plate subducting beneath Caribbean Plate along the MAT in azimuth shown at a rate of 7.7 cm per year [DeMets et al., 2010]. Transition is shown from oceanic crust sourced at the EPR and CNS (Barckhausen et al. 2001). At this location there is a transition from steep subduction of relatively cold EPR crust to the more shallowly downgoing and warmer CNS crust. Cumulative slow slip contours of Dixon et al. (2014) shown from blue to pink in 100 cm intervals. Centroid (Ekström, Nettles, and Dziewoński 2012) and relocated hypocenter (Yue et al. 2013) for 2012 M_w 7.6 Nicoya earthquake shown by pink and black stars, respectively. The 1990 M_w 7.0 Gulf of Nicoya earthquake (Protti et al. 1995) shown in green, and 1978 M_w 7.0 Samara earthquake (International Seismological Centre 2014) shown in blue. Global centroid-moment tensor solutions (Ekström, Nettles, and Dziewoński 2012) shown by beachballs, scaled by magnitude. Fisher Seamount Chain can be seen from bathymetry beneath the word 'convergence', heading toward the southern tip of the Nicoya peninsula.

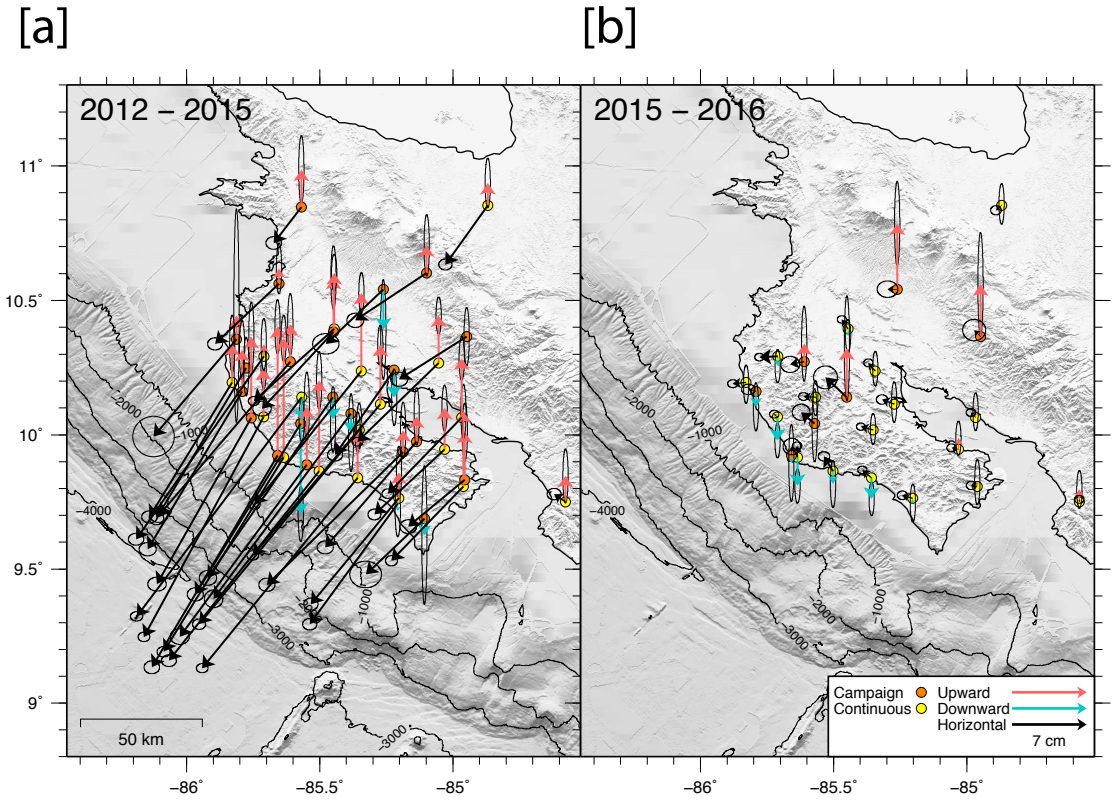

Figure 2.2: Displacement, relative to Caribbean plate, at campaign (orange) and continuous (yellow) GPS sites for 2012-2015 (a) and 2015-2016 (b). Horizontal displacements in black, upwards in red, and downwards in blue. Shown are the 22 available campaign measurements from 2012-2015, compared to only 7 campaign sites successfully occupied in 2016.

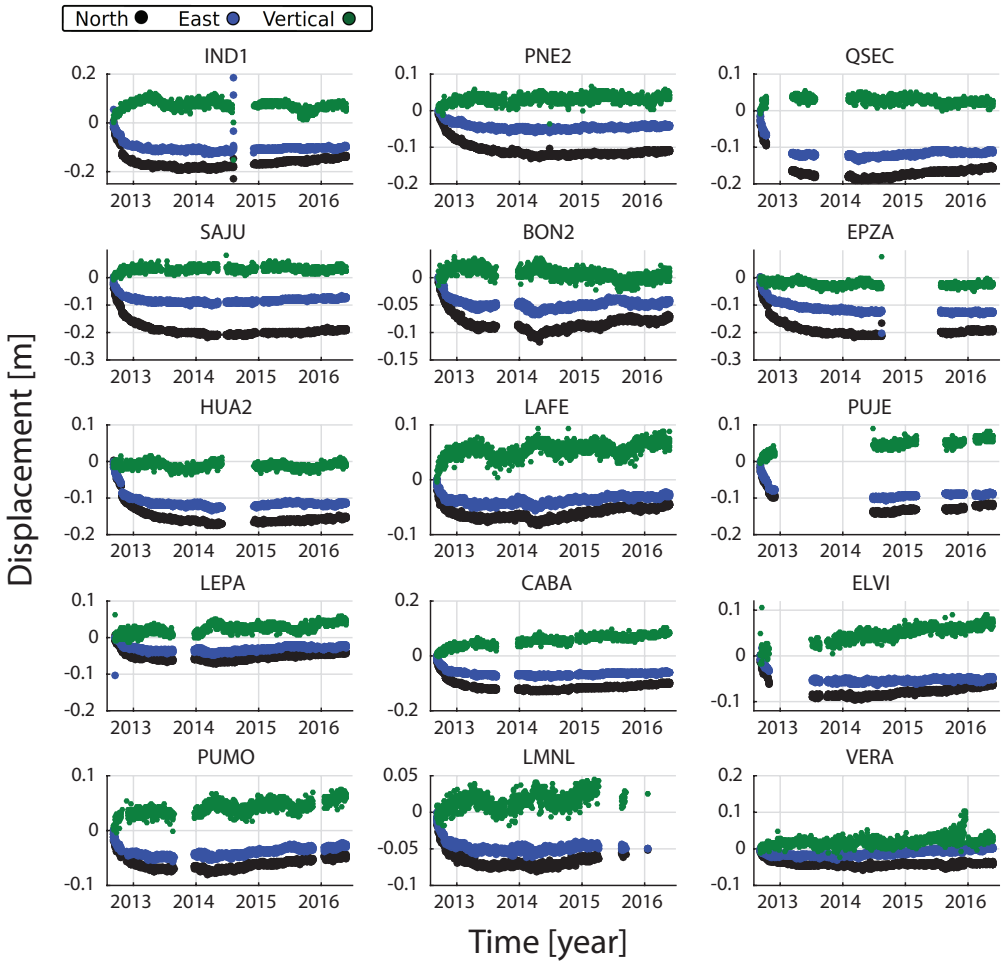

Figure 2.3: Displacement [meters] relative to the first day after the 2012 earthquake for a subset of continuous GPS stations having good temporal coverage. All offsets are given for a fixed Caribbean reference frame. Stations are arranged (left to right, starting from top row and working down) by distance from the trench. North, east, and vertical components are displayed in black, blue, and green, respectively. Postseismic daily displacements are large at first, diminishing with time, and ultimately reversing by approximately the start of 2015. Potential SSEs are visible as short-term reversals in direction of motion.

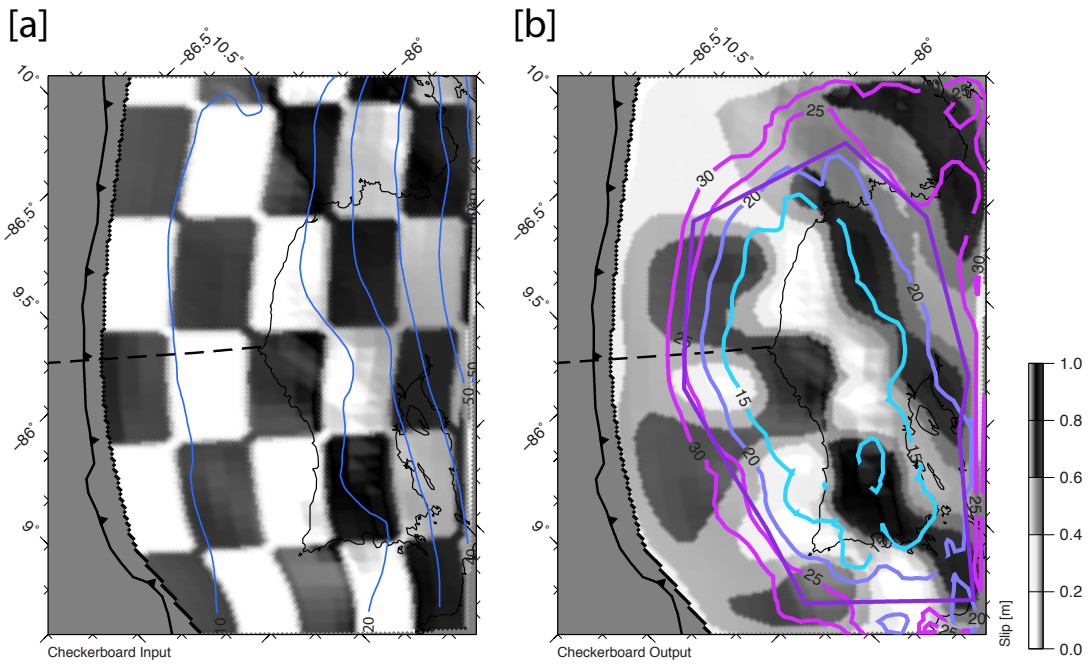

Figure 2.4: Results of checkerboard recoverability testing for input model (a) and resultant slip (b) using preferred smoothing value (κ = 9000). Depth contours are overlain in blue over input slip panel. Output slip panel shows annotated contours of resolvability (in km) as well as a dark purple, angular polygon surrounding area for which there is good recoverability based on checkerboard test. For more information about resolution and recoverability tests please see Section 2.4.2. EPR-CNS suture shown as dashed line, MAT as solid line with teeth.

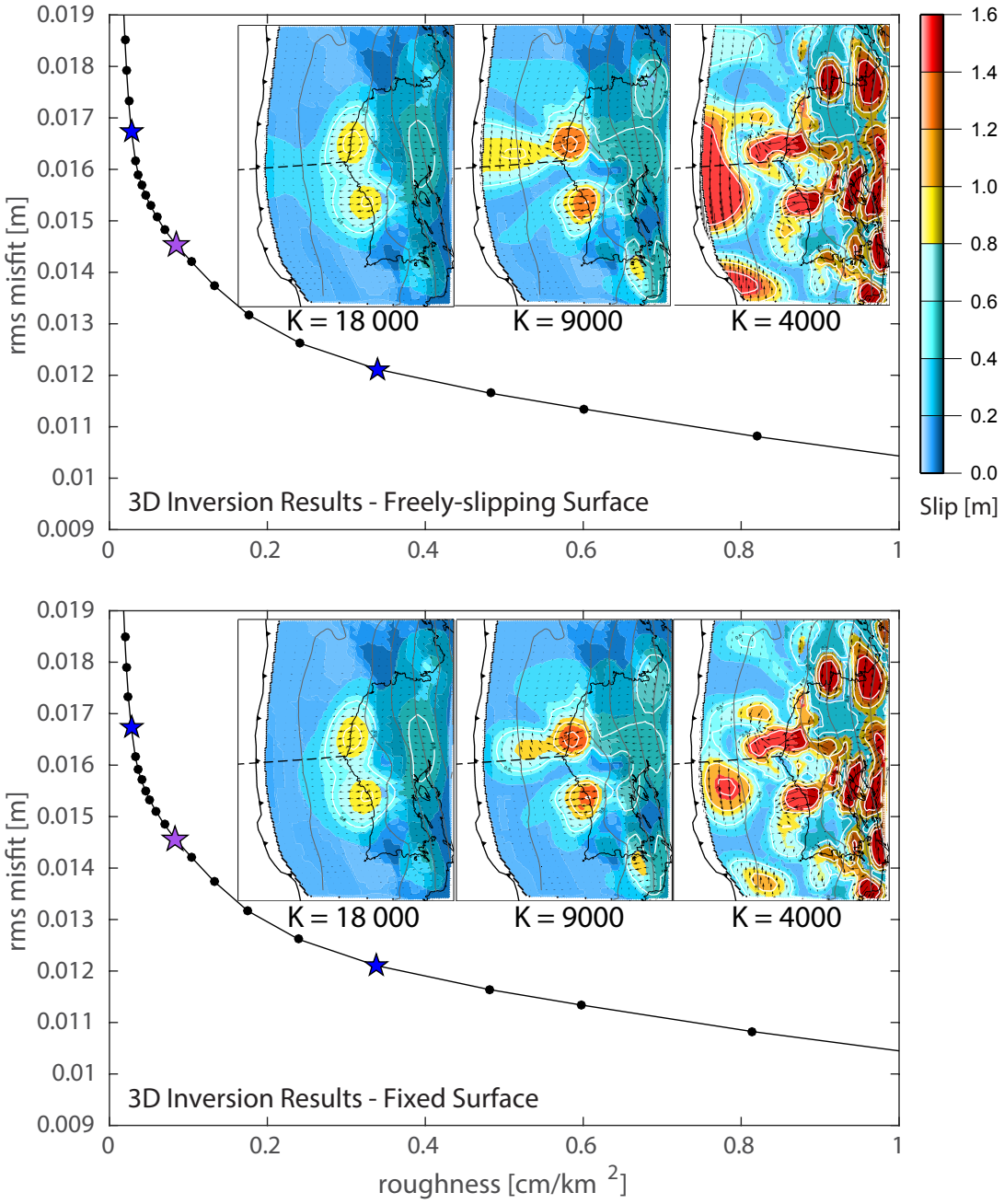

Figure 2.5: Roughness versus misfit for inversion of 2012-2015 GPS displacements. Preferred solution of κ = 9000 indicated by purple star. Blue stars indicate under- and oversmoothed solutions of κ = 4000 and 18000. Resulting maps of afterslip are shown as insets. From left to right they represent oversmoothed, preferred, and undersmoothed results.

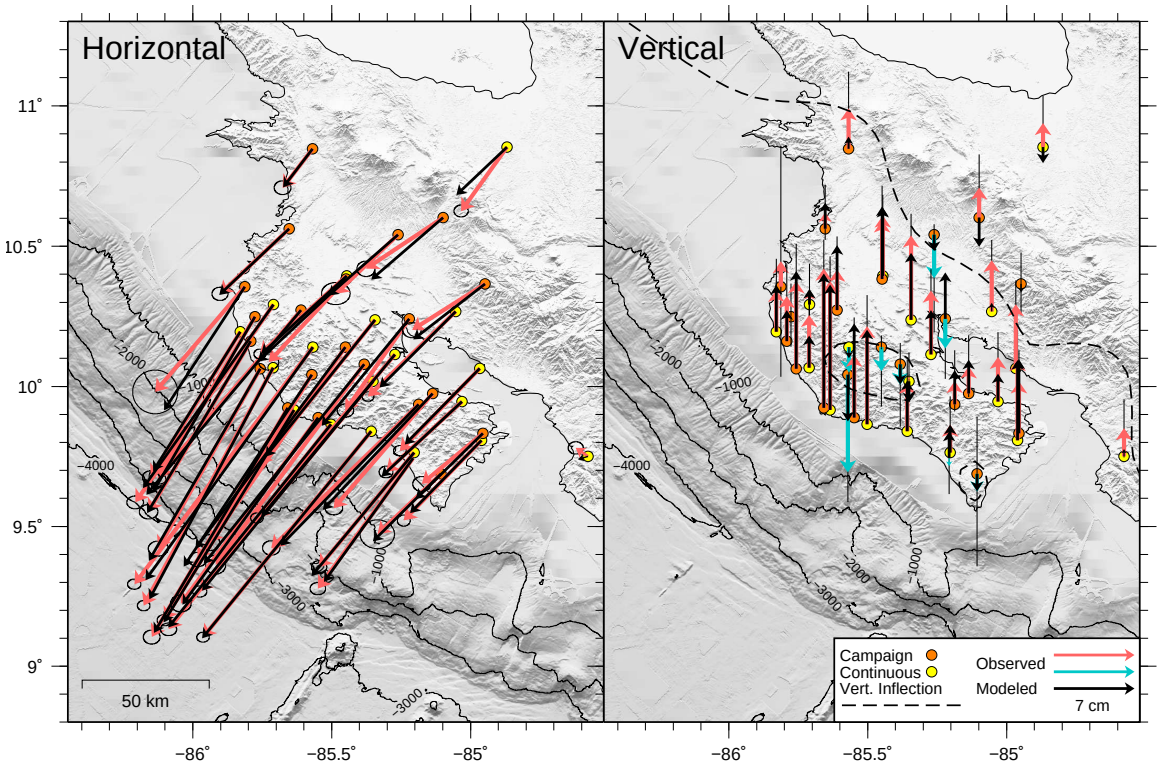

Figure 2.6: GPS displacements for 2012-2015 time period, shown for comparison against model predictions for preferred slip result with free surface. Observations shown by colored arrows, with predictions indicated by black arrows. Left panel shows horizontal displacement, right shows vertical. Dashed line in right panel shows modeled zero vertical deformation, separating uplift from subsidence.

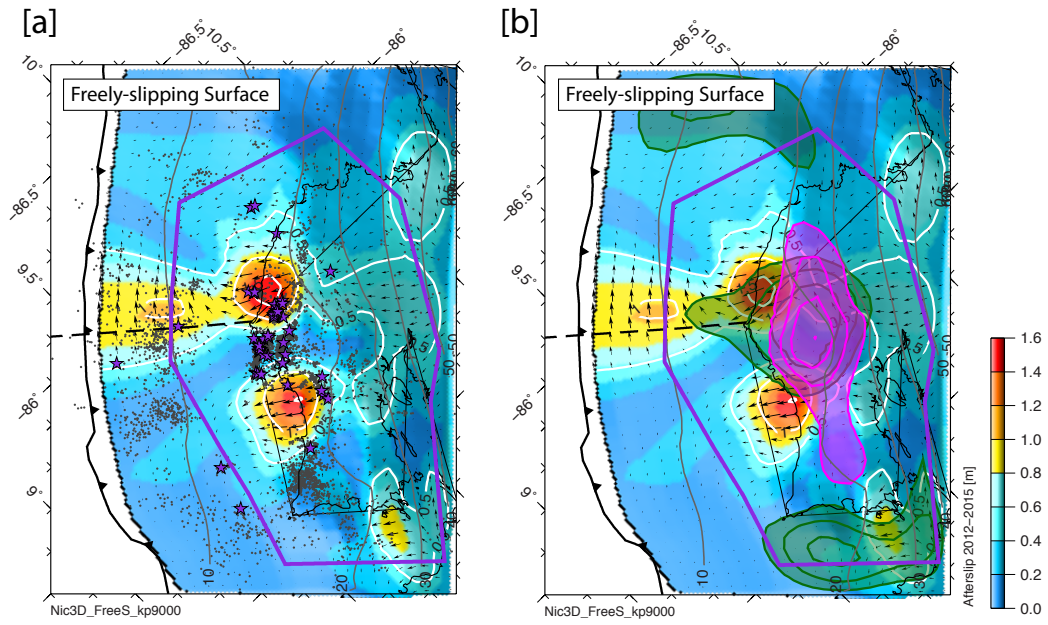

Figure 2.7: Both panels show result of 2012-2015 inversion where slip is allowed at the trench (non-fixed surface). Magnitude of total postseismic slip on the subduction interface is scaled by color, with arrows showing direction of hanging wall motion at each patch. White lines show 50 cm contours of slip. Thick black line with teeth marks the MAT, while thin grey lines show depth in 10 km intervals (Kyriakopoulos et al. 2015). Dashed line shows EPR-CNS transition (Barckhausen et al. 2001). Purple polygon denotes zone of recoverability, outside of which we are unable to resolve structures uniquely. (a) Aftershocks until end of 2012 shown as grey dots, with purple stars representing locations of repeating aftershock clusters (Yao et al. 2017). (b) 2012 coseismic slip contours shown in pink (every 100 cm), with percentage of pre-2012 locking annotated and shown in green (20% intervals, starting at 50%) (Kyriakopoulos and Newman 2016).

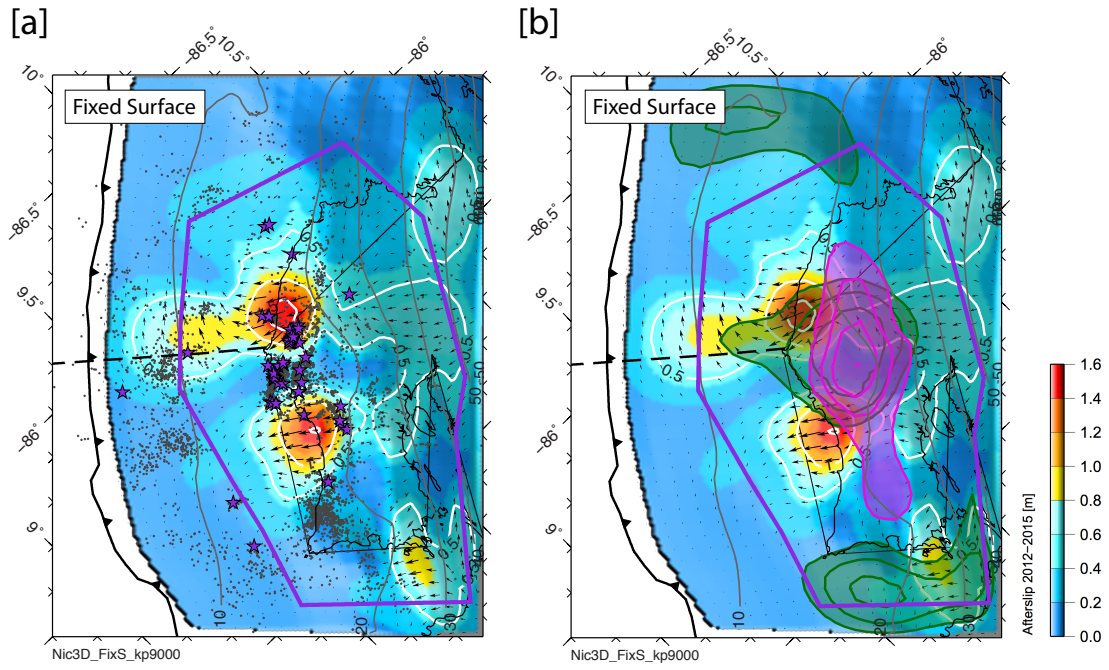

Figure 2.8: Same as for Figure 2.7, except with inversion not allowing slip to rupture the trench (fixed surface). Again, slip on the subduction interface is scaled by color, with arrows showing direction of hanging wall motion at each patch. White lines show 50 cm contours of slip. Purple polygon denotes zone of recoverability, outside of which we are unable to resolve structures uniquely. (a) Aftershocks until end of 2012 shown as grey dots, with purple stars representing locations of repeating aftershock clusters (Yao et al. 2017). (b) 2012 coseismic slip contours shown in pink (every 100 cm), with percentage of pre-2012 locking annotated and shown in green (20% intervals, starting at 50%) (Kyriakopoulos and Newman 2016).

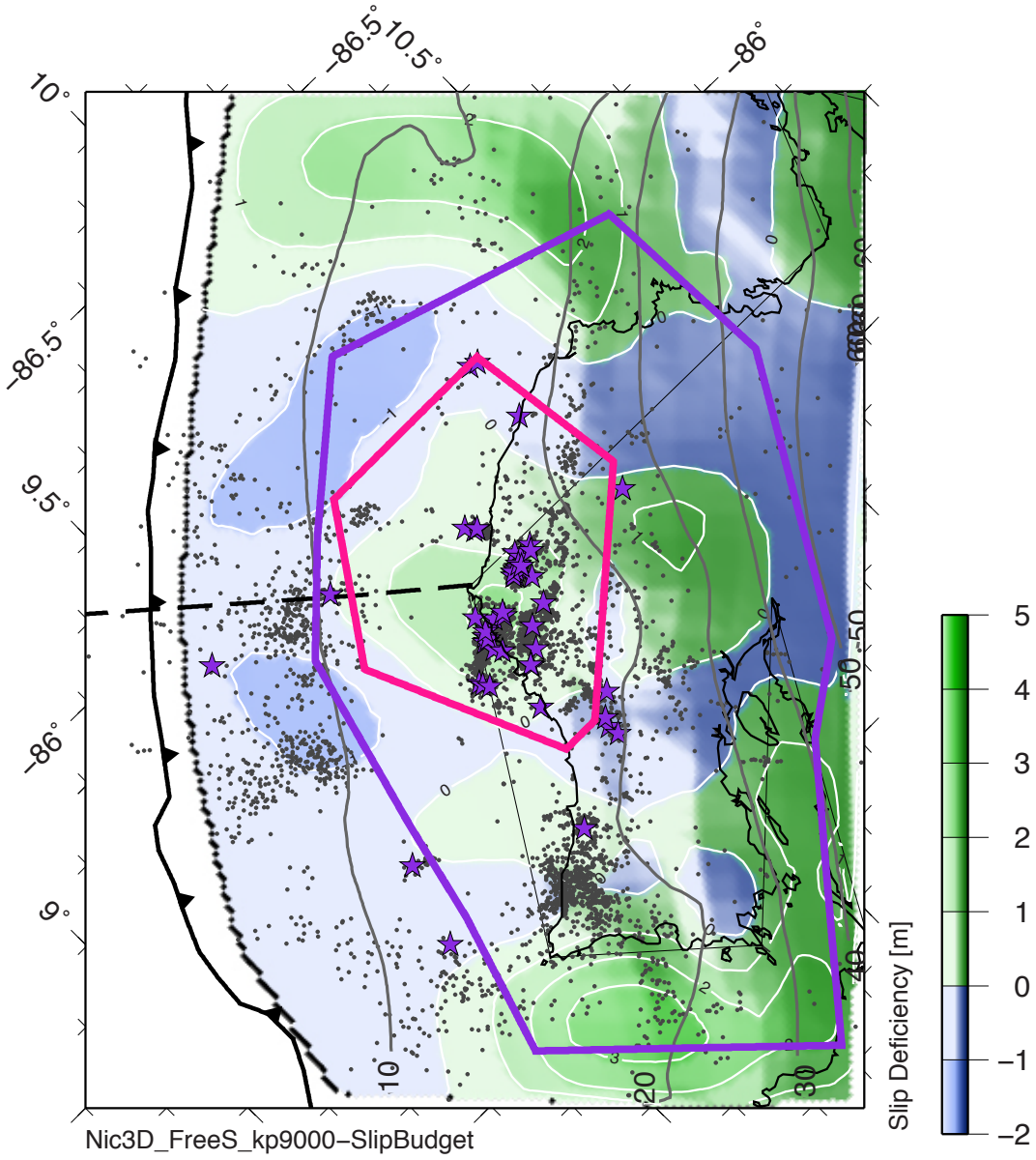

Figure 2.9: Slip deficit as difference between interseismic locking, coseismic slip, and afterslip. Interseismic slip accumulation is calculated as percentage of interseismic locking (Kyriakopoulos and Newman 2016) multiplied by the full tectonic convergence rate over 62 years. Afterslip is from non-fixed surface model. Negative slip deficit represents slip overshoot. Overlain are aftershocks (grey dots) and repeating events (purple stars) from Figures 2.7a and 2.8a (Yao et al. 2017). Pink polygon shows the region of significant stored strain near the elbow in the coastline, as discussed in Section 2.5.4. Purple polygon shows area of recoverability, dashed black line is EPR-CNS transition from (Barckhausen et al. 2001), and thick black line with teeth marks the MAT.

Table 2.1: Displacements and errors from 2012 to 2015 at Campaign and Continuous GPS stations used in this study. Dates in decimal years, displacements relative to stable Caribbean plate.

Station	Longitude	Latitude	Elev. [m]	Start	End	E [mm]	eE [mm]	N [mm]	eN [mm]	U [mm]	eU [mm]
Campaign											
BAGA	-85.261	10.5414	123.49	2012.7022	2015.1945	-53.87	5.06	-51.08	3.91	-37.67	19.07
BALL	-85.448	10.3834	118.03	2012.7077	2015.1836	-67.01	3.54	-71.98	2.85	50.80	12.19
BONG	-85.207	9.7438	21.54	2012.6940	2015.1945	-82.47	2.75	-112.97	2.18	-7.01 9.79	
CEBA	-85.776	10.2491	90.43	2012.6967	2015.1863	-84.13	2.78	-140.81	2.54	1.28	11.16
COBA	-85.107	9.6881	172.44	2012.7240	2015.1890	-55.06	6.08	-52.37	5.08	-15.35	26.49
DIRI	-85.611	10.2718	82.04	2012.6940	2015.1781	-123.10	3.47	-143.86	2.72	35.10	11.81
GRAN	-85.653	10.5622	122.24	2012.7022	2015.1890	-59.94	2.84	-56.37	2.34	14.25	9.72
GUA2	-85.450	10.1401	136.32	2012.6913	2015.1781	-117.24	3.34	-169.28	2.81	-20.76	12.53
GUIO	-85.659	9.9231	31.42	2012.6913	2015.1808	-117.78	2.97	-198.44	2.47	120.61	10.35
HOJA	-85.382	10.0795	240.97	2012.6858	2015.1808	-128.77	3.57	-173.65	3.36	-17.86	14.84
JICA	-85.136	9.9751	61.40	2012.6995	2015.1863	-85.65	3.11	-99.23	2.44	23.58	10.97
LEON	-85.187	9.9365	276.91	2012.6885	2015.1836	-127.69	3.09	-124.48	2.55	20.31	10.78
MATA	-85.813	10.3553	77.82	2012.6967	2015.2000	-77.63	7.96	-91.02	7.73	22.22	40.87
MIRM	-85.571	10.0421	433.75	2012.7158	2015.1890	-98.85	3.10	-160.09	2.55	-84.69	10.54
PALO	-85.220	10.2415	40.05	2012.7022	2015.1836	-55.40	2.92	-79.54	2.33	-25.66	10.77
PAQU	-84.955	9.8322	80.26	2012.7049	2015.1918	-53.02	3.21	-43.76	2.63	45.06	11.02
POTR	-85.569	10.8474	155.76	2012.7131	2015.1945	-25.89	2.98	-33.78	2.43	35.07	12.96
SAMA	-85.549	9.8892	45.91	2012.6913	2015.1781	-118.93	3.66	-161.10	3.00	54.37	13.21
SJOS	-84.948	10.3656	1062.14	2012.6995	2015.2000	-63.25	3.28	-39.97	2.68	-0.01	11.14
SJUA	-85.757	10.0632	44.58	2012.7104	2015.1863	-88.38	3.55	-155.78	2.66	76.04	13.12
TENO	-85.098	10.6018	373.35	2012.7131	2015.2055	-66.88	3.24	-44.32	2.73	25.94	11.75
VENA	-85.792	10.1611	24.98	2012.6940	2015.1863	-88.42	3.28	-147.66	2.55	38.94	11.36
Continuous											
BIJA	-84.577	9.7500	555.54	2012.7240	2015.1945	-10.67	2.68	7.40	2.19	24.37	10.27
BON2	-85.203	9.7645	28.33	2012.7049	2015.1945	-82.46	2.71	-99.36	2.31	24.24	9.95
CABA	-85.344	10.2379	26.78	2012.6803	2015.1945	-100.13	2.21	-125.06	1.81	73.06	7.72
ELVI	-85.446	10.3947	81.76	2012.7131	2015.1945	-75.29	2.09	-67.71	1.73	52.46	7.13
EPZA	-85.568	10.1409	668.60	2012.6803	2015.5671	-154.62	2.37	-205.49	1.79	-22.13	7.90
GRZA	-85.636	9.9155	39.69	2012.6967	2015.1945	-112.42	2.53	-181.98	2.00	111.81	8.79
HATI	-85.710	10.2922	58.69	2012.6803	2015.1945	-119.69	2.95	-171.40	2.27	11.24	9.91
HUA2	-85.352	10.0177	594.20	2012.6831	2015.1945	-150.02	2.53	-181.89	1.99	3.94	8.64
IND1	-85.502	9.8646	75.44	2012.6858	2015.1945	-140.75	2.86	-177.53	2.23	84.93	11.09
LAFE	-84.960	9.8071	65.17	2012.6803	2015.1945	-67.42	2.29	-69.41	1.97	70.43	10.32
LEPA	-85.031	9.9454	20.97	2012.7077	2015.1945	-65.70	2.47	-60.85	2.07	38.80	8.74
LMNL	-85.053	10.2675	102.85	2012.6803	2015.1945	-76.01	2.09	-73.74	1.69	44.52	7.07
PNE2	-85.829	10.1952	19.66	2012.7049	2015.1945	-77.53	3.01	-126.03	2.28	36.17	11.01
PUJE	-85.273	10.1140	29.10	2012.6803	2015.6411	-119.52	2.23	-141.66	1.79	55.46	7.54
PUMO	-84.967	10.0645	17.90	2012.6803	2015.1945	-69.20	2.23	-71.35	1.82	55.56	8.45
QSEC	-85.357	9.8404	17.74	2012.6803	2015.1945	-145.74	2.22	-178.47	1.75	42.87	7.70
SAJU	-85.711	10.0671	73.82	2012.6803	2015.1945	-112.18	2.23	-206.19	1.81	45.58	7.91
VERA	-84.869	10.8536	64.30	2012.6803	2015.1945	-39.70	2.53	-55.49	2.10	20.99	9.49

Table 2.2: Displacements and errors from 2015 to 2016 at Campaign and Continuous GPS stations used in this study. Dates in decimal years, displacements relative to stable Caribbean plate.

Station	Longitude	Latitude	Elev. [m]	Start	End	E [mm]	eE [mm]	N [mm]	eN [mm]	U [mm]	eU [mm]
Campaign											
BAGA	-85.261	10.541	123.49	2015.186	2016.180	-9.02	3.97	0.12	3.16	61.84	16.12
DIRI	-85.611	10.272	82.04	2015.175	2016.175	-13.13	3.61	-2.45	3.09	16.96	14.36
GUA2	-85.450	10.140	136.32	2015.175	2016.169	-20.03	4.58	18.59	4.38	45.92	20.08
GUIO	-85.659	9.923	31.42	2015.178	2016.169	0.35	3.35	8.36	3.16	-7.11	14.72
MIRM	-85.571	10.042	433.75	2015.175	2016.169	-12.63	3.40	10.56	3.06	-1.66	14.01
SJOS	-84.948	10.366	1062.14	2015.197	2016.178	-5.97	4.40	6.10	4.10	48.91	19.89
VENA	-85.792	10.161	24.98	2015.184	2016.175	-7.12	2.60	2.04	1.99	-14.32	9.20
Continuous											
BIJA	-84.577	9.750	555.54	2015.175	2016.178	-0.08	1.81	2.42	1.51	11.76	7.21
BON2	-85.203	9.765	28.33	2015.175	2016.178	-9.85	1.90	2.63	1.65	-4.71	7.29
CABA	-85.344	10.238	26.78	2015.175	2016.178	-6.46	1.76	7.57	1.51	2.09	6.64
ELVI	-85.446	10.395	81.77	2015.175	2016.178	-5.83	1.74	8.75	1.44	-6.44	6.21
EPZA	-85.568	10.141	668.59	2015.559	2016.178	-11.16	1.88	0.44	1.47	-1.22	6.66
GRZA	-85.636	9.916	39.69	2015.175	2016.178	-0.40	1.81	11.06	1.44	-26.81	6.49
HATI	-85.710	10.292	58.68	2015.175	2016.178	-17.17	1.76	-0.74	1.46	-9.20	6.38
HUA2	-85.352	10.018	594.20	2015.175	2016.178	-11.47	1.69	3.25	1.39	1.07	5.92
IND1	-85.502	9.865	75.14	2015.175	2016.178	-8.45	2.22	13.93	1.79	-12.04	8.97
LAFE	-84.960	9.807	65.18	2015.175	2016.178	-5.74	1.86	1.18	1.64	4.30	8.68
LEPA	-85.031	9.945	20.97	2015.175	2016.178	-6.54	1.77	1.59	1.51	10.57	6.51
PNE2	-85.829	10.195	19.66	2015.175	2016.178	-12.39	2.00	-1.17	1.52	-1.73	7.34
PUJE	-85.273	10.114	29.09	2015.175	2016.178	-11.38	2.18	4.41	1.81	2.01	7.75
PUMO	-84.967	10.065	17.91	2015.175	2016.178	-4.40	1.81	4.70	1.51	5.43	7.20
QSEC	-85.357	9.840	17.73	2015.175	2016.178	-8.73	1.77	7.35	1.42	-19.89	6.38
SAJU	-85.711	10.067	73.81	2015.175	2016.178	-3.09	1.80	2.48	1.49	-22.21	6.64
VERA	-84.869	10.854	64.31	2015.175	2016.178	-5.35	2.04	-4.64	1.75	1.29	7.78

CHAPTER 3
ENIGMATIC UPPER-PLATE SLIVER TRANSPORT PAUSED BY MEGATHRUST EARTHQUAKE AND AFTERSLIP

Citation: Hobbs, T.E., Newman, A.V., Protti, M. (2019), *Enigmatic Upper-Plate Sliver Transport Paused by Megathrust Earthquake and Afterslip*. Submitted to Earth and Planetary Science Letters.

3.1 Highlights

- 5 years of postseismic GPS data captures entire megathrust relocking sequence
- Novel trench-parallel sliver transient between afterslip and interseismic period
- Findings suggest slip partitioning may be modulated by megathrust locking

3.2 Abstract

How does deformation after an earthquake affect megathrust stresses? Five years of surface velocities following the 2012 M_w 7.6 Nicoya, Costa Rica earthquake uniquely capture the lithospheric recovery. During the first four years, seaward afterslip transitions to relocked, landward, interseismic motion. This 2016 interseismic period matches the velocity field seen before the 2012 event. Prior to this, in late 2014, locking reinitiated temporarily but was interrupted by a period of never-before-described, exclusively trench-parallel motion associated with a slow slip event and no resolvable megathrust locking. We present a conceptual model in which low postseismic megathrust coupling (little locking) generates partitioned slip: trench-normal motion on the megathrust during afterslip and trench-parallel motion during this never before seen transient. High coupling (strong locking) during the interseismic period drives oblique, convergent surface motions. This challenges

the paradigm that megathrusts are either always partitioned or always oblique, contradicts the tectonic escape hypothesis in Central American, and introduces a new time-dependent megathrust fault behavior. Given that most subduction zones are oblique, explaining these observations is critical to characterizing stress accumulation.

3.3 Introduction

The Nicoya Peninsula in Costa Rica lies on the Middle America Trench, where the Cocos plate subducts beneath the Caribbean (Figure B.1). Uncommonly, the Nicoya peninsula extends to within roughly 60 km of the trench, making it particularly attractive for land-based surface deformation measurements from directly above a subduction seismogenic zone using GNSS receivers. This region also has a rich earthquake history, with M_w greater than 7 events recurring approximately every 50 years (Protti, Güendel, and Malavassi 2001; Feng et al. 2012; Protti et al. 2014). Due to the favorable geometry and short recurrence interval, GNSS and seismic networks have existed on the Nicoya Peninsula for more than two decades, recording myriad tectonic behaviors (e.g. Norabuena et al. 2004; Ghosh et al. 2008; Outerbridge et al. 2010; Feng et al. 2012). On 5 September 2012, the most recent M_w 7.6 earthquake struck beneath Nicoya, producing up to 4 m of slip along the $>$ 100 km rupture length (Protti et al. 2014; Kyriakopoulos and Newman 2016). This distribution of slip from this event had been forecasted prior to rupture using interseismic deformation to determine the megathrust coupling, which turned out to be an accurate method for assessing the region of future coseismic slip (Feng et al. 2012; Protti et al. 2014). Following the earthquake, several studies have detailed the postseismic response of the megathrust over several months to three years (e.g. Chaves et al. 2017; Hobbs et al. 2017; Sun et al. 2017; Voss et al. 2017), illuminating the superposition of slow slip, aftershocks, afterslip, and shallow deformation. Here, we seek to leverage recent observations to present the most complete multiyear description of megathrust relocking, as taken from directly above the seismogenic zone, to characterize the return to interseismic conditions and unique upper-

plate interactions that were observed along the way.

As a result of the 25° obliquity of Cocos-Caribbean convergence at the location of the Nicoya Peninsula, the Central American Forearc translates to the northwest (LaFemina et al. 2009; Kobayashi et al. 2014) at 11 mm/yr (Feng et al. 2012). Inboard of Nicoya, margin-parallel forearc strain is accommodated by shearing across the volcanic arc, along the Haciendas-Chiripa Fault System (Figure 3.1) (Feng et al. 2012; Montero, Lewis, and Araya 2017). While sliver motion is assumed to be controlled by oblique subduction, the extent to which other processes affect its motion throughout phases of the seismic cycle has been undocumented until now. Such work is essential to understanding patterns of stress accumulation and release in the human-populated upper-plate portion of subduction zones.

3.4 Methods

3.4.1 Global Navigation Satellite System (GNSS) Velocities

To understand postseismic crustal deformation, we consider GNSS observations surrounding the Nicoya peninsula. Campaign GNSS measurements were taken in 2012 (Protti et al. 2014), in 2015 and 2016 (Hobbs et al. 2017), and most recently in 2017. Temporally sparse campaign observations supplement a network of continuous GNSS stations on the Nicoya Peninsula, jointly operated by USF and OVSICORI with technical support from UNAVCO. Presented in Table B.1, this study uses 23 stations for 5 years from immediately after the 2012 M_w 7.6 Nicoya earthquake to the end of January 2018. This is an extension of the time series of Hobbs et al. (2017), containing more than 1.5 more years of continuous data and one more set of campaign occupations. For the additional campaign data, we use the same precise point positioning methodology (Hobbs et al. 2017), to obtain fiducial-free daily positions in the ITRF-2008 reference frame. For each day, positions are converted to velocities by finding the slope of the weighted best-fit line through the subsequent year of daily positions, and converted to a stable Caribbean reference frame (Dataset S1 and DeMets, Gordon, and Argus 2010). Using shorter periods ($<$ 1 year) for velocity calcula-

tions, results in aliasing from seasonal and semi-seasonal signals, which are not removed in an effort to preserve the maximum raw tectonic signal. Velocities are decomposed into trench-parallel and trench-normal vectors using a trench orientation of 315° (Figure B.2), consistent with the Nicoya interseismic study (Feng et al. 2012).

These linear velocities tend to under-predict instantaneous velocity in the first ∼3 months after the earthquake, when displacement time series are strongly nonlinear (Figure B.2) (Hobbs et al. 2017). This work, however, is focused on the several-year deformation and its orientation rather than addressing behaviors from immediately after the earthquake (see Malservisi et al. 2015; Hobbs et al. 2017; Sun et al. 2017). For this reason, short-term errors in annual velocities will minimally affect the outcome of our study. We also exclude any velocities with formal horizontal errors greater than 3 mm. This threshold is selected manually to minimize spurious velocities calculated from a small number of data points at the start or end of data intervals (Figure B.3). Formal errors are often smaller than the true uncertainty in GNSS surface velocities, without accounting for factors like scattering from tropospheric moisture. While we attempt to account for much of this by averaging over a year-long period, we also adjust by considering suites of data rather than any one particular time series from an individual station. In this way, our time series remain minimally processed to avoid filtering out region-wide, real tectonic signals that can be convolved with noise signals.

3.4.2 Backslip Inversion for Megathrust Locking

To understand how the subduction interface evolves during postseismic recovery, surface velocities are used as inputs for elastic slip inversions using a fully 3D slab model (Kyriakopoulos et al. 2015). Given the same station-slab geometry, Green's functions from the inversion of Hobbs et al. (2017) are implemented into GTdef (Chen et al. 2009) using the backslip method of Savage (1983). This method is only applicable after the afterslip signal is diminished, hence we calculate backslip for times in the latter portion of our study period

only.

Assuming that a freely-slipping plate moves at the constant convergence rate (82.3 $\pm$ 2.2 mm/yr DeMets, Gordon, and Argus 2010), any degree of coupling can be modeled as relative amounts of normal slip on an otherwise stationary interface. In effect, this assigns a reference frame wherein the entire fault is sliding freely, modeled as being "stationary", and assigns backslip to portions of the fault which are retarded. This methodology therefore assumes only purely elastic, recoverable convergence of plates with no far-field deformation. Whereas trench-parallel motion is often regarded as inelastic (unrecoverable), some trench-parallel motion must be removed prior to inverting for backslip (for further discussion see Norabuena et al. 2004). Consistent with previous studies (e.g. Norabuena et al. 2004; Wang et al. 2007), for each time period we calculate the network averaged trench-parallel velocity and remove it from each station (Table B.2). This allows us to image the spatial progression of the relocking between the Cocos and Caribbean Plates, assuming that the majority of trench-parallel motion is related to unrecoverable sliver motion rather than convergence. To demonstrate, however, that our results are robust to this choice to remove average trench-parallel motion, supplementary Figure B.4 shows the results for the time period of maximum trench-parallel motion (green) calculated by removing the previously documented 11 mm/yr sliver motion (Feng et al. 2012), and when the 2015 SSE signal (Voss et al. 2017) is removed. All results show the same result under the central peninsula and have similar misfits, confirming that, within reasonable limits, the findings here are insensitive to varying the amount of trench-parallel slip removed prior to inversion.

In an underdetermined inversion, damping is applied and a preferred solution is found by minimizing the model fit and solution roughness (Figure B.5). Model predictions for surface velocities are compared against observed velocities to ensure the model produces realistic ground motions (Figure B.6), and from the resolution matrix we determine the area of resolvability (Figure B.7). Though our model cannot resolve locking up to the trench or at the edges of the model space, the match between modeled surface velocities and those

observed suggests the results near the peninsula are reasonable.

3.5 Results

3.5.1 Relocking Period Features Unexpected Trench Parallel Motions

Annual GNSS surface velocities show intriguing features over the five year postseismic period (Movie B.11, Figure 3.1), which can be divided into six representative start dates: dominant afterslip (2013.00 — red), diminished afterslip (2013.95 — orange), initial relocking with minor trench-parallel motion (2014.22 — yellow), maximum trench-parallel motion (2015.30 — green), second relocking (2015.80 —blue), and return to interseismic motions (2016.40 — purple). Note that we chose these stages to best represent the most important features and phases during the 5 year postseismic period, and thus they need not be evenly spaced. We refer to 'afterslip' as the time in which surface velocities are seaward following the earthquake, 'interseismic' as surface velocities that are landward and mimic the previous interseismic period, and 'relocking' as the time between afterslip and interseismic. Surface velocities are also decomposed into azimuth, trench-normal, and trench-parallel time series (Figure B.2). In both Figures 3.1 and B.2 we see a progression from trench-normal afterslip that, between late-2013 (Figure 3.1b) and early-2014 (Figure 3.1c), decays and rotates towards purely trench-parallel motion (Figure 3.1d). This is followed in late-2015 by continued rotation towards oblique landward convergence (Figure 3.1e), with coastal stations then inland stations returning to near-interseismic velocities seen prior to the 2012 earthquake (Figure 3.1f). The relocking period, it seems, is interrupted by a period of purely trench-parallel velocity across the entire forearc sliver. Hereon, this period will be referred to as the Postseismic Sliver Transient (PST).

3.5.2 Relocking in Two Phases

Figure 3.2 shows megathrust locking (coupling) during the latter 4 stages described in Figure 3.1: relocking initiation (yellow), sliver transport (green), second relocking (blue), and

interseismic (purple). Note that we select only time periods for which we expect little or no afterslip (Figure 3.1c-f, showing no seaward motion). Before inverting the velocity field, the average trench-parallel velocity at that time was removed, representing an assumed northwestward rigid block translation (see Section 3.4.2 for discussion). We find that interface locking initiates contemporaneously with decaying afterslip (Figure 3.2a), but then nearly disappears during the maximum PST (Figure 3.2b). Ephemeral relocking, in which locking initiates but then diminishes, has not been documented previously.

The Nicoya Earthquake Patch After the PST, locking again increases and forms a highly locked patch under the center of the peninsula. This patch is collocated with the area of highest locking in the previous interseismic period (Feng et al. 2012; Kyriakopoulos and Newman 2016) and the maximum coseismic slip (Protti et al. 2014; Kyriakopoulos and Newman 2016). It is also an area that was devoid of afterslip and aftershocks (Hobbs et al. 2017). This suggests it may be a permanent velocity-weakening asperity through multiple earthquake cycles: focusing stress accumulation during the interseismic and rupturing energetically during large coseismic events roughly every 50 years (Feng et al. 2012).

3.6 Discussion

3.6.1 Relocking Timeline

Initiation of relocking on the rupture patch 3 years after the mainshock is slower than expected (Remy et al. 2016; Bedford et al. 2016), and the full interseismic velocity field (16.4 ± 4.9 cm/yr at 11.1 ± 16.0^{o}) is only attained by mid-2016. Subtracting 4 years postseismic from the interseismic energy budget accounts for up to 0.33 m of potential slip, based on convergence at 82 mm/yr (DeMets, Gordon, and Argus 2010) and depending on the amount of partial coupling attained during the relocking period. This suggests that accurately constraining recovery timescales is critical to estimating accumulated stress, rather than simply assuming it accumulates over the full inter-event time.

3.6.2 Novel Observation of Variable Trench-parallel Velocity

Afterslip and relocking are expected in the current paradigm of postseismic recovery (Wang, Hu, and He 2012), however the interruption for exclusively trench-parallel motion observed between 2013.95 and 2015.80, was not. Sliver transport rates are generally considered to be constant (e.g. Jarrard 1986; McCaffrey 1992; Lundgren et al. 1999; Bevis and Martel 2001; McCaffrey, Stein, and Freymueller 2002; Iinuma et al. 2004; Norabuena et al. 2004; LaFemina et al. 2009; Feng et al. 2012), but we observe substantial variability across the PST (Figure B.2). Averaged across the forearc and over the entire PST, surface velocity is 9.2 ± 4.5 mm/yr and -0.1 $\pm$ 7.2 mm/yr in the trench-parallel and trench-normal directions, respectively. The average azimuth of velocities during the PST is 317 ± 39^{o}, indistinguishable from the trench azimuth of 315^{o} (Figure B.2). In other words, we know that there is an unexpected period in which the motion of the sliver is purely trench-parallel. This trench-parallel velocity is similar or slightly larger than the 11 mm/yr interseismic value (Feng et al. 2012), and 1.7-2.7 times larger than earlier sliver transport estimates for this region (McCaffrey, Stein, and Freymueller 2002; Norabuena et al. 2004; LaFemina et al. 2009). During the maximum PST (2015.30), trench-parallel velocity is 13.3 ± 5.7 mm/yr. Conversely, it reaches its minimum in the early portion of the postseismic recovery period, where appreciable trench parallel motion is absent. During this time, we even find slightly negative trench-parallel velocities, with the largest signals occurring at coastal and Mid-Peninsula sites (Figure B.2). This raises the question: What is causing this variable sliver velocity? To answer this, we consider conditions in and around the Nicoya megathrust and the portion of the Central American Forearc Sliver that overlies it.

Relationship to Megathrust Slow Slip Events

Two SSEs occurred during the postseismic period, with one in early 2014 lasting from early February to mid-March (2014.09-2014.20), and a longer event from late 2015 to early 2016 (2015.75-2016.25) (Voss et al. 2017). The 2014 SSE is coincident with the onset of

the PST and the first peak in trench-parallel motion, while the longer 2015 SSE initiates at the termination of the PST event (Figure B.2). Removing the 2015 SSE velocities prior to inversion (Figure B.4) does not significantly affect results. Bounded temporally by SSEs, a relationship between the sliver transient and other transient fault behavior of the megathrust below is possible. Although we cannot say for certain which came first, initiation of a SSE may be the source of the apparent disruption of the initial locking phase, or vice versa. Further studies should focus on modelling to better determine the possible link between SSE, megathrust relocking, and trench-parallel movement.

Relationship to Seismic and Volcanological Data

Because our and prior observations suggest differential motion of the stable Caribbean plate relative to the Central American Forearc is accommodated through the volcanic arc (Lundgren et al. 1999; Norabuena et al. 2004; Feng et al. 2012; Montero, Lewis, and Araya 2017), we explored changes in regional (`http://www.ovsicori.una.ac.cr`) and arc-related seismicity (Chaves et al. 2017; Montero, Lewis, and Araya 2017), as well as in eruptive activity (`http://volcano.si.edu`) concurrent with the PST (Figures B.8, B.9, B.10). Given current datasets, there is no discernable deviation between the pre-PST, PST, and post-PST periods. However, a regional network on the Turrialba-Irazú complex did record an earthquake swarm immediately following the Nicoya earthquake (Lupi, Fuchs, and Pacheco 2014), as did Rincón, Miravalles, Tenorio, and Arenal volcanoes (Taylor and Bakkar 2016), suggesting a dynamic triggering link between the megathrust and arc-related faults. If we expect that earthquakes in this environment may be very small, then event detection using local networks may be necessary to safely exclude the possibility of heightened arc fault-related seismicity during the PST.

Preliminary Conceptual Model of PST

To understand how these observations may be relevant to other subduction zones it is important to ask: What is driving the postseismic sliver transient? Oblique convergence is shown to result in oblique surface velocities in the upper-plate when overall coupling on the megathrust interface is relatively strong, and partitioned slip when coupling is relatively weak (McCaffrey 1992; Bevis and Martel 2001; McCaffrey, Stein, and Freymueller 2002). Thus, different subduction zones have different behavior. However, our observations suggest this is not the full story.

For the interseismic periods (before 2012 and after 2016), surface velocities are oblique landward and the megathrust is well-coupled (Feng et al. 2012). The presence of afterslip proves that coupling was low on the megathrust, because differential motion was occurring on it (Hobbs et al. 2017), and also suggests that coupling on the Haciendas-Chiripas arc fault system is likely to have weakened due to relative elastic extension in the upper-plate, called 'tectonic pull' (Protti, Güendel, and Malavassi 2001; Lupi, Fuchs, and Pacheco 2014). In an oblique convergent margin we expect this to drive dextral slip across the arc fault, consistent with observed short-lived, trench-parallel forearc motion we see during the PST. Concurrently, we have shown herein that megathrust coupling at that time was very low. Therefore, during afterslip and the PST, when we see partitioning of surface velocities between trench-normal and trench-parallel, respectively, the megathrust fault coupling is low. We propose that partitioning or oblique motion is indeed controlled by megathrust conditions, but that variations in interface strength can drive differing behavior at a single subduction zone. This is suggested by the association between megathrust variability through the postseismic period (Figure 3.3) that corresponds to sliver motion when coupling is weak, and oblique surface motions when coupling is strong.

Interseismic velocities were assumed to be constant, until months-long, episodic slow slip events SSE were first observed in Cascadia (Dragert, Wang, and James 2001). We now well understand that deformation rates change within the seemingly stable megathrust

interseismic period (Meltzner et al. 2015). The results presented herein tell a similar story, for trench-parallel velocities of the sliver. Could it be that the variable sliver velocity we observe here is not a one-off, but rather is the first observation of a phenomenon occurring at other subduction zones as well? To validate or refine this preliminary conceptual model, we must start looking for temporary instances of partitioned slip, particularly transient sliver motions, that can be then be tied to changes in megathrust conditions.

3.6.3 Tectonic Drivers

Slivers, which are well-developed on at least half of all subduction zones, migrate along the plate margin causing potentially thousands of kilometers of translation over tens of millions of years (Jarrard 1986). According to previous studies, the motion of a forearc sliver occurs either through oblique subduction, on strong megathrusts, or through partitioning of slip into trench-normal megathrust events and trench-parallel motions across transverse arc faults, when the megathrust is relatively weak (Bevis and Martel 2001). The northwest motion of the Nicoya sliver, however, has alternatively been interpreted as the result of subduction of the Cocos Ridge, which drives the Caribbean plate outward (LaFemina et al. 2009; Kobayashi et al. 2014). This model of forearc translation, invoking 'tectonic escape' from the indenting Cocos Ridge and associated high topography inboard within the Panama Microplate (LaFemina et al. 2009; Kobayashi et al. 2014), would result in constant forcing from the southeast at all times in Nicoya's seismic cycle. However, the time-variable nature of sliver transport during the 5-year postseismic period, which varies from null to $>$10 mm/yr (Figure B.2), can likely not be described exclusively by a model invoking a constant lateral forcing such as from an indenting ridge. This finding therefore suggests that the tectonic escape model may not be sufficient for modeling of Central American tectonics, although future work should investigate the state of non-megathrust faults that may be controlling sliver motion. In particular, one should look for data regarding the faults along the Central Costa Rica Deformed Belt, which may inhibit transfer of stress between

the Panama Microblock and Nicoya Forearc Sliver, and along the arc-related Hacienda-Chiripas fault system, which may help accommodate sliver motion. Additionally, it will be important to examine the effect of PST on the northwestern, leading edge of the forearc sliver in order to fully understand the forces driving this behavior.

3.7 Conclusions

Examining 5 years of postseismic surface deformation directly over the source region of the September 2012 M_w 7.6 Nicoya earthquake has uniquely provided an opportunity to image the evolution of megathrust relocking as it enters into the early interseismic portion of the seismic cycle. We identify that trench-normal afterslip clearly decays within two years (by late-2014), and an initial relocking signal is interrupted synchronously with a slow slip event on the megathrust. Within a few months, a novel period of purely trench-parallel motion is observed across the entire forearc region, and can be modeled to show that the feature occurs when little trench-normal coupling is occurring on the megathrust interface. Almost 4 years following the earthquake (by mid-2016), interseismic velocities return to oblique pre-2012 levels across the Peninsula, accompanied by substantial locking again below the central portion of the megathrust.

The relationship between slip partitioning and megathrust coupling is unlikely coincidental, with strongly partitioned motion during periods of low megathrust coupling and oblique motion when locking is high. These findings cannot be sufficiently described using only the tectonic escape model of Central American tectonics, as we have documented sliver transport that does not occur at a constant rate. Although we present a preliminary conceptual framework to explain these observations, future work should seek a cause for the interruption of relocking processes associated with the decrease in coupling and start of the postseismic sliver transient. Attention should also be paid to the sliver-bounding faults to the northwest, along the arc, and to the southeast. Explaining these observations will be crucial in developing a complete understanding of the megathrust earthquake cycle and

associated time-dependent hazards.

3.8 Acknowledgements

All GNSS data is available through UNAVCO archives (http://unavco.org). Seismological data extracted from OVSICORI (http://www.ovsicori.una.ac.cr/index.php/sismologia/encuesta-sismos-sentidos), and volcanological data from Global Volcanism Program (http://volcano.si.edu/search_volcano.cfm). This project is funded through NSERC PGSD2-488063-2016 to T.E.H. and NSF 1447104, 1262267 to A.V.N. Figures prepared using Generic Mapping Tools (GMT), Matlab, and Gnuplot. Field work would not have been possible without support from UNAVCO and OVSICORI, and the assistance of J. Buffo, B. Burgoa, K. Gardner, M.S. Kemmerlin, J. Méndez, J. McAdams, C. Muller, D. Sánchez, and A. Williamson.

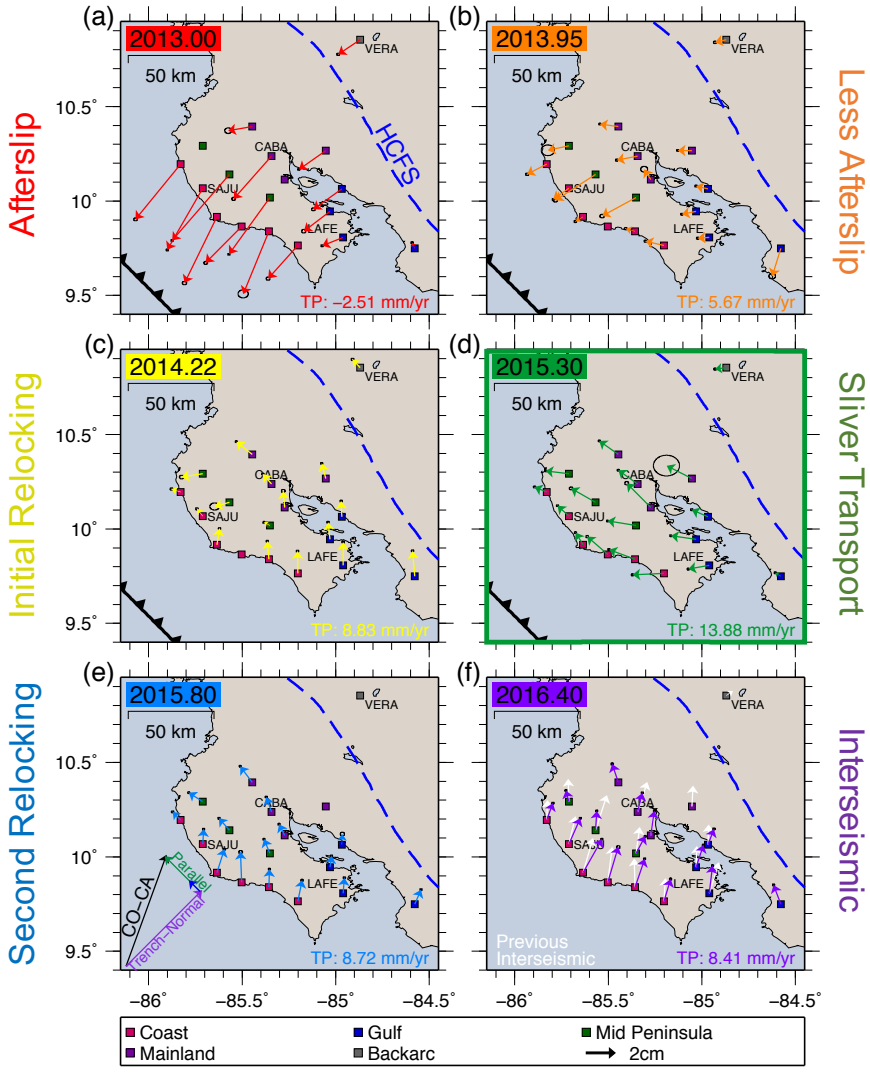

Figure 3.1: Surface velocities, in stable Caribbean reference frame, are calculated for a one year period following the time shown at the top left of each panel. Network averaged trench-parallel (TP) motion indicated in bottom right corner of each panel, but not removed from GNSS velocities. Haciendas-Chiripa Fault System (HCFS) shown as dashed blue line (Kyriakopoulos and Newman 2016; Montero, Lewis, and Araya 2017), and Middle America Trench as black line with triangles. All available times are shown in Movie B.11. Time periods are colored as follows: (a - red) strong seaward motion in January 2013, (b - orange) diminished seaward motion in December 2013, (c) slight trench-parallel motion in March 2014, (d) peak trench-parallel motion in April 2015, (e) diminished trench-parallel motion in October 2015, and (f) oblique landward motion in May 2016. Interseismic results of Feng et al. (2012) shown with white arrows on panel (f). Convergence vector and its trench-normal, trench-parallel, and sliver motion components indicated in black, purple, green, and blue arrows, respectively (DeMets, Gordon, and Argus 2010; Feng et al. 2012) and displayed in panel (e). Coastal stations are shown in pink, mid-peninsula stations in teal, mainland stations in purple, Gulf of Nicoya stations in blue, and backarc station in grey (Table B.1).

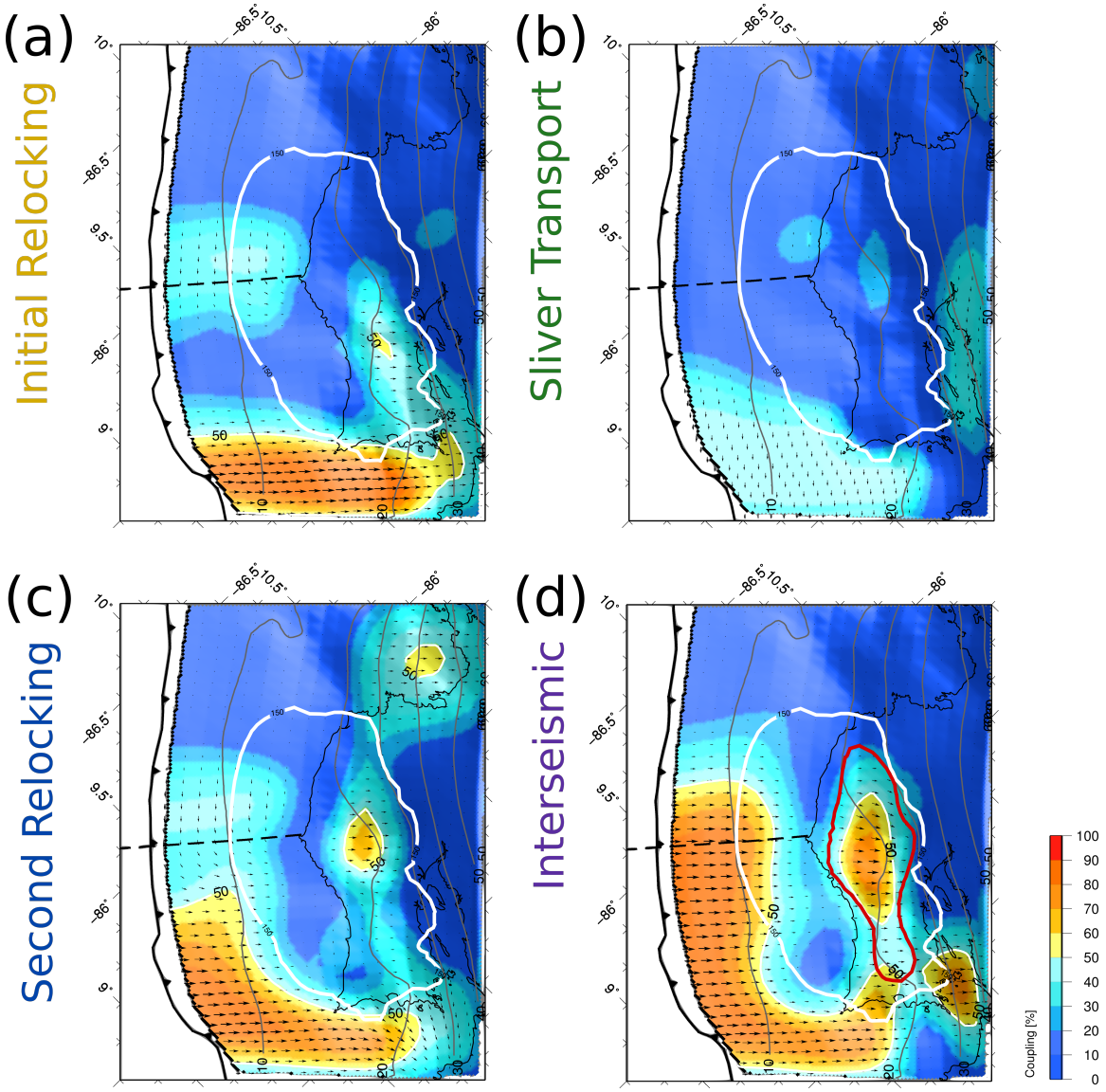

Figure 3.2: Result of backslip inversions during (a) PST initiation, (b) maximum PST, (c) post PST, and (d) the end of the study period, including red contour showing the area of greater than 1 m coseismic slip (Kyriakopoulos and Newman 2016). Proportion of maximum total coupling is colored and contoured, relative to 83 mm/yr convergence (DeMets, Gordon, and Argus 2010), with vectors indicating the direction of hanging wall motion. Average trench-parallel velocities for each time period are removed prior to inversions, as discussed in method, but locking is allowed in either trench-parallel direction and normal faulting (backslip). Interface geometry shown by grey contours (Kyriakopoulos et al. 2015). Middle America Trench shown as solid line with triangles, and area of recoverability indicated by the thick white line (Figure B.6). Model misfit evaluations and comparison of observed to predicted surface velocities can be found in Figures B.4 and B.5, respectively.

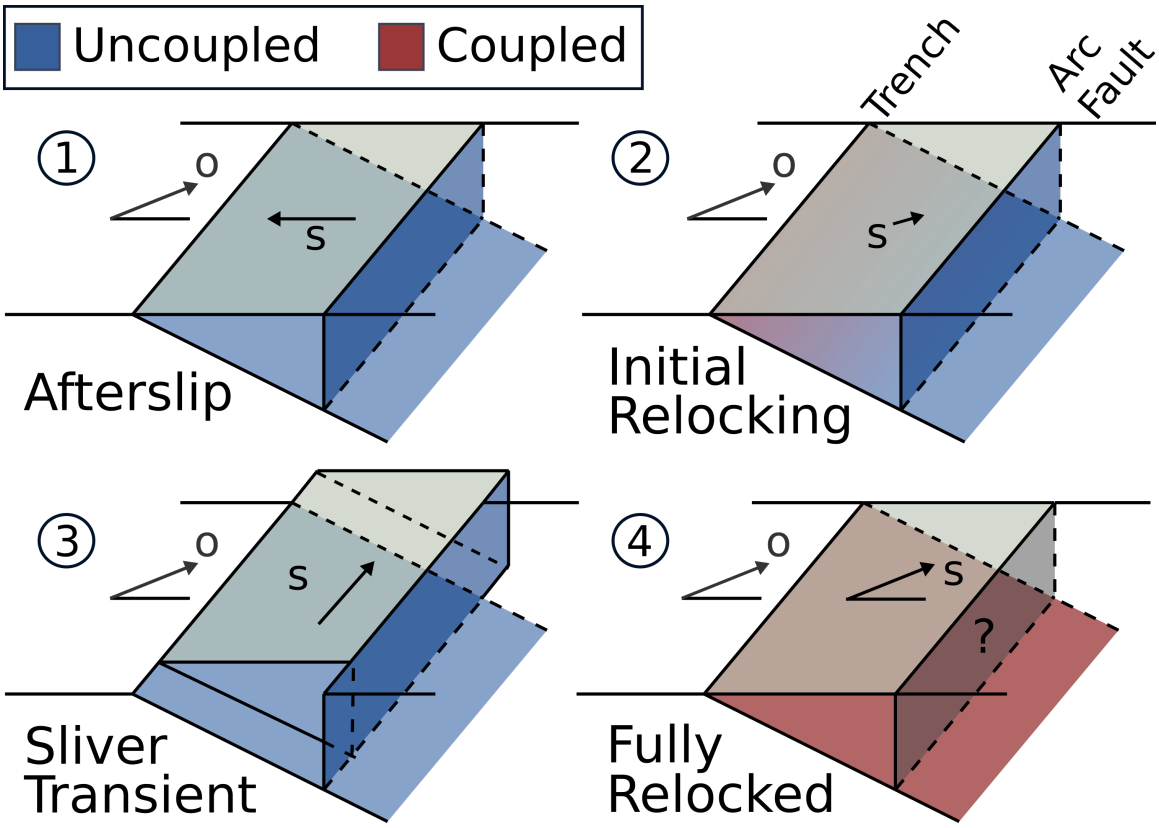

Figure 3.3: Conceptual model of forearc motions observed herein, delineated along the megathrust interface (inclined plane) and arc-bounding fault (vertical). This model is generalized beyond the study area, but surface velocities are consistent with those observed in Figure 3.1 and B.7. The incoming oceanic plate, marked by vector "o", maintains oblique convergence. Representative surface velocities shown as vector "s". Blue faults are poorly coupled or unclamped, and red indicates that the fault is relatively well-coupled or strong. During (1) afterslip, the forearc moves seaward in a trench-normal direction, sliding along a weakly-coupled megathrust and unclamping the arc fault. The afterslip is driven by stored elastic stress and coseismic stress changes. As (2) relocking initiates, coupling increases in the shallow megathrust and seaward velocities are diminished or gently reversed. (3) During the PST, coupling is low on the megathrust and arc fault but stored compressional stresses were already released by afterslip. Partitioning of slip during the PST thus results in purely trench-parallel sliver motion. (4) Relocking reinitiates, and eventually the megathrust is highly coupled. Slip is no longer partitioned, and stress accumulates in the direction of convergence, regardless of the state of the arc-bounding fault.

CHAPTER 4

DEFINING THE TEMPORAL RELATIONSHIP BETWEEN AFTERSLIP AND AFTERSHOCKS USING DENSE SEISMIC AND GEODETIC NETWORKS IN NICOYA, COSTA RICA

Tentative Citation: Hobbs, T.E., Yao, D., Newman, A.V., Peng, Z., Protti, M. (2019), *Defining the Temporal Relationship Between Afterslip and Aftershocks Using Dense Seismic and Geodetic Networks in Nicoya, Costa Rica*. To be submitted to Journal of Geophysical Research: Solid Earth.

4.1 Abstract

The majority of the seismogenic portion of a megathrust is located underwater, which makes instrumentation expensive and logistically challenging. The Nicoya Peninsula in Costa Rica is ideally situated for studying the subduction interface as it extends to within 60 km of the trench, allowing for collection of both seismic and geodetic data directly above the rupture zone. This study utilizes the rare subduction geometry to illuminate, for the first time, the relationship between geodetically imaged afterslip and repeating aftershocks following the 2012 M_w 7.6 Nicoya, Costa Rica earthquake.

Analyst-picked aftershocks from the several months following the earthquake are used as templates in a WMF technique, or simply template matching. Detections with very high cross correlation are termed repeating aftershocks. These are thought to result from patches of slip-weakening material (asperities) within an otherwise stably-sliding region. Therefore, repeating aftershocks have been treated as a proxy for slip on the subduction interface. However, repeating seismicity results from the first 3.5 months following the 2012 Nicoya earthquake appear to be spatially anticorrelated with the cumulative distribution of afterslip inverted directly from GPS. Such spatial anticorrelation indicates that slip inferred

from repeating aftershocks may not be a suitable tool for measuring slip in regions without offshore geodetic measurements. This work expands the catalog of detected aftershocks by including detections with lower cross correlation coefficients, allowing us to examine detailed spatial and temporal evolution of aftershock seismicity out to 1.3 years following the earthquake. By expanding the template matching search through another full year (2013), and developing a new methodology for jointly analyzing campaign and continuous GPS data, we are able to further constrain the temporal evolution of repeaters with respect to afterslip. We confirm the previous finding that aftershocks and afterslip are anticorrelated in the updip region, even with good recoverability of geodetic slip and a very complete aftershock catalog. Caution should therefore be exercised in directly using repeating earthquakes as a slip proxy in environments without additional constraints on slip.

4.2 Introduction

Subduction zones are difficult to study given that most of the processes of interest occur at depth (e.g. Bilek and Lay 2018). As well, they are enigmatic because the seismogenic portion of a megathrust is often tens or hundreds of kilometers offshore (Williamson and Newman 2018). Therefore scientists often seek techniques to study megathrust behavior from afar, when nearby measurements of the earth deformation are not available. To characterize the megathrust, one might consider the distribution of seismicity, including b-value mapping(e.g. Schorlemmer, Wiemer, and Wyss 2005; Nuannin, Kulhanek, and Persson 2005; Ghosh et al. 2008; Tormann et al. 2015), or Coulomb stress analysis (e.g. King, Stein, and Lin 1994; Toda and Stein 2000; Toda, Lin, and Stein 2011; Ishibe et al. 2017). Both of these have been used to predict, for example, where different megathrust behaviors are expected to nucleate in future. Having direct geodetic and seismic observations to confirm these predictions (e.g. Kaneko, Avouac, and Lapusta 2010; Cao and Gao 2002), when possible, is critical for confirming our fundamental understanding of how these processes interact.

For the Nicoya Peninsula in Costa Rica, fortunately, we have a unique opportunity to make land-based observations from directly above the seismogenic portion of the megathrust. This has led to a wealth of discoveries in the wake of the 2012 M_w 7.6 Nicoya event, which illuminated how a subduction zone experiences and subsequently recovers from a large earthquake (e.g. Protti et al. 2014; Malservisi et al. 2015; Hobbs et al. 2017; Sun et al. 2017; Voss et al. 2017; Yao et al. 2017; Voss et al. 2018). One particularly interesting finding was the apparent anticorrelation of afterslip and repeating aftershocks reported by Yao et al. (2017) and Hobbs et al. (2017).

Repeating earthquakes are events with nearly identical waveforms that are thought to result from repeated slip on the same patch, such that the source and path remain identical (Nadeau and McEvilly 1999). It was previously established (e.g. Beeler, Lockner, and Hickman 2001; Igarashi, Matsuzawa, and Hasegawa 2003; Matsuzawa et al. 2004; Uchida and Matsuzawa 2013; Hu et al. 2016) that these patches are likely small regions of slip-weakening material within an otherwise slip-strengthening environment: small earthquakes from a piece of the fault that is otherwise sliding stably. As such, they must keep pace with the surrounding fault. Using magnitude-slip relations, the amount of slip on these asperities can be used as a proxy for the amount of slip occurring nearby, resulting in a spatially variable afterslip map without geodetic data. This methodology has been broadly applied in subduction zones such as New Zealand (Todd 2017; Shaddox et al. 2017) and Japan (e.g. Igarashi, Matsuzawa, and Hasegawa 2003; Uchida and Matsuzawa 2013; Hu et al. 2016). All of this despite the fact that the methodology has never been directly compared with well-resolved geodetically determined slip in a megathrust environment.

For Nicoya, one would have expected to see repeating aftershocks distributed throughout the region of geodetically determined afterslip. This ensures that repeating aftershocks are a ubiquitous feature of afterslip, such that they may be used as an acceptable tool for measuring slip. Surprisingly, repeating aftershocks observed in the first 4 months after the mainshock were clustered tightly in a region between two patches of strong afterslip (Yao

et al. 2017; Hobbs et al. 2017). This finding fundamentally challenges the current use of repeating aftershocks as a proxy for slip occurring within an otherwise stably sliding region. Notably, however, the afterslip reported therein was either determined using only continuous GPS data (Yao et al. 2017) or by considering cumulative afterslip over a 2.5 year period between the first and second campaign occupation after the mainshock. In other words, conclusions were based on GPS data with limited temporal or spatial resolution, and using only a subset of the aftershocks sequence.

Seismic and geodetic datasets differ strongly in their temporal and spatial sampling. Seismic data are collected at the sub-second level and their sources can be located with precision on the kilometer scale even in the offshore (e.g. Cleveland, VanDeMark, and Ammon 2015). Static geodetic data are typically reported as daily solutions, with sensitivity that depends on the network-source geometry and the size of the patches experiencing slip in inversion (e.g. Kyriakopoulos and Newman 2016). For the Nicoya Peninsula, checkerboard testing shows good recoverability of the 20 x 40 km^2 slip patches within roughly 30 km of the coastline when using the full network of campaign and continuous stations (Hobbs et al. 2017). Even this presents problems, though, as campaign data are irregularly collected. This is a common issue in geodetic processing: working with heterogeneous datasets (e.g. Biggs et al. 2010). To completely rule out the possibility that repeating aftershocks are occurring synchronously and colocated with afterslip, we must consider how both of these phenomena evolve in time and space over the same interval. To do so requires a technique to incorporate the full suite of available GPS data as well as an earthquake catalog that extends through more of the afterslip occurrence.

We design a new methodology for extracting time series from a network with inconsistencies in spatial and temporal sampling. The resulting timeseries incorporate as much data as possible, with assumptions based on physically realistic models of earth deformation. This methodology means a consistent psuedo-sampling, allowing for study of the evolution of slip at depth in Nicoya, Costa Rica. This methodology could be easily implemented

at other subduction zones where a backbone continuous GPS network exists and campaign data are currently being underutilized. Combining this proximal geodetic deformation data with a newly generated, dense aftershock catalog allows for the first time ever direct comparison of slip and its proxy, repeating aftershocks. Such analysis is critical for validating the current methods of measuring offshore slip as well as for improving our understanding of the megathrust environment as it continues releasing stress postseismically.

4.3 Methods

4.3.1 Geodesy: GPS Timeseries Analysis and Slip Inversion

Campaign occupations and a continuously operating GPS network in Nicoya, Costa Rica provide an unparalleled dataset of postseismic recovery taken from directly above the seismogenic zone. However, gaps in continuous data and sparse campaign sampling result in inconsistent GPS network coverage. Mainly, there is a trade-off between dense spatial coverage, which exists for a very small window of time, and dense temporal coverage, which is available only at a few stations. Herein, we develop a fitting algorithm to artificially generate consistent network coverage over a time period of interest. This algorithm involves creating a **(1)** functional form of dense GPS timeseries such that they can be sampled at any point in time. Displacements calculated from those timeseries are used as input for **(2)** a simple 2D elastic interpolation, to generate psuedodata timeseries at sites with low temporal resolution. Those psuedo timeseries are corrected using the observed data at those stations, to produce a timeseries which is similar in shape to nearby stations but is consistent with all available data. The full suite of real and interpolated data is then inverted to determine time-evolving afterslip on the megathrust.

Data Collection & Initial Processing

Geodetic field work was undertaken on the Nicoya Peninsula in March of three consecutive years: 2015-2017. The first two of these field expeditions are detailed in (Hobbs et

al. 2017), with the third being a repeat of the first: A total of 24 sites were successfully reoccupied for at least two UTC days, 17 of which had measurements in 2012 after the mainshock. All data is archived through UNAVCO at `https://www.unavco.org/data/data.html`. Data from a complimentary, continuously-operating geodetic network on the Nicoya Peninsula, operated by USF and OVSICORI, is accessed through the UNAVCO archives as well. Processing with JPL's "GIPSY-OASIS" software results in fiducial-free daily solutions for campaign sites and continuous stations (consult Hobbs et al. 2017 for detailed discussion).

Functional Form of GPS Timeseries

We define 'continuous' stations as those stations with more than 365 data points (over a 4.5 year period). Their displacements are modeled as the sum of mainshock and aftershock offsets, linear interseismic motion, three superimposed relaxation functions, and rate changes from two SSEs in 2014 and 2015:

$$d(t) = d_M + mt + \{t > t_A \rightarrow d_A\} + \sum_{j=1}^{2} \left[\{t \subset t_{SSEj} \rightarrow m_{SSEj}(t - t_{SSEj})\} + \{t > t_{SSEj} \rightarrow d_{SSEj}\}\right] + \sum_{i=1}^{3} \left[b_i \exp\left(\frac{t_M - t}{\tau_i}\right)\right]$$

where conditional statements are shown in curly brackets ("if p is true then q" is written as $\{p \rightarrow q\}$). Total displacement d is represented through t time, ($d(t)$), and as static offsets from the mainshock (d_M at time t_M) and largest aftershock (d_A at time t_A). Timing of the mainshock and largest aftershock are provided by the USGS Comprehensive Catalog (`https://earthquake.usgs.gov/earthquakes/search/`). Amplitude of aftershock offset is taken as the difference between averaged position on the day before and the day after. Linear interseismic motion is described by slope m. Displacement from SSE event j, occurring over time period t_{SSEj}, is composed of a linear offset during the event (m_{SSEj}) and a cumulative static offset being preserved after the event ends (d_{SSEj}). Timing

and offsets of SSEs were picked by visual inspection of time series. Exponential relaxation functions have linear amplitude (b_i) and nonlinear relaxation constant (τ_i).

Fitting is performed using Gnuplot's 'fit' function (`http://gnuplot.sourceforge.net/`), which uses a Marquardt-Levenberg algorithm (after Marquardt 1963) to iteratively minimize the weighted sum of squared residuals for each component. Due to the large number of variables and the well-known challenges of nonlinear inversion (e.g. Tarantola 1986), we alternately fit the linear (b_i, d_M, m) and nonlinear (τ_i) parameters of the function over partial and full time windows:

1. Fit linear constants over full time
2. Fit intermediate exponential over full time
3. Fit longest exponential over 2013-2016
4. Fit shortest exponential over 2012.5-2013.2
5. Re-fit linear constants over full time
6. Fit all exponentials over full time

For each subsequent step the outputs from the previous step are used as initial values, to avoid inadequate fitting due to local minima. We use varied time periods to help fit relaxation functions over short, medium, and long time intervals — corresponding to fastest, moderate, and slowest relaxation. The resulting goodness of fit is the average reduced chi squared (χ^2) value, evaluated for each component (Table 4.1). Single and double relaxation functions were also modeled, but three exponential terms was found to provide superior fit and therefore a lower χ^2.

Interpolation at Campaign Sites & Correction

Once a functional form of each timeseries exists, they are sampled every month after the earthquake for 4.5 years to fully characterize the time-evolving postseismic deformation.

The resulting cumulative displacements at each station are used to calculate the predicted displacements at campaign stations for the same times. For this, we use the 2D elastic interpolation program, GPSGRIDDER (Sandwell and Wessel 2016), as implemented in Generic Mapping Tools (Wessel et al. 2013).

To extract the most information, however, we would like to incorporate campaign data whenever it is available. To do this, we take predicted displacements at campaign stations and apply a linear scaling (c) and vertical offset (k) so it better matches with observed campaign data:

$$d_{corrected}(t) = cd + k$$

The optimal scaling and offset are determined by grid search that minimizes squared misfit between weighted observations and predictions. Weights are the inverse of observations per year, such that if there are many observations near the time under consideration then each point is weighted less than if there are few. The results are timeseries of predicted displacements that have similar shape to nearby continuous stations, but match observed campaign displacements where available.

GTdef inversion

Cumulative displacements at all stations, evaluated every month, are used as inputs into elastic inversion code: GTdef (Chen et al. 2009). We use the 3D fault geometry of Kyriakopoulos et al. (2015), preserving the station-node geometry and thus allowing us to use the FEM generated Green's functions of Hobbs et al. (2017). Smoothing is applied in two dimensions, and evaluated against misfit to find the solution which simultaneously minimizes both values (Figure 2.5). When interpreting results, we consider only the region of good recoverability (Figure 2.4), defined in Hobbs et al. (2017) using a checkerboard test and resolution matrix. The advantage of this methodology is that the network remains constant in all time periods, so we can consider the same region of 'good' recoverability at all points in time.

4.3.2 Seismology: Aftershock Detection

To better understand the aftershocks, and particularly the repeating aftershocks, of the 2012 M_w Nicoya earthquake sequence, we extend the catalog of Yao et al. (2017) through the year 2013. To do this, we use a WMF event detection technique (Meng et al. 2012; Meng, Peng, and Hardebeck 2013; Yao et al. 2017), which cross correlates template earthquake waveforms with continuous waveforms to look for similarities.

Data Collection & Preprocessing

We utilize continuous waveforms from the seismic network operating on the Nicoya Peninsula, Costa Rica. As shown in Figure 1.7, these 14 stations are jointly maintained by OVSICORI, UCSC, USF and GT, and described in Dixon et al. (2013) and Yao et al. (2017). Though there are minor data gaps (Figure 4.1), data is available from several stations at all times. Templates events are those used in Yao et al. (2017), as we endeavor to extend that same catalog. These template events were picked by an automated short-term average / long-term average (STA/LTA) detection algorithm, and subsequently confirmed by analysts (Walter et al. 2015). In total, there are 7890 templates which are pre-selected for high signal to noise ratio (SNR > 5). The templates and continuous timeseries, recorded at 40-100 Hz sampling frequency, are bandpass filtered from 2-15 Hz to isolate local seismic signals and then interpolated to a common 40 Hz sampling frequency.

Waveform Matched Filter

The procedure utilized is fully explained in Meng et al. (2012) and Yao et al. (2017), but briefly described here as well. Template events are windowed from 1 second before to 5 seconds after P and S wave arrivals in the vertical and horizontal components, respectively, and those windows are cross correlated against appropriate channels of daily continuous waveforms. We then shift each cross correlation function to the origin times of the templates, to align detections across components and stations. When waveforms are similar,

the cross correlation coefficient will be high. Thus, we consider a detection as any point at which the stacked cross correlation coefficient exceeds 12 times the Median Absolute Deviation (MAD) of the daily mean cross correlation functions (e.g. Yao et al. 2017). The cross correlation of template waveforms and continuous waveforms is carried out using the Extreme Science and Engineering Discovery Environment (XSEDE) facilities through the Texas Advanced Computing Center (TACC) Stampede Cluster (Towns et al. 2014). The parallelized code was developed for GPU by Meng et al. (2012).

Catalog Building

After combining detections, we eliminate duplicates within a 3 second period to preserve only the detection with the highest cross correlation value. Newly detected events are assigned the location of the template event that detected them and a Local Magnitude (M_L) based on the ratio of the detected average peak amplitude relative to that of the template (Peng and Zhao 2009). We compute the Gutenberg-Richter statistics (Gutenberg and Richter 1944) for our catalog of detected events using the maximum curvature method (e.g. Wiemer, McNutt, and Wyss 1998) for Magnitude of Completeness (M_C). We use linear least squares fitting for:

$$\log N = a - bM$$

where N is the cumulative number of events equal to or greater than a given magnitude, M, with coefficients for activity, a, and abundance of events with small versus large magnitude, b or b-value.

Repeating events are identified as those with cross correlation coefficient greater than 0.9, and then grouped into families using the Equivalency Class algorithm of Press et al. (1986) and Peng and Ben-Zion (2005). Slip from each event, d in [m], is calculated assuming constant strain drop ($\Delta\epsilon$) of 10^{-4} (Kasahara 1981), a circular crack model (Kanamori and Anderson 1975; Ben-Zion et al. 2003), and an empirical potency-magnitude relationship (Ben-Zion and Zhu 2002):

$$r^3 = \frac{7}{16}\frac{P_o}{\Delta\epsilon}$$

$$\log P_o = 1.00M - 4.72$$

$$d = \frac{P_o}{10^4 \pi r^2}$$

where the circular radius, r in [m], is expressed in terms of strain drop and scalar potency, P_o in [km^2 cm], which is in turn a function of magnitude, M. The total slip for a family of repeaters can the be calculated as it increases through the sequence.

4.4 Results

4.4.1 Evaluation of New Interpolation Method

As shown in Figure 4.2, we find that the gnuplot fitting algorithm is able to closely replicate the shape of GPS timeseries, including slow slip events. Note that we only use the horizontal values for the remainder of this work, as GPSGRIDDER does not compute vertical strains and GTdef can evaluate slip using only horizontal motions. The campaign psuedo timseries generated from GPSGRIDDER, once corrected as exemplified in Figure 4.3, show good agreement with observed data while maintaining a more detailed shape than if the campaign data were fit in isolation. In addition to showing that the generated timeseries are consistent with observed displacements, we also seek to establish the accuracy of this method in measuring afterslip. To this end, in Figure 4.5 we compare a single interpolated inversion from March 2015 against the inversion made using the full set of campaign observations taken at that time (Hobbs et al. 2017). While there are some discrepancies, due to data that are not perfectly fit by our algorithm and by the use of vertical components with the real data, overall we are able to generate similar features. We can see that the patch of strongest afterslip along the coastline and northwest of the EPR-CNS boundary is intact, as is a weaker version of the patch further southeast along the coastline. Slip is recorded at the shallow edge of the recoverability region offshore and along the deeper

megathrust interface in both cases, with mild variations in the extent and magnitude. Overall, this gives us confidence that this method is suitable for examining the features of the afterslip, particularly for regions that are within the network of continuous GPS, rather than at the edges. Thus, we are able to examine how cumulative afterslip evolves through time, using all available data, rather than only at discrete campaign occupations or only with the backbone continuous GPS network.

4.4.2 Progression of Afterslip & Relocking

Herein, we image the cumulative afterslip through time via a slip inversion of total displacement at monthly intervals, shown in Figure 4.4 for 2012-2013 and Movie 4.10 for 2012-2017. We see that afterslip establishes into patches very early on and then the slip in those patches increases in amplitude. It does not tend to migrate around the subduction interface. The strongest slip within the zone of recoverability is located beneath the coastline and adjacent to the EPR-CNS boundary at the "elbow" in the coastline, as discussed in Section 4.4.1. This patch develops immediately after the event and continues to grow until about mid 2014 when it reaches its maximum of 1.6 m slip. Other slip patches of note are on the deeper subduction interface and to the southeast of the "elbow". We see that another patch of slip develops beneath the tip of the Gulf of Nicoya with over 1.2 m of slip at maximum, which continues to grow throughout the entire time period considered. There is additional evidence for shallow, near-trench afterslip that extends somewhat into the zone of good recoverability, but without additional offshore data it is impossible to constrain the megathrust activity all the way to the trench.

Afterslip within the zone of recoverability reaches an equivalent magnitude of M_w 7.37 in the first month after the mainshock, M_w 7.48 by the start of 2014, and attains its peak of M_w 7.53 in late 2015 (2015.75 in Figure 4.4). This is consistent with the observation above that the area over which slip occurs is approximately fixed throughout the time considered, and only the amount of slip changes. We know this because the area experiencing slip (A)

will have a much larger impact on the seismic moment ($M_o = \mu A d$), being on the order of hundreds of kilometers versus slip (d) which is on the order of meters. It is worth noting, however, that the majority of the increase in cumulative afterslip after 2014.0 is in portion of the megathrust that is deeper than 30 km and downdip of the coseismic rupture patch. The downdip extent of the megathrust is most likely to be experiencing some viscoelastic relaxation as the earth's mantle responds slowly to the coseismic impulse, that could appear as afterslip when using an elastic model (e.g. Sun et al. 2014). Viscoelastic relaxation has typically only been considered to exert an appreciable change in surface displacements when considered over timescales larger than several years (e.g. Peltzer et al. 1998; Lin and Freed 2004; Wang, Hu, and He 2012). The remainder of this study, however, focuses on the early postseismic period of time which can unequivocally be considered afterslip, before long-term relaxation is likely to be significant, and only on the updip (15-25 km depth) slip.

4.4.3 Aftershocks & Repeaters

Figure 4.4 shows the 107,217 detected aftershocks in 2013 as well as those of Yao et al. (2017). Seismicity is spatially most abundant immediately southeast of the "elbow" in the coastline at the EPR-CNS boundary, and temporally seems to universally decline through the summer months only to increase again during the fall and winter of 2013. Figure 4.6 also displays the complete aftershock sequence with M_L up to 6.2. Although we determine an M_C of -0.46, we conservatively set it to 0.8 to ensure we are not missing events. The b-value is an important metric of the relative activity for small versus large magnitude events. Here we find a value of 0.89 for the study region (Figure 4.7).

For repeating events from 2012-2013, we find a total of 60 families, of which only 16 extend into 2013. Of those, 11 families had only two 2013 events, occurring in December; 4 families had just a single 2013 event, occurring in the spring; and 1 family had 6 events in 2013 that are distributed throughout the year. That family was also the most productive family in 2012. As shown in Figure 4.8, activity and therefore slip are both greatly reduced

in 2013. Figure 4.1 shows data availability for the year 2013. While there are at least 4 stations operating at all points in time, which may be sufficient to record any events, we cannot say with certainty that we are recording all events from a family of repeaters. We therefore cannot assume that the cumulative slip calculated here (Figure 4.8) is directly relatable to cumulative slip imaged geodetically. Rather, we comment on the temporal and spatial distribution of repeaters, to see if they are distributed similarly to afterslip.

4.4.4 Afterslip & Aftershocks

Evaluating the spatial and temporal evolution of afterslip and aftershocks in Figure 4.4, we can clearly see that areas rich with aftershocks are relatively poor in afterslip, and vice versa. This is particularly noticeable for repeating aftershocks, which are clustered at the "elbow" in the peninsula, near the EPR-CNS boundary, and around the periphery of the strongest patch of afterslip immediately northwest of that spot. We also confirm the previous finding (Hobbs et al. 2017) that both aftershocks and afterslip are most abundant within a confined depth range of roughly 15-25 km, immediately updip of the main coseismic rupture region.

4.5 Discussion

4.5.1 GPS Network Design

As was demonstrated in Section 4.4.1, the new methodology described herein is able to successfully reproduce the approximate extent of the largest afterslip patches, consistent with the afterslip observed during the campaign occupation of 2015. What makes it valuable, however, is how it can extend our temporal and spatial observing power by simply incorporating all sources of GPS data to generate continuous, observation-based timeseries at all stations. Otherwise, it has been common practice to use only one type of GPS data. One could use continuous observations for timeseries processing (e.g. Jiang et al. 2012; Malservisi et al. 2015; Voss et al. 2017) or one could consider campaign GPS only for

simple applications: assumed linear interseismic behavior (Ruegg et al. 2009; Feng et al. 2012, e.g.) or isolated snapshots of total slip (e.g. Perfettini and Avouac 2007; Hobbs et al. 2017). This technique, on the other hand, is able to more efficiently incorporate multiple datasets with variable sampling.

However, this technique does requires many measurements to interpolate with, and as such these findings bear on design of future GPS networks. We recommend that campaign stations, where possible, should be incorporated inside of continuous networks rather than at their periphery. The continuous networks should be prioritized near any regions known to exhibit slow slip events, as these are nearly impossible to capture with campaign occupations. Where feasible, we would also recommend rotating campaign instruments between sites. This allows for improved accuracy in the scaling of timeseries (Section 4.3.1) while using nearby continuous stations to determine the overall shape. Whereas without this methodology those rotating campaign data would not have been valuable enough to justify their collection, this approach could fully utilize those observations to constrain deformation timeseries and the largest possible number of stations.

4.5.2 Anticorrelation of Afterslip and Repeating Aftershocks

The most important result of this work is to show the true anticorrelation of afterslip and repeating aftershocks, even when their temporal evolution is considered. In other words: both in time and in space, the highest concentration of repeating aftershocks is not correlated to the highest afterslip. This is even despite the consensus in the literature that repeating aftershocks are an indicator for slip (e.g. Matsubara, Yagi, and Obara 2005; Uchida and Matsuzawa 2013; Dominguez, Taira, and Santoyo 2016; Weston and Shirzaei 2016; Huang et al. 2017; Uchida and Bürgmann 2019). The key difference between this and other studies, though, is that the Nicoya Peninsula offers a rare opportunity to use land-based geodetic techniques directly over the seismogenic portion of the megathrust. This comparison has never been done before for a megathrust environment. In Japan and Chile, for example, the

coeismic slip zone is exclusively offshore. This results in poor recoverability of slip, just as we find for the near-trench region of Nicoya (Figure 4 in Hobbs et al. 2017). Hence, findings here suggest that reports of colocated afterslip and repeating aftershocks may be an artifact of poor geodetic slip recovery offshore. Certainly it calls into question the use of repeating aftershocks as a proxy for the amount of slip occurring on the megathrust, as such a technique would have in this case missed the regions of greatest slip.

We do note, however, that some repeating aftershocks do occur around the periphery of large afterslip patches (Figure 4.4). This is consistent with previous studies showing that repeating aftershocks should nucleate in the transitional zone between velocity weakening and velocity strengthening materials (Chen and Lapusta 2009) but not in all velocity strengthening regimes. We therefore caution that a paucity of repeaters does not indicate a paucity of slip, and that more work is needed to adequately describe the relationship between these megathrust behaviors in regions with sufficient seismic and geodetic data.

4.5.3 Megathrust Stress and b-value

The b-value has been likened to the state of stress on the fault interface (e.g. Wyss 1973; Schorlemmer, Wiemer, and Wyss 2005), as it represents the ratio of large to small earthquakes. Globally, b-value is approximately 1 (Stein and Wysession 2003), and 1.06 for a previous study in Nicoya (Ghosh et al. 2008). The b-value determined in this study is 0.11 lower than the global average, suggesting that this sequence is mildly depleted in large events. Importantly, though, the reported b-value of 0.89 is also lower than the value of 1.06 which was previously reported for the Nicoya megathrust (Ghosh et al. 2008). Overall, this suggests the aftershock sequence was depleted in relatively larger events. Also, this lower b-value indicates that the differential stress is higher or that the megathrust is stronger now than it was during the previous interseismic (e.g. Schorlemmer, Wiemer, and Wyss 2005; Ghosh et al. 2008; Scholz 2015). This finding is consistent with Tormann et al. (2015) who found that b-values increase and then return to preseismic levels or lower shortly after

a large megathrust event. It is also possible that the b-value could have decreased in the years leading up to the 2012 mainshock (Nanjo et al. 2012; Schurr et al. 2014), hence the postseismic value appears overall lower than that observed in the mid-2000's.

In addition to comparing our overall b-value to the b-value map of Ghosh et al. (2008), we also compare afterslip and aftershocks to that previous b-value map to evaluate spatial heterogeneity. Figure 4.9a shows an interesting relationship between preseismic b-values and postseismic response, particularly along the coastline in the 15-25 km depth range on the megathrust. Most clearly, we see that the patch of strongest afterslip (navy contours) is well-mapped by the region of lowest b-value prior to the earthquake (blue and purple region). Conversely, the region of anomalously high b-value (orange region) at the southeastern tip of the peninsula overlaps with a patch of strong aftershock seismicity that was devoid of repeaters (black dots). In between, changes from those extreme b-values to more moderate values (green regions) are well aligned with the transitions between patches showing intense aftershock seismicity or afterslip. These moderate b-values of Ghosh et al. (2008) are still greater than average (1.2-1.5 versus 1). Although it has been suggested that b-value mapping can be used to determine locking (e.g. Wiemer and Wyss 2002; Ghosh et al. 2008; Schurr et al. 2014), we find that b-value mapping was, retrospectively, better suited to predicting the region of maximum afterslip (e.g. De Gori et al. 2012) — a relationship that bears further investigation in the future.

4.5.4 Aftershock and Afterslip Forecasts Need Interface Mapping

In trying to understand, and perhaps one day forecast (e.g. Steacy et al. 2013), subduction zone behavior, the scientific community wants to understand the causal relationship between process and response. Some studies suggest that afterslip is driving aftershocks (e.g. Kato 2007; Chan and Stein 2009). Others suggest that mainshock seismicity, rather, drives both slip events and aftershocks (e.g. Toda and Stein 2000; Lange et al. 2014). What we see in the current results, as well as from previous studies of the Nicoya Peninsula (e.g. Ghosh

et al. 2008; Chaves and Schwartz 2016), is that regardless of the stress driver, the behavior of the megathrust appears to be dominantly controlled by long-lasting heterogeneities on the subduction interface rather than by stresses imposed by either the mainshock or post-seismic slip. In other words: knowing about the stresses won't be enough information to anticipate the response on the megathrust unless you know something about the physical properties.

For illustration, we plot the Coulomb stress changes (Toda et al. 2011) induced by the 2012 mainshock. We use regional principal stresses as the average of those given in the World Stress Map for the study area (Heidbach et al. 2018), and the coseismic slip model of (Kyriakopoulos and Newman 2016), within the zone of recoverability (Hobbs et al. 2017), so as to be consistent in using geodetically determined slip. Presented in Figure 4.9 are the maximum Coulomb stress changes for optimally oriented faults in the depth range 15-25 km, where we see maximum afterslip and aftershocks. We chose this depth range to examine the stresses contributing to the clustered aftershock activity and afterslip within that depth range (ex: Figure 4.5). We didn't prescribe a receiver fault plane because we do not have focal mechanism information for this dataset.

Generally we see that there are Coulomb stress increases well in excess of the 1 bar threshold for triggering (Freed 2005) distributed across effectively the entire region under consideration (15-25 km depth along the coastline). If we had wanted to predict the location of aftershocks, one might have generated this map in 2012 and suggested that aftershocks should occur all along the coastline. This would not have addressed the spatial heterogeneity of the afterslip and aftershocks at this depth. Clearly, Coulomb stress alone cannot explain the relative dominance of afterslip and aftershocks, although both are likely driven by the stresses imparted coseismically. We would instead recommend a strategy which integrates information about the mainshock as well as the megathrust properties when trying to constrain a region of expected aftershock activity.

4.6 Conclusion

Incorporating GPS data that has gaps in continuity or has variability in network size represents a serious challenge for geodecists, and results in underutilization of data. We present a new methodology for jointly analysing campaign and continuous GPS data through fitting and elastic interpolation. This physics-based approach allows one to maximize information extracted from heterogeneous datasets, by incorporate all available data for timeseries analysis. For a single snapshot in time during a campaign GPS occupation, we show that this method is able to produce surface displacements which, when inverted, show similar features to the direct observations. With this in mind, we consider the time evolution of afterslip through the first several years after the 2012 M_w 7.6 mainshock. It shows slip patches that establish early on and then subsequently accumulate slip, particularly in two patches beneath the coastline.

With this technique, campaign occupations that are rotated between stations could be fully incorporated with continuous data at a lower cost than trying to maintain the equivalent number of fully continuous sites. Monitoring schemes which are low cost or require only intermittent occupation are particularly valuable in places where budgets for telemetry or instrumentation are low, where instruments are sitting on shelves rather than collecting seemingly 'random' short term data, or where conditions prohibit all but the sturdiest of GPS installations for part of the year. The latter, for example, may work well in polar environments where a small backbone network can be emplaced through the winter with supplementary campaign occupations through the summer months.

Additionally, we extend the dense aftershock catalog of Yao et al. (2017) through 2013 using the WMF technique. An additional 107,217 events are detected, with M_L up to 6.2. Of the 60 repeating aftershock families identified, only 16 extend into 2013 and with much lower productivity than they experienced in 2012. Overall, we are able to use the time-variable afterslip and 1.3 year aftershock catalog to conclusively report that the strongest

afterslip and aftershock seismicity, including repeating aftershock activity, are anticorrelated both spatially and temporally. This finding, which is taken in a unique location where ground-based geodetic techniques can directly measure updip afterslip, bears strongly upon the use of repeating earthquakes as proxy strain meters. While it has become common to use repeating events to measure slip on the subduction interface, this study shows that areas of strong slip may be missed with that technique. Because repeaters are thought to occur in conditionally stable regions, numerical modeling may help us understand the current result regarding repeaters and afterslip, particularly in regards to locations with slip but no seismicity. Future offshore geodetic measurements will be invaluable in further constraining the relationship between megathrust slip and the seismic signals it produces.

We also find that updip afterslip and aftershocks occur at a location and depth which experienced positive Coulomb stress change from the mainshock. However, the discrete occurrence of aftershocks versus afterslip appears to be determined by conditions that preexisted the 2012 event, based on b-value mapping in the 2000's. We therefore conclude that aftershock forecasting should incorporate as much information about megathrust properties as possible, to determine regions which are likely to behave in a slip-weakening versus a slip-strengthening manner when subjected to mainshock stress changes.

4.7 Acknowledgements

All GNSS data is available through UNAVCO archives (`http://unavco.org`). Model outputs are available from the Nicoya Seismic Cycle Observatory (`http://nicoya.eas.gatech.edu`). This project is funded through NSERC PGSD2-488063-2016 to T.E.H. and NSF 1447104, 1262267 to A.V.N. This work used the Extreme Science and Engineering Discovery Environment (XSEDE), which is supported by National Science Foundation grant number ACI-1548562. Figures prepared using Generic Mapping Tools (GMT), Matlab, and Gnuplot. Field work would not have been possible without support from UNAVCO and OVSICORI, and the assistance of J. Buffo, B. Burgoa, K. Gardner,

M.S. Kemmerlin, J. Méndez, J. McAdams, C. Muller, D. Sánchez, and A. Williamson.

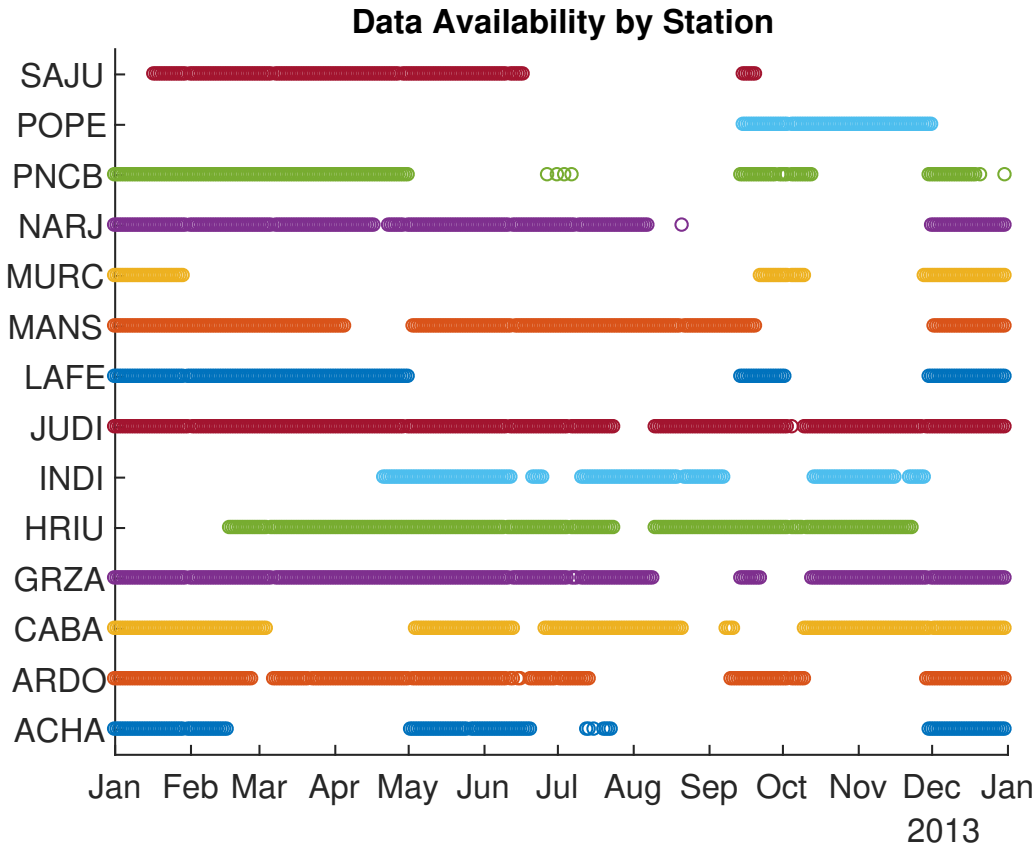

Figure 4.1: Availability of daily waveforms, through 2013, at all stations used in this study.

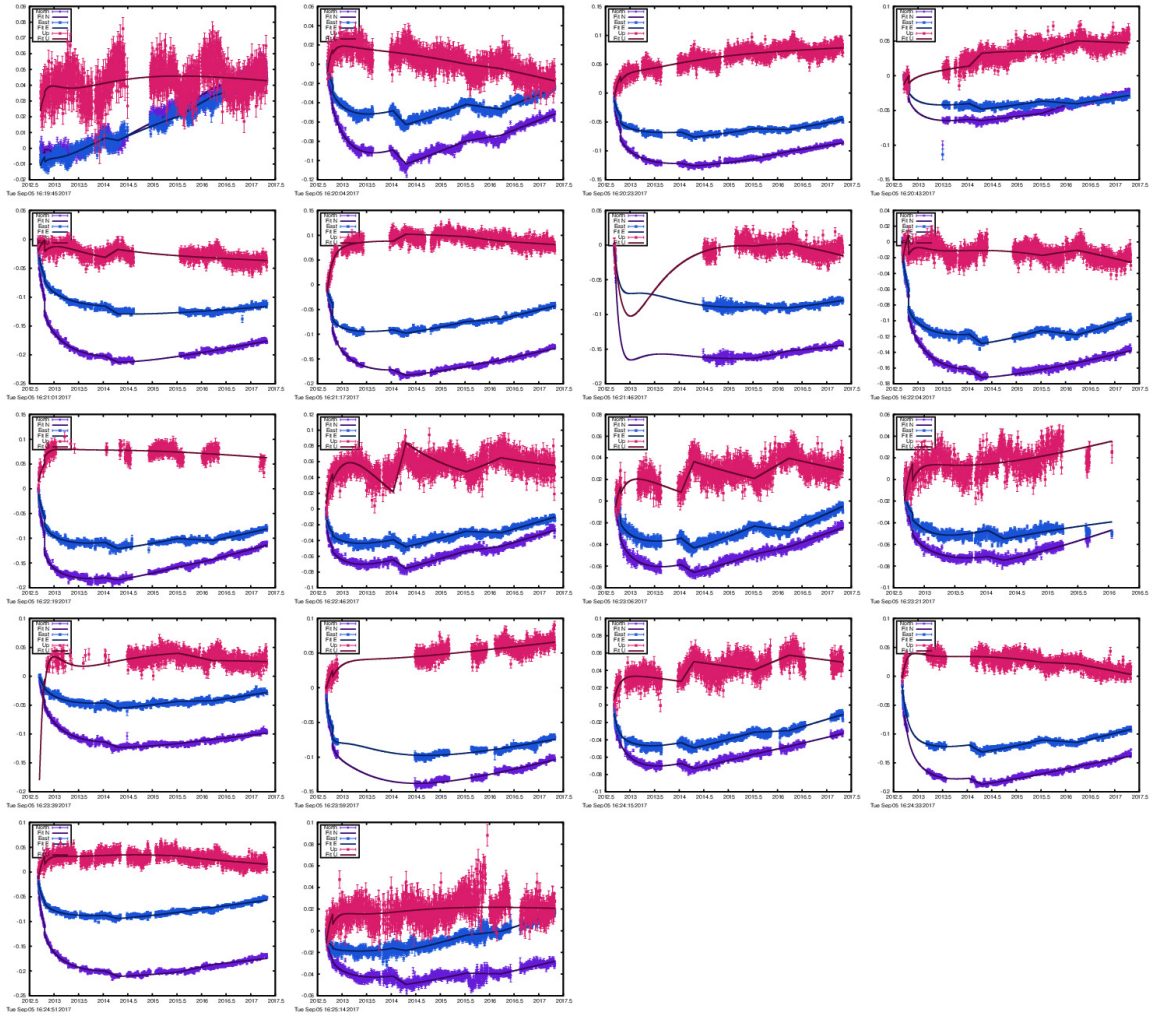

Figure 4.2: Functional fits to observed continuous GPS data, as described in Section 4.3.1. North is shown in purple, east in blue, and upwards in pink. Data are dots with vertical error bars, and fitting functions are shown as lines.

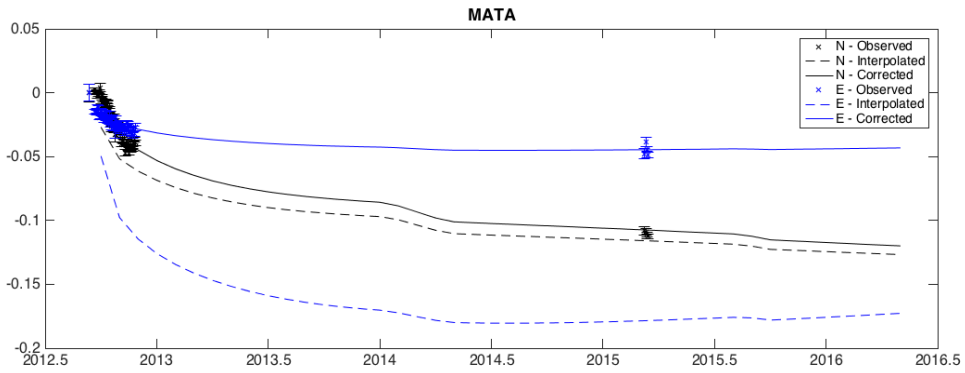

Figure 4.3: Example of corrected campaign GPS data for station MATA, with east component in blue and north in black. Observations (x's) are better fit by corrected data (solid line) than by the dashed lines which were output from the 2D interpolation alone. Note that resulting time series (solid lines) are still richer in information than a simple relaxation curve for these same data.

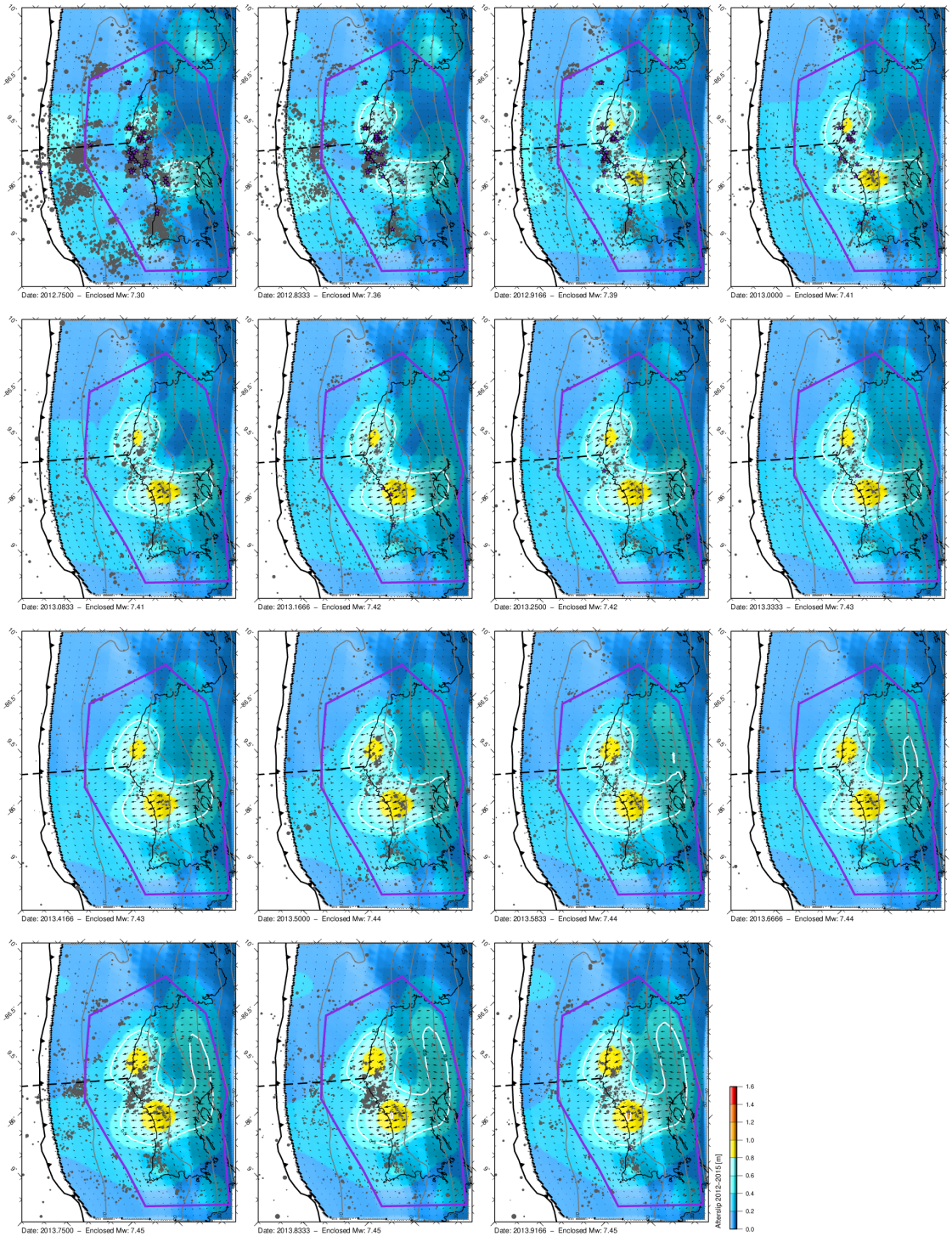

Figure 4.4: Continued, with caption, on following page.

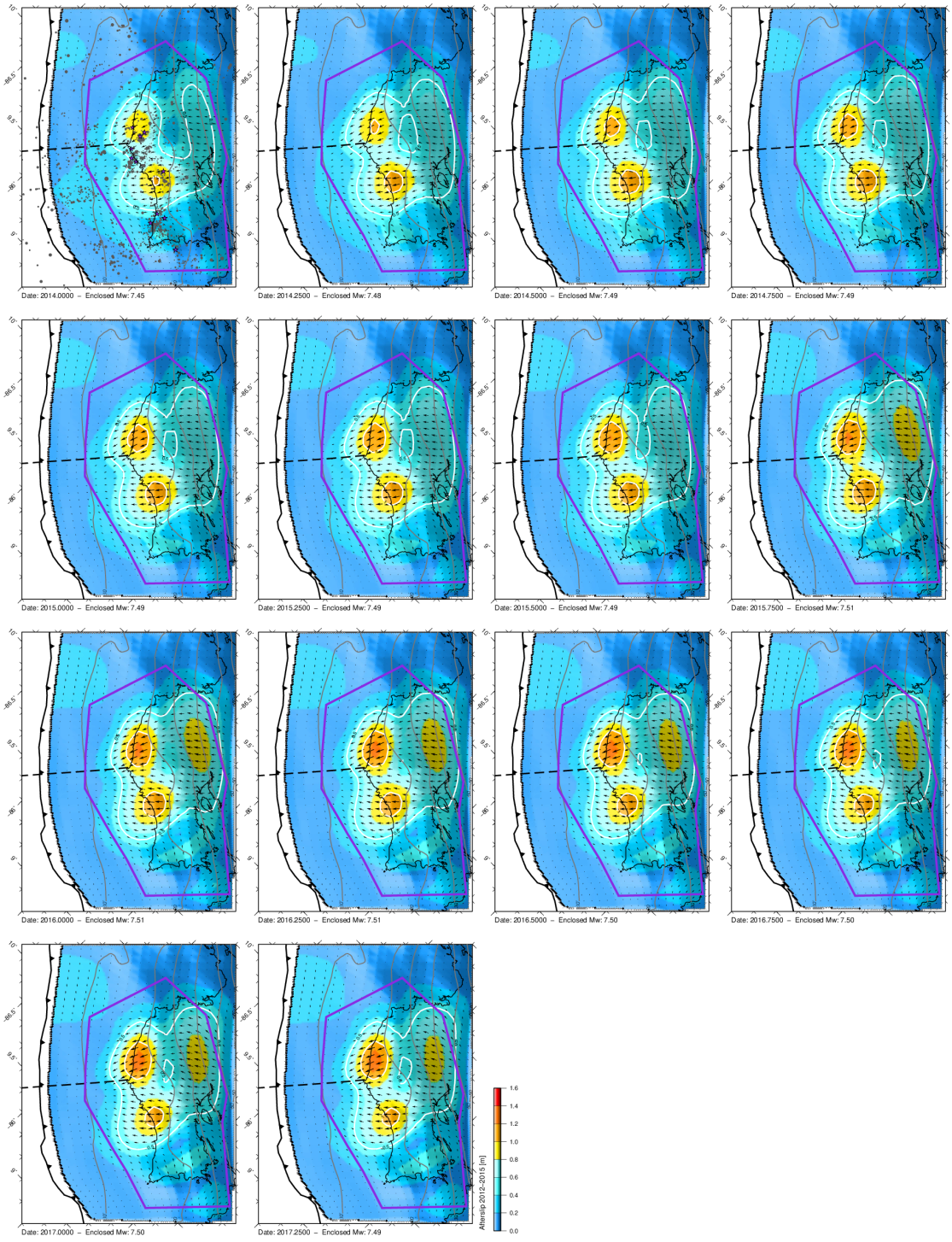

Figure 4.4: Result of slip inversion, taken at monthly intervals, using interpolation method. Region of high recoverability and resolution indicated by purple polygon. Repeating earthquakes shown as purple stars. EPR-CNS boundary shown as dashed black line. Slip, scaled from blue to red as 0-1.6 meters. We see that slip evolves on the north side of the EPR-CNS divide near the coastline, as well as in the deeper region of the megathrust. The strongest repeating earthquake activity, however, is tightly clustered immediately southeast of that area — suggesting an anticorrelation.

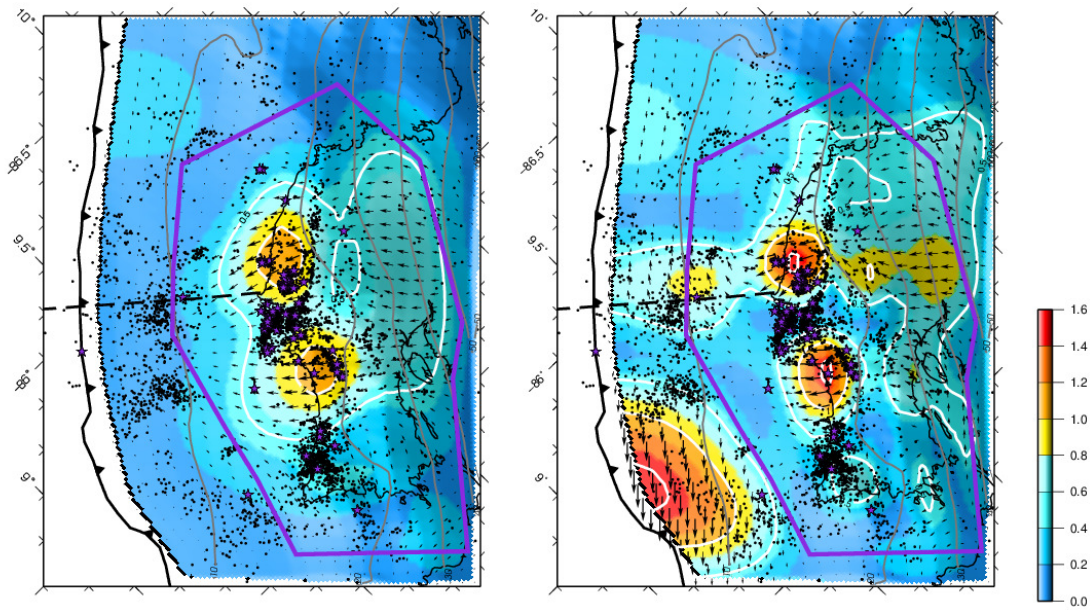

Figure 4.5: Result of slip inversion, taken at the time of the 2015 campaign, using interpolation method (left) and real data (right, from Hobbs et al. 2017). Region of high recoverability and resolution indicated by purple polygon. Repeating earthquakes from immediately after earthquake to end of 2013 shown as purple stars, all other seismicity shown as grey circles. EPR-CNS boundary shown as dashed black line. Slip, scaled from blue to red as 0-1.6 meters.

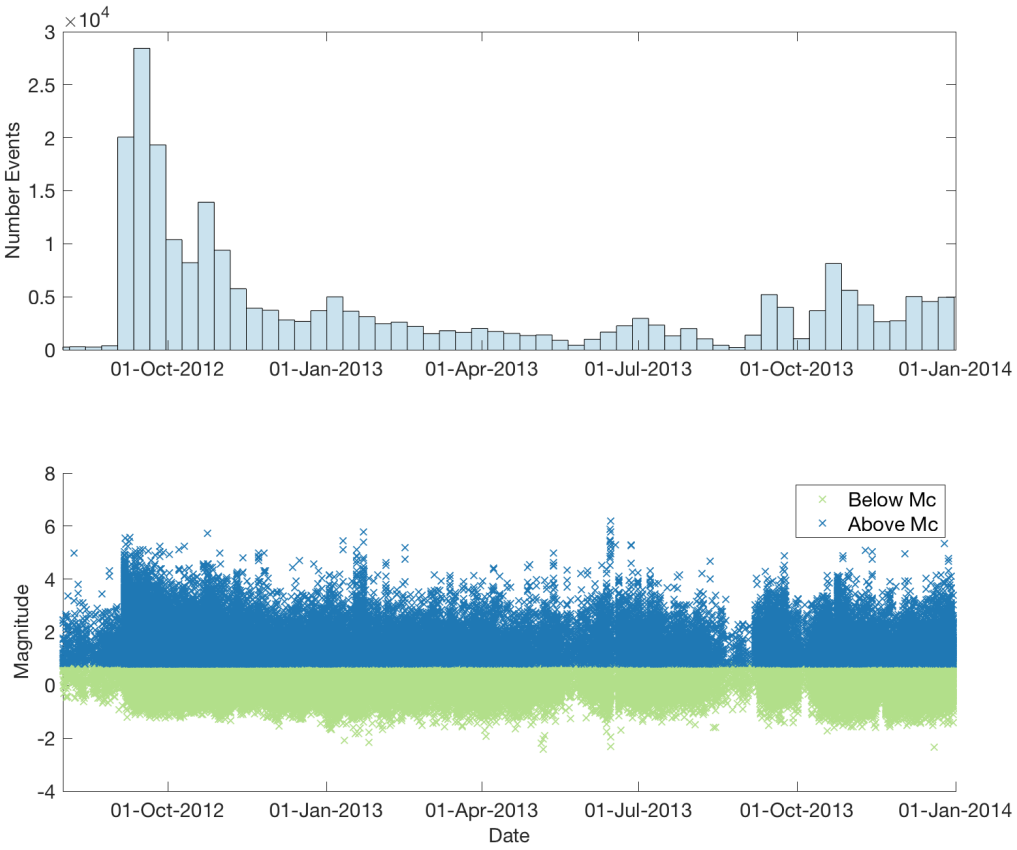

Figure 4.6: All aftershocks from this catalog and that of Yao et al. (2017), from immediately after the 2012 M_w 7.6 event until the end of 2013. Top panel shows the number of events through time, while bottom panel shows the magnitudes (M_Ls). Note that all events with magnitude below M_C are shown in green.

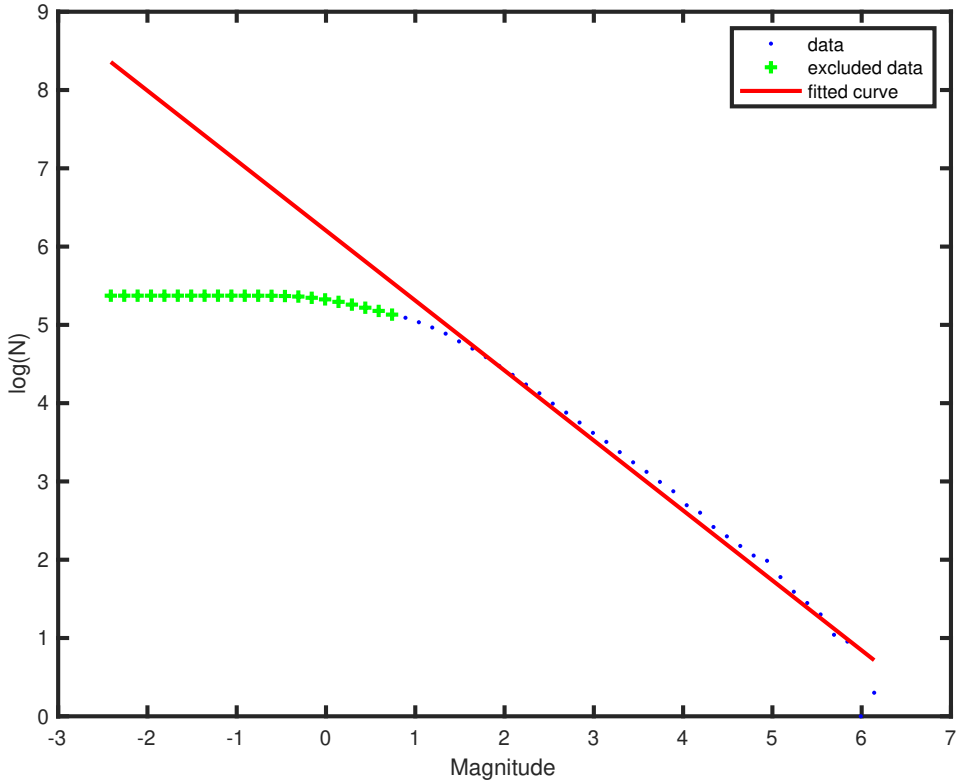

Figure 4.7: Gutenberg-Richter relation for all aftershocks shown in Figure 4.6. Excluded events, with magnitude below M_C, are shown in green. Line of best fit is shown in red, for data shown as blue dots.

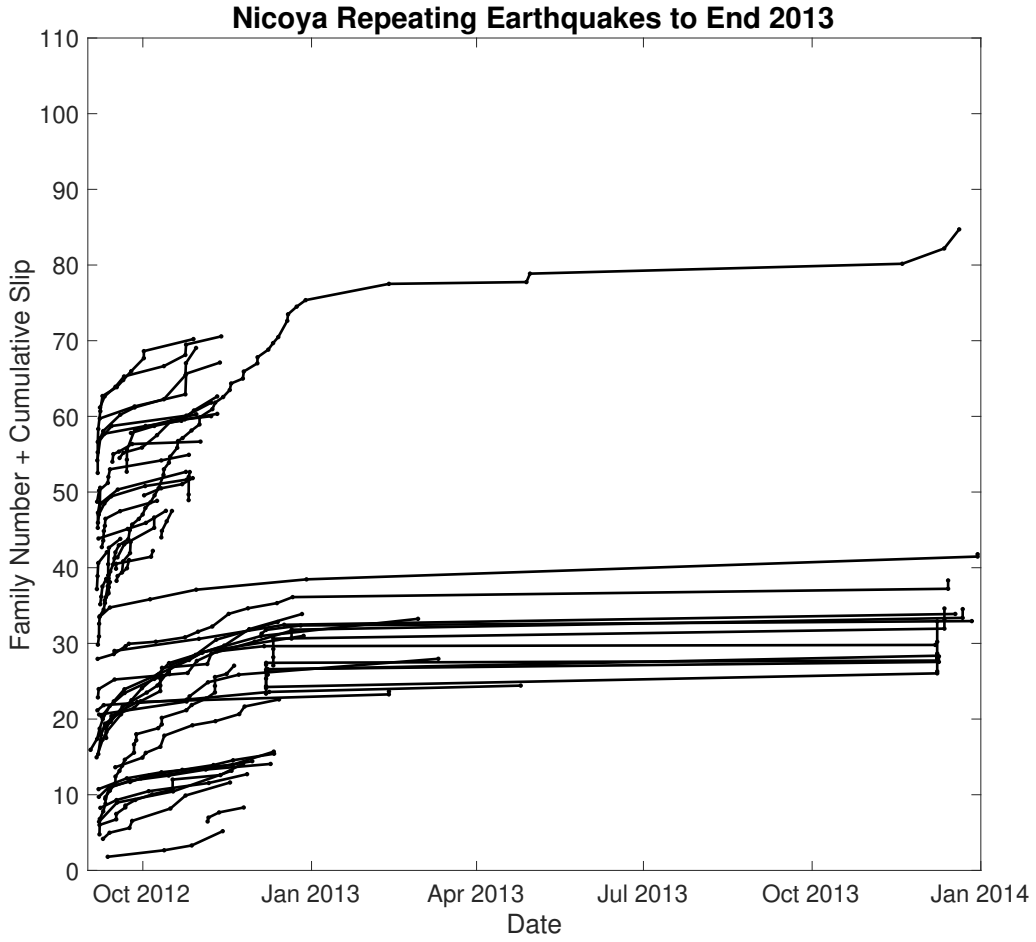

Figure 4.8: Cumulative slip for each family of repeating earthquakes, from 2012 (Yao et al. 2017) through 2013 (Section 4.3.2).

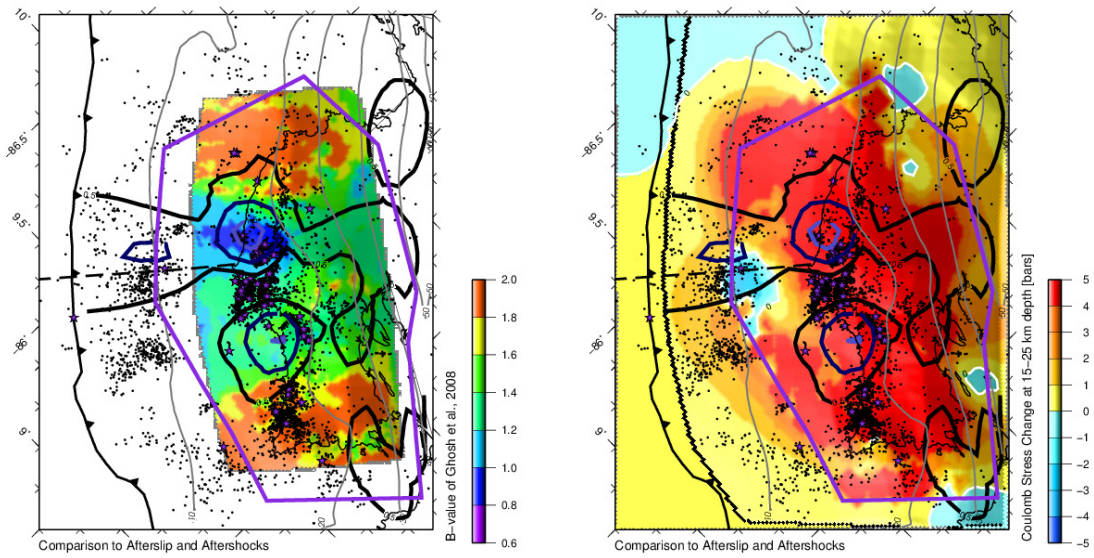

Figure 4.9: Comparison of afterslip / 2012-2013 aftershocks against (left) b-value mapping of Ghosh et al. (2008) and (right) results of Coulomb stress calculation. Afterslip is shown as navy blue contours ranging from 0-1.5 m slip. Grey points are all seismicity, with repeating aftershocks shown by purple stars. Purple polygon is the region of good recoverability for afterslip.

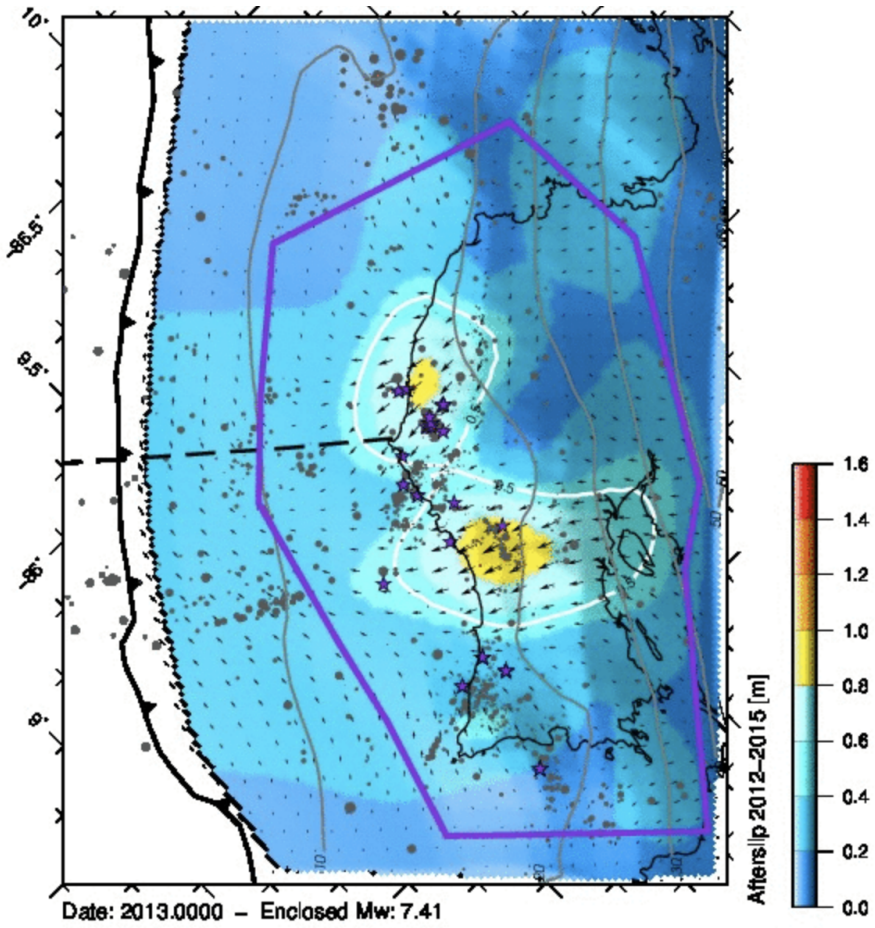

Figure 4.10: Full movie can be found at `http://geophysics.eas.gatech.edu/people/thobbs/outputs/3DInterp_2012-2017_final.gif` — above is only a still representation. Movie is the full version of Figure 4.4, showing monthly progression of cumulative afterslip and overlain aftershocks (grey for regular events, purple stars for repeaters). Polygon shows region of good recoverability.

Table 4.1: Goodness of Fit Evaluation for Gnuplot Fitting Algorithm

	Average Reduced Chi Squared			
Number of Exponential Terms	North	East	Up	**Total**
1	6.088	3.106	1.777	3.657
2	3.894	2.441	1.577	2.637
3	3.551	2.268	1.534	2.451

CHAPTER 5
CONCLUSION

5.1 Primary Findings

This work has used geodetic and seismic instrumentation to observe the deformation of the Nicoya Peninsula in the 5 years following the 2012 Moment Magnitude (M_w) 7.6 earthquake. This was achieved using data from the Nicoya Seismic Network, 18 continuous Global Positioning System (GPS) stations and a set of 22 campaign GPS sites. By considering the displacement, and its corresponding annual velocity, I documented the nonlinear decrease of seaward trench-normal motion (afterslip) between 2012 and mid 2014. At this time, the signal became exclusively trench-parallel across the entire forearc — something that has never been observed prior to this work. By 2016, trench-normal motion was observed again and by 2017 the network showed wholesale landward velocities consistent with the previous interseismic velocities of Feng et al. (2012).

I also developed a new methodology for combining campaign and continuous GPS observations into interpolated timeseries. This allows for use of all possible data over the time period considered, rather than selecting a lower spatial or temporal coverage. For example, in Chapter 2, I considered afterslip that had accumulated by March of 2015 not because that time was meaningful for the postseismic signal, but because that was when there were campaign measurements. This new methodology allowed for imaging of the early afterslip signal at any point in time, using all 40 GPS stations with consistent network geometry.

Building off the aftershock and repeating earthquake catalog of Yao et al. (2017), in Chapter 4 I detect more than 100,000 additional aftershocks with catalog completeness down to Magnitude of Completeness (M_C) 0.8. Repeating aftershocks are shown to have

decreased in activity dramatically in 2013.

Converting GPS surface observations into megathrust behavior was accomplished via linear elastic inversion in GTdef (Chen et al. 2009). Afterslip was shown to have slip equivalent to a M_w 7.5 event inside of the zone of recoverability. This suggests that the afterslip may have released more stored energy than the mainshock if there is additional slip near the trench, although it is beyond our resolving power to image it. The highest slip, 1.7 m, was updip of the coseismic rupture and split into two patches. These patches are observable either using the cumulative afterslip up to the March 2015 campaign (Chapter 2), or using the new interpolation methodology described in Chapter 4. I show conclusively that these afterslip patches are anticorrelated to aftershocks both in space (Chapters 2 & 4) and in time (Chapter 4). This is particularly notable for the repeating aftershocks, which are thought to be a proxy for aseismic slip (e.g. Nadeau and McEvilly 1999; Igarashi, Matsuzawa, and Hasegawa 2003; Matsuzawa et al. 2004; Uchida and Matsuzawa 2013; Hu et al. 2016).

Using the backslip method for the period after the afterslip signal is diminished, I show that relocking initiates first in 2014. However, it is interrupted by the Postseismic Sliver Transient (PST) described in Chapter 3, before resuming in late 2015. By mid 2016 the interface shows a patch of strong locking under the central peninsula, which replicates the extent of coseismic rupture from 2012 more closely than it matches the pre-2012 locked patch (Kyriakopoulos and Newman 2016).

Afterslip is known to be a period without megathrust coupling, as aseismic sliding is occurring. During the PST, backslip imaging shows that megathrust locking is also effectively zero. This finding of exclusively trench-normal afterslip or exclusively trench-parallel PST, both with effectively no megathrust coupling, suggests that slip partitioning of oblique subduction zones may be controlled by the state of megathrust locking. Outside of these times, during the pre-2012 and post-2015 interseismic periods, coupling is higher and surface velocities are oblique.

5.2 Impact

The Nicoya Peninsula provides a unique opportunity to study a megathrust from directly above the seismogenic zone (Figure 1.4). In the wake of the 2012 M_w 7.6 Nicoya earthquake, I have completely characterized the deformation as it pertains to the afterslip and relocking patterns of an oblique subduction zone. Summarizing my findings, I have discovered 3 surprising and important features:

1. Afterslip and aftershocks are clustered separately of one another along the updip edge of coseismic rupture. This is not consistent with the theory of repeating aftershocks as slip meters, nor with the results of stress modeling from the mainshock rupture.

2. Relocking is interrupted by an episode of purely trench-parallel forearc motion, following the purely trench-normal afterslip. Thus, I document the first ever instance of transient slip-partitioning, seemingly controlled by megathrust coupling, in an otherwise obliquely deforming subduction zone.

3. The Nicoya Asperity, which appears to be associated with the change in subduction angle at the suture of oceanic crust sourced at the East Pacific Rise (EPR) and Cocos-Nazca Spreading Center (CNS), is consistent through seismic cycles.

5.2.1 Megathrust Behavior Driven By Physical Properties of Interface

These findings strongly influence how we view stresses on the megathrust. Whereas many models show a subduction zone as a two dimensional (2D) structure (e.g. Peng and Gomberg 2010), we are learning that complex three dimensional (3D) models (e.g. Lay et al. 2012) are more consistent with observations. Said another way, we can't use depth within a subduction zone to determine what behavior the fault will display. Along the 15-25 km depth range in Nicoya we see alternating patches of densely clustered aftershocks or afterslip, varying along strike rather than along dip. This alternation of behavior cannot be

accounted for by some stress heterogeneity caused by the mainshock, as shown in Chapter 4. And thus, it suggests that, because imparted mainshock stresses were similar throughout this depth range, the response to either nucleate aftershocks or experience afterslip may be tied to some property of the megathrust. This points to a strong need for mapping of megathrust properties in order to assess seismic potential. For example, the patch of greatest afterslip in Nicoya matches well with a region identified as having low b-value, suggesting a strong fault, prior to the mainshock (Ghosh et al. 2008). The same region was shown to sit immediately updip of a change in subduction angle (Kyriakopoulos et al. 2015; Kyriakopoulos and Newman 2016), upon which the mainshock nucleated. Both of those results were determined using seismic methods, which do not require the proximity of land to the seismogenic zone. This strongly supports the idea that b-value mapping and precise determinations of slab geometry can help identify regions which are likely to fail as large earthquakes versus those which may slip aseismically. Particularly, this could be useful in a place like the Alaskan-Aleutian subduction zone, which has plentiful seismicity but poor geodetic access to the offshore seismogenic zone.

5.2.2 Asperities Remain Through Multiple Seismic Cycles

This point is reinforced by the finding that an asperity, like the Nicoya coseismic rupture patch delineated in Figure 3.2d, can remain in place between seismic cycles. As such, it implies that one could anticipate a fault to behave similarly between earthquake cycles and therefore previous behavior may be considered predictive of the future behavior. A patch which experiences slow slip in one interseismic will likely continue to behave that way after a mainshock. Voss et al. (2017) found that this has appeared to hold true so far in Nicoya. However, this finding should be taken cautiously. It has been shown that great earthquakes, with energetic rupture, can extend outside of the region which is favorable for earthquake generation (e.g. Lay et al. 2012). Therefore, as was soberly shown by the Tohoku-Oki earthquake (Ozawa et al. 2011), one should not assume that a large earthquake

necessarily represents the largest possible earthquake on a subduction zone. Investigating the previous 1950 earthquake, using the same seismic stations as were used to consider the 2012 event, may help to illuminate changes to the mainshock asperity.

5.2.3 Repeating Aftershocks Do Not Match Afterslip

Given that it has become quite common to use repeating aftershocks as a proxy for slip (see Uchida and Bürgmann 2019, and references therein), the finding that they do not match one another has serious ramifications. Nadeau and McEvilly (1999) found that the repeating earthquake-inferred slip rates qualitatively matched the rate of surface deformation taken from repeated fault offset measurements on the Parkfield section of the San Andreas. Igarashi, Matsuzawa, and Hasegawa (2003) used land-based GPS to compare with slip accumulated from repeating events, but did not have high geodetic resolution in the area of interest or alignment of the time periods being considered. In other words, surprisingly little work has been done to validate the repeating earthquake hypothesis with high fidelity, colocated, contemporaneous geodetic data. We show that in this case, meeting those requirements, repeating earthquakes tend to be clustered outside of the region of highest afterslip. Hence, a slip distribution estimated from this result would tend to misdirect slip into regions that we can presently say are relatively poor in afterslip. Therefore, this methodology should not be used without further testing in fault environments with quality geodetic data.

5.2.4 Sliver Motion is Not Constant

This work illuminates the timing and spatial heterogeneity of the relocking signal, which is interrupted by an observed PST. Notably, all of this came after a period of purely trench-normal afterslip. Partitioning of slip into purely trench-normal and trench-parallel components was documented during the postseismic, despite observations of oblique interseismic convergence. This unexpected complexity means that trench-parallel motion is not at a

constant rate — it was diminished during the coseismic and afterslip phases, and increased to slightly higher than average levels during the PST. While there is currently no evidence for an increase in seismicity on the forearc bounding fault during the PST, it suggests that hazards along this or similar faults in other subduction zones may vary with time. Additionally, it indicates that slip partitioning may be a function of megathrust coupling. This would marry an observation that is made across the surface of the entire forearc (obliquity) with a sought after value that dictates the expected size of rupture (coupling).

5.2.5 Afterslip and Sliver Transient Refute Tectonic Escape Model of Central American Tectonics

Furthermore, the above finding is strictly incompatible with a proposed 'tectonic escape' model of Central American tectonics. In that scheme (LaFemina et al. 2009; Kobayashi et al. 2014), northwest motion of the Central American Forearc is driven by outward forcing of the Panama Microblock in response to the indenting Cocos Ridge (Figure 1.6). This forcing would be constant, as the Cocos Plate is uninteruptedly being driven under the Panama Microblock. Exclusively trench-normal afterslip, on the other hand, indicates that trench-parallel motion or a lack thereof is controlled by the local megathrust environment, which experience the 2012 mainshock, rather than a distal source. This finding suggests that we must reject the 'tectonic escape' model, and implement only the simpler oblique subduction model for driving large-scale northwest translation of the Central American Forearc.

5.3 Future Research and Outstanding Questions

As is the way of scientific progress, the impactful results of this work lead to several subsequent avenues of inquiry. Here I suggest the most pertinent studies for further evaluating the findings presented.

5.3.1 B-value Mapping with the Nicoya Aftershock Catalog

Although I discuss the overall character of the catalog b-value, using the full set of Waveform Matched Filter (WMF) aftershocks to map the changes in b-value on the fault interface would be a logical next step. The catalog has over 200,000 events and a magnitude of completeness near 1, making it a sufficiently high resolution dataset for such work. It would truly determine whether the imaged patch of low b-value, which corresponded to the patch of highest afterslip, was constant through a seismic cycle. If so, it corroborates the finding in Section 5.2.2 that the physical properties of the subduction zone, as they relate to the behavior of the megathrust, are constant between seismic cycles. Additionally, one could use seismicity in the time between the mainshock and the work of Ghosh et al. (2008) to determine if b-values changed in the coseismic rupture area leading up to the mainshock.

5.3.2 Consideration of the Effect of Hurricane Season on Aftershocks

Figures 4.4 and 4.6 clearly show a decrease in seismicity in the late summer or early autumn of 2013, with activity increasing in September to December of that year. This observation, however, will require further analysis to prove if it is statistically significant. Incidentally, September–December is both the time period in which the template earthquakes were selected (Yao et al. 2017), and the time of major rainfall from cyclones. As shown in Figure 5.1, the North Pacific coast of Costa Rica experiences wet and dry seasons, with the wet season having two peaks separated by the 'veranillo' or little summer. The second and largest peak corresponds to the peak in hurricane activity in the Caribbean, and is responsible for 46% of the annual rainfall in this part of Costa Rica (Energía 2001; Waylen and Harrison 2005). Although 2013 had below average hurricane activity, Mexico was hit harder than average (Kimberlain 2014). At the same time in September 2013, Mexico was hit by two tropical storm systems from different oceans (Pedrozo-Acuña, Breña-Naranjo, and Domínguez-Mora 2014), both of which became hurricanes as they made multiple landfalls. Given that rainfall is known to increase in Costa Rica as a result of tropical cyclones in the

Caribbean, it bears considering whether there is a link between rainfall and seismicity in the fall of 2013.

Alternately, due to the methodology, this tentative observation of increasing seismicity in September–December may be an artifact of using template events from the same time period in the year previous. Therefore, if we can determine that in other catalogs the overall seismicity rate is constant through fall 2013 then this apparent increase in activity is just an increase in activity on the fault planes that were most active in fall 2012. This is also a striking result, as it indicates that different fault planes are active at different times of the year, and may still imply a seasonal connection. In either case, this preliminary finding should be examined further, particularly using a larger set of template earthquakes.

5.3.3 Evaluate Potential Relationship Between Obliquity of Subduction Zones and Geodetic Locking

Herein I document a strong correlation between slip partitioning and a dearth of megathrust locking — or, alternately, a correlation between obliquity of surface velocities and megathrust locking. If so, then there is the possibility of using obliquity measurements as a proxy for relative coupling of the megathrust through the seismic cycle. Because these obliquity measurements exist across the forearc, such a technique would not rely on the proximity of land to the seismogenic zone that exists in Nicoya. And as most subduction zones are oblique to some degree, it could be widely useful. The other advantage is that obliquity can be quickly estimated from surface displacements, whereas locking is a derivative value based on the surface displacements, fault geometry, network resolution, and regularization scheme. Dense postseismic measurements in the near-trench region will be essential to an improved understanding of such complexities, as the updip limit of locking remains enigmatic in many environments (e.g. Wang and Tréhu 2016). Target subduction zones for evaluating this link would be places where geodetic coverage is sufficient to constrain the amount of locking through time, such as in Japan, New Zealand, or the nearby Osa

Peninsula in Southern Costa Rica.

5.3.4 Look for Transient Sliver Motion at Other Subduction Zones

It will also be important to evaluate the time evolving nature of sliver motion at other subduction zones as it may reveal unexpected complexity like that observed in Nicoya. This would be simple to complete alongside the previous goal, as it relies on similar data. Changing rates of sliver motion would be particularly important for constraining accumulated strain energy, and hence seismic hazard, in subduction environments where the forearc-bounding fault is expected to be seismogenic. For this reason, this work would be well suited for the Sumatra Fault (Ito et al. 2016). This fault system is analogous to the Nicoya case in terms of tectonic arrangement, except that this fault has experienced increased seismicity since the 2004 Sumatra-Andaman Earthquake and runs the entire length of the Sumatran Island. Thus, for the over 50 million residents of Sumatra (Indonesia 2011) this fault presents a considerable hazard.

5.3.5 Continue Evaluating Repeating Aftershock Slip Against Geodetic Slip

Finally, and most importantly, this work has shown that the densest regions of repeating earthquakes do not correlate with afterslip in time or in space. This suggests that using repeating events as a proxy for slip may be strongly misleading. However, this is the first study that truly undertakes the task of comparing geodetic slip with repeaters. As such, it is critical to repeat this procedure at other faults to either confirm these findings or establish that this system is an outlier. In either case, this work should be conducted urgently. Repeating earthquakes are being used to make maps of slip at subduction zones, like Japan (e.g. Ozawa et al. 2011), which have produced some of the most devastating earthquakes in recent memory. Incorrectly measuring the slip that is occurring there is a perilous undertaking, with potentially life threatening results depending on the applications of those studies.

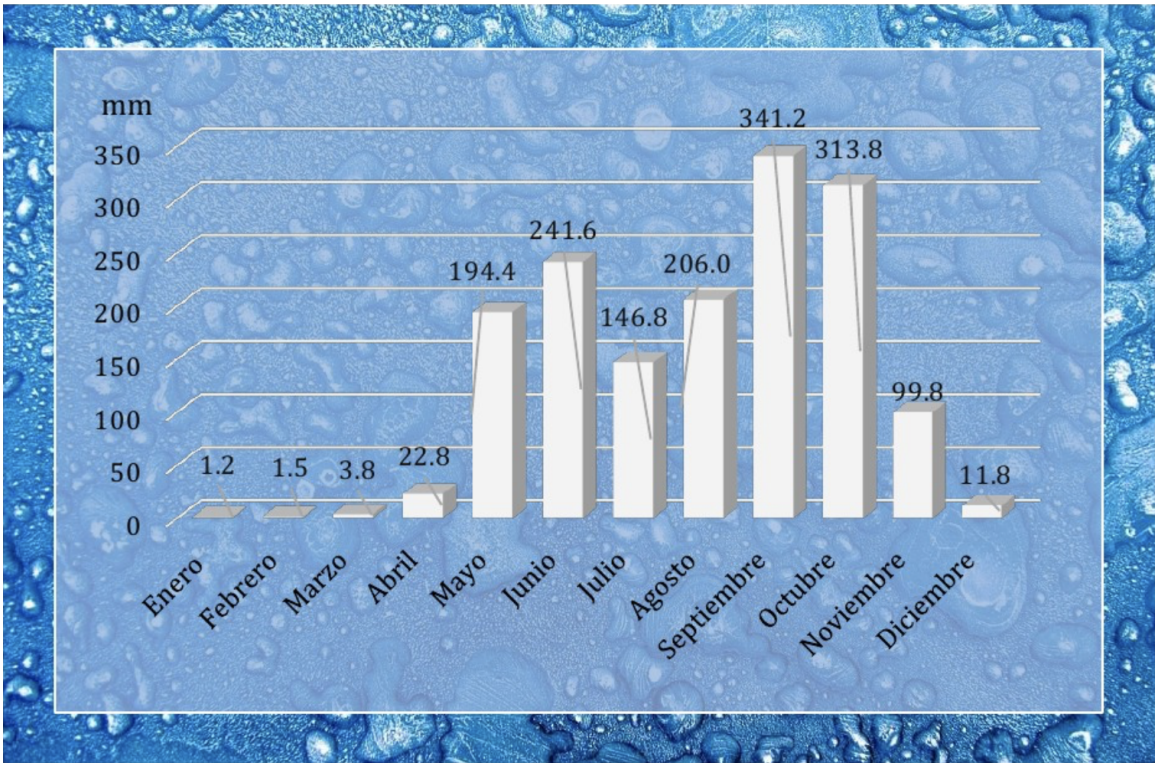

Figure 5.1: Figure from (Energía 2017). Average rainfall, by month, from 1957-2017 in Liberia, Costa Rica just inland of the Nicoya Peninsula (within the study area). Wet season extends from April to December. Two peaks in rainfall can be seen, with the second and higher peak resulting from the effect of Hurricane season. The period between the two peaks is referred to as the 'veranillo' or little summer.

Appendices

APPENDIX A

SUPPLEMENT TO CHAPTER 2: "LARGE AND PRIMARILY UPDIP AFTERSLIP FOLLOWING THE 2012 M_W 7.6 NICOYA, COSTA RICA EARTHQUAKE"

This supplement provides additional figures to support conclusions described in the main text of this article. Figures A.1 and A.2 contain results of alternate model inversions, both of which are similar to those presented in the article. They are provided here for completeness. Figure A.3 shows continuous GPS data for a station located off the Nicoya peninsula. While it does not contribute towards afterslip it does contain a clear signal from Slow Slip Events (SSEs) in 2014 and 2015.

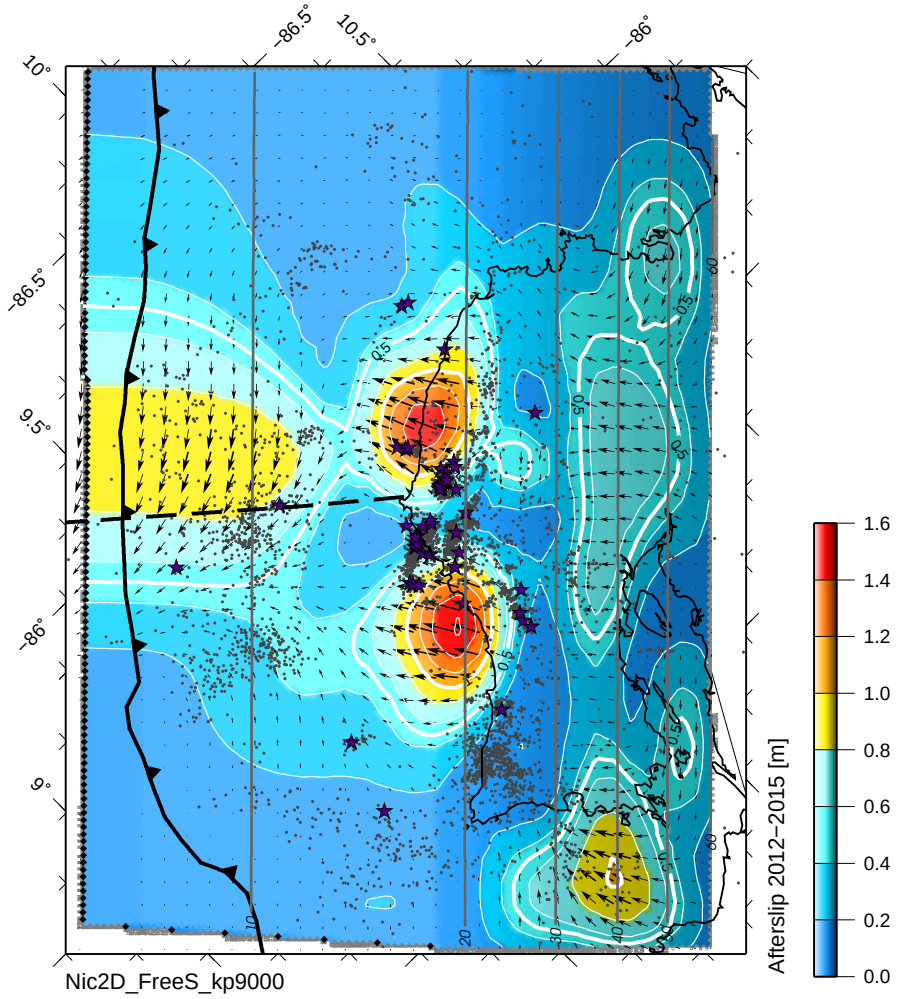

Figure A.1: Postseismic slip for 2D geometry of Nicoya subduction zone, allowing for slip at the trench (free surface). κ of 9000 is used for comparison against 3D models in main text. Interface geometry consistent with Feng et al. (2012) and Protti et al. (2014). Magnitude of slip scaled by color, with arrows showing direction of hanging wall motion at each patch. Aftershocks until end of 2012 shown as grey dots, with purple stars representing locations of repeating aftershock clusters (Yao et al. 2017). Thick black line with teeth marks the Middle America Trench, while thin grey lines show depth in 10 km intervals. EPR-CNS suture shown as dashed line (Barckhausen et al. 2001). Comparing with Figure 2.7, there is little discrepancy between the simpler 2D geometry shown here and the full 3D model reported in the main text.

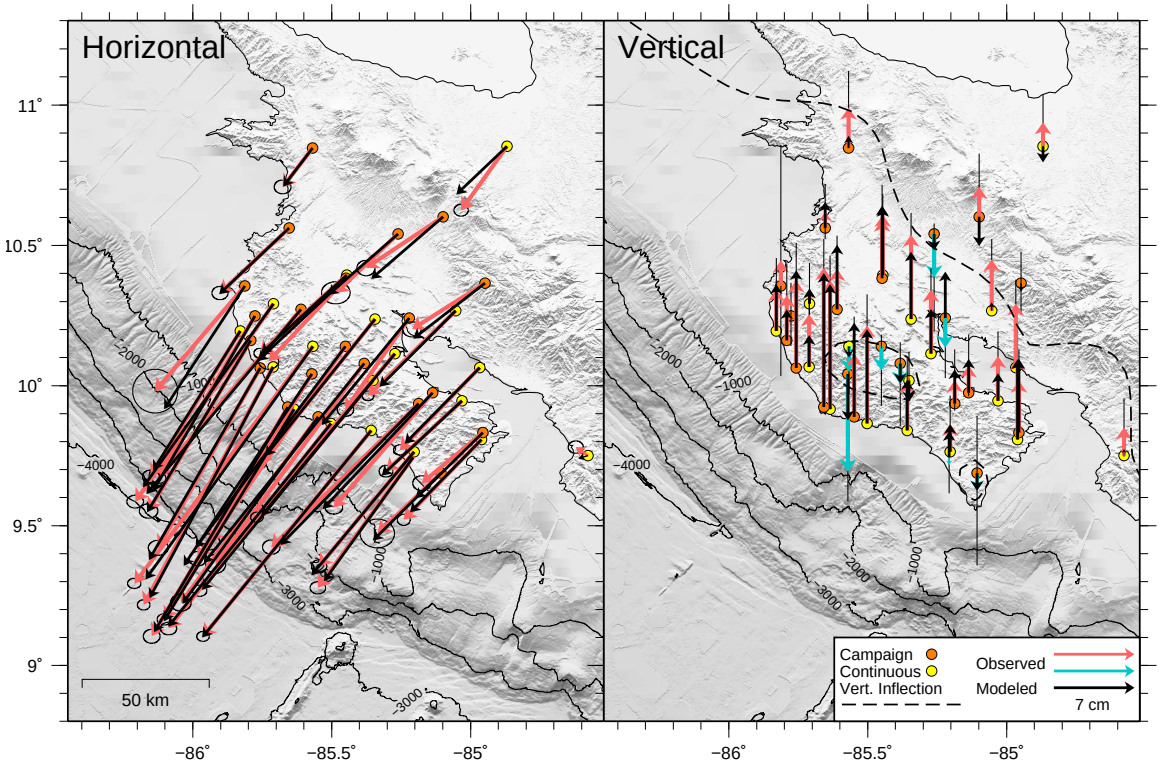

Figure A.2: GPS displacements for 2012-2015 time period, shown for comparison against model predictions for preferred slip result with fixed surface. Observations shown by colored arrows, with predictions indicated by black arrows. Left panel shows horizontal displacement, right shows vertical. Dashed line in right panel shows modeled zero vertical deformation, separating uplift from subsidence. Compare to Figure 2.8 of main text, showing same data compared to predicted vectors using non-fixed surface model. Results are almost identical, indicating that the data is unable to resolve between models with and without slip at the interface.

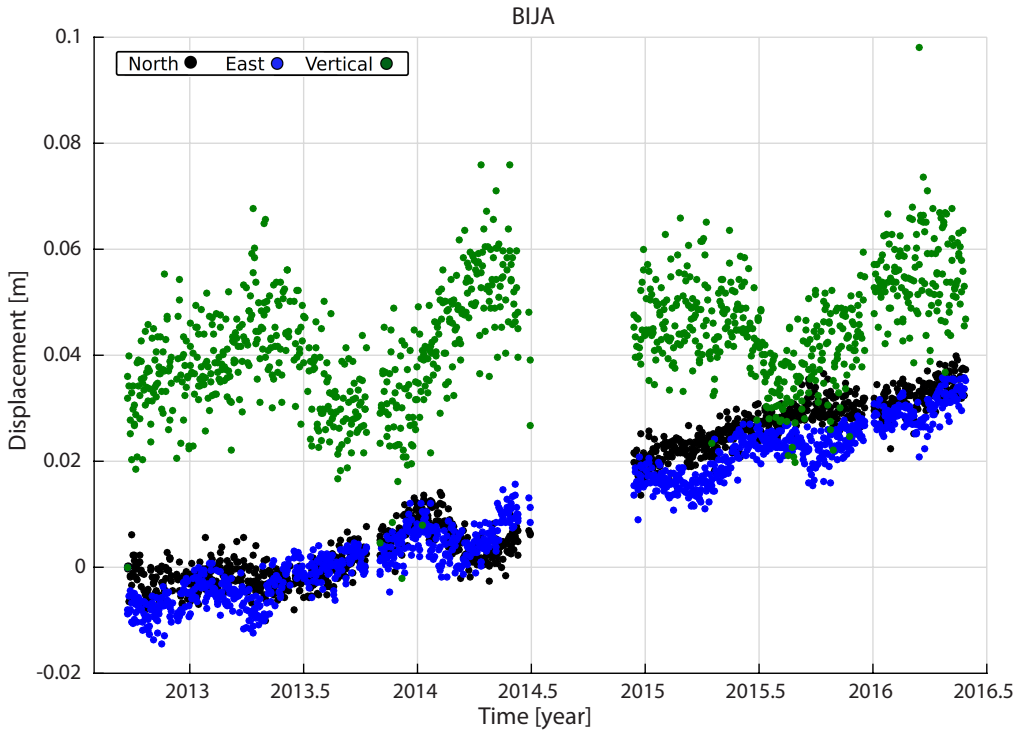

Figure A.3: Time series of GPS displacements for continuous station BIJA, located on the southeast side of the Gulf of Nicoya. This non-peninsula site does not display a strong post-seismic response, but the general northeast trend is interrupted in early 2014 by a southwest transient lasting up to one third of the year. As discussed in the main text, this matches observations at other stations surrounding the Gulf of Nicoya and points to a slow slip event in that region.

APPENDIX B

SUPPLEMENT TO CHAPTER 3: "ENIGMATIC UPPER-PLATE SLIVER TRANSPORT PAUSED BY MEGATHRUST EARTHQUAKE AND AFTERSLIP"

This supplement contains a movie of surface velocities throughout time, as well as figures and tables relating to the selection of high quality data and inversion results. A map of the study area is also provided. All data are described in text as well as figure captions. A dataset of GPS annual velocities used in this study is provided in Dataset S1.

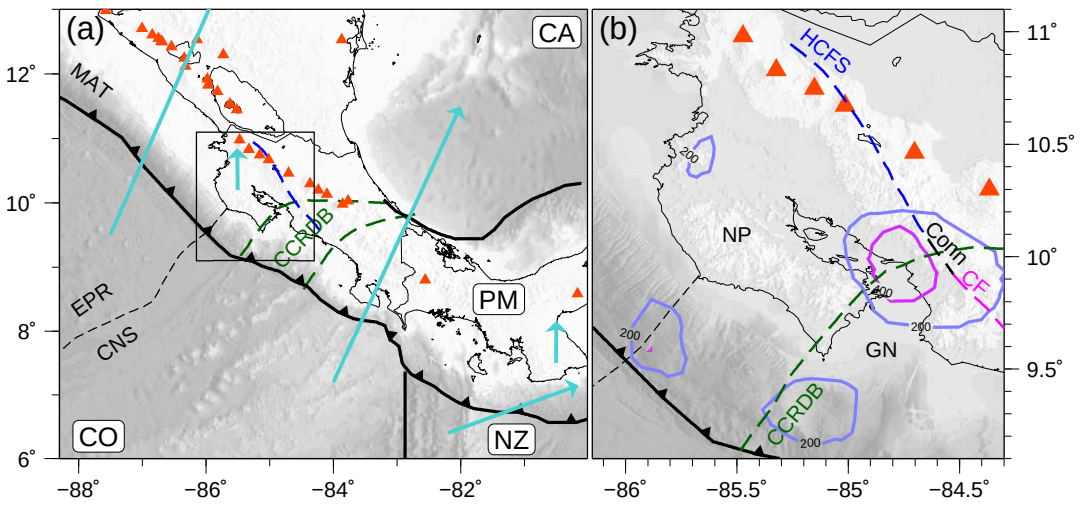

Figure B.1: Tectonic overview of the study area, wherein Cocos (CO) and Nazca (NZ) plates subduct beneath Caribbean (CA) plate and proposed Panama Microblock (PM) (Bird et al. 2002). Separation of crust sourced at the EPR and CNS Center is marked by thin dashed black line (Barckhausen et al. 2001). The Central Costa Rica Deformed Belt (CCRDB) is bounded by dashed green lines (Marshall, Fisher, and Gardner 2000). The Middle America Trench (MAT) is marked by a black line with triangles in the direction of subduction. Volcanoes shown as red triangles. Haciendas-Chiripa Fault System (HCFS) and potential Candelaria Fault connector are shown as blue dashed line (Kyriakopoulos and Newman 2016; Montero, Lewis, and Araya 2017). Plate motions are shown for stable Caribbean reference frame (DeMets, Gordon, and Argus 2010), indicated by cyan vectors. Seafloor bathymetry and crustal topography shaded in grey (Ryan et al. 2009). Country boundaries shown as thin black lines. (b) Zoomed in view of Nicoya study area. Nicoya peninsula (NP) and Gulf of Nicoya (GN) are labelled. Cumulative slip, in meters, from 2014 and 2015 slow slip events indicated by purple contours (Voss et al. 2017).

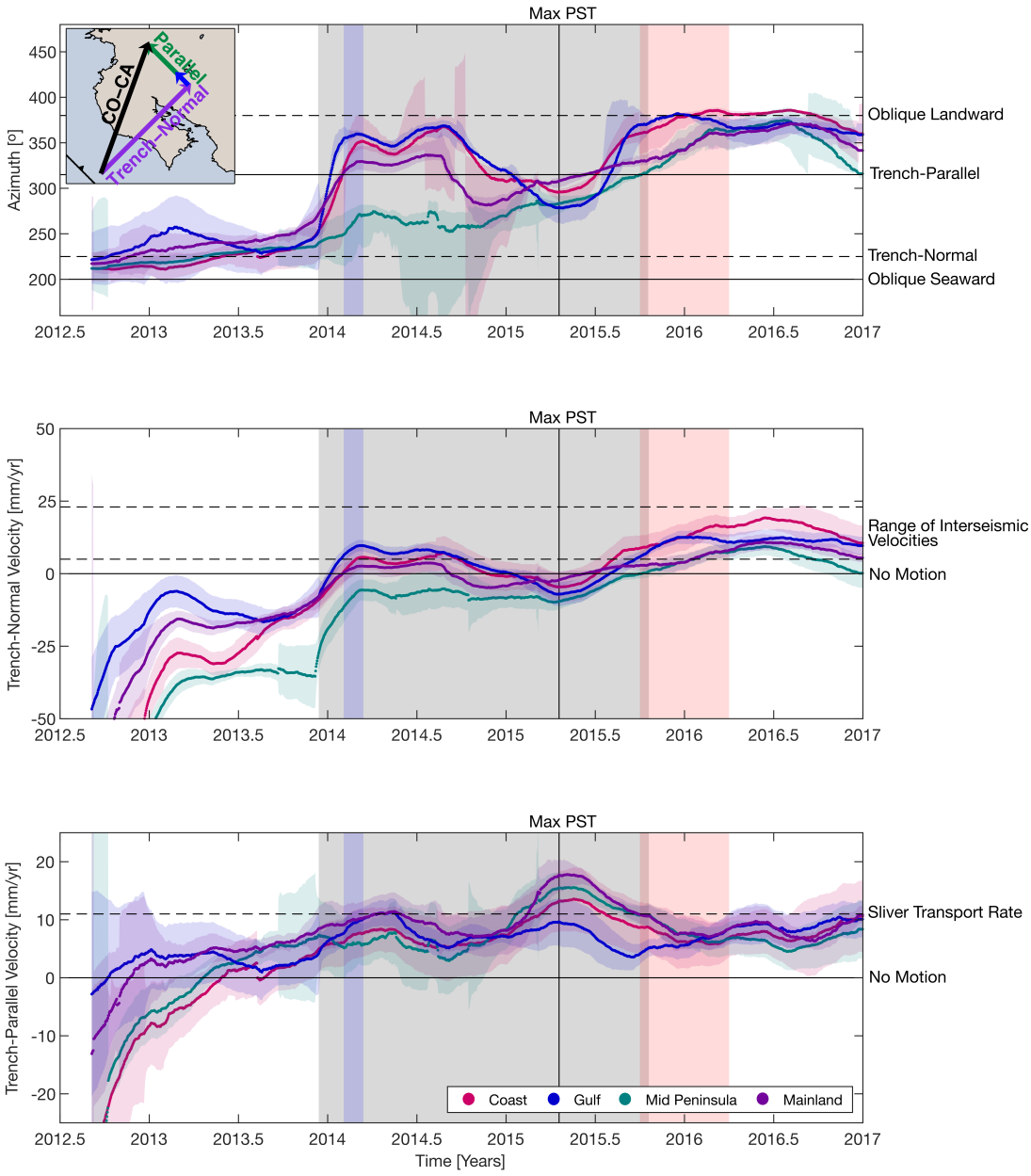

Figure B.2: Averaged azimuth, trench-normal velocities, and trench-parallel velocities, in stable Caribbean reference frame. Daily velocities, calculated over the following year, are the weighted average of individual GNSS stations grouped by location. Coastal stations in pink, mid peninsula stations in teal, mainland stations in purple, Gulf of Nicoya stations in blue (Table B.1). Standard deviations are shown as transparent regions. PST indicated by grey rectangle from 2013.95-2015.80. The 2014 and 2015 SSEs indicated by blue and red rectangles, respectively (Voss et al. 2017). For reference, azimuth of oblique seaward convergence, trench-normal, trench-parallel, and oblique landward convergence are plotted in the top panel and inset. The range of previously observed interseismic velocities is shown in the second panel, and the third shows the measured average sliver transport rate from the previous interseismic (Feng et al. 2012).

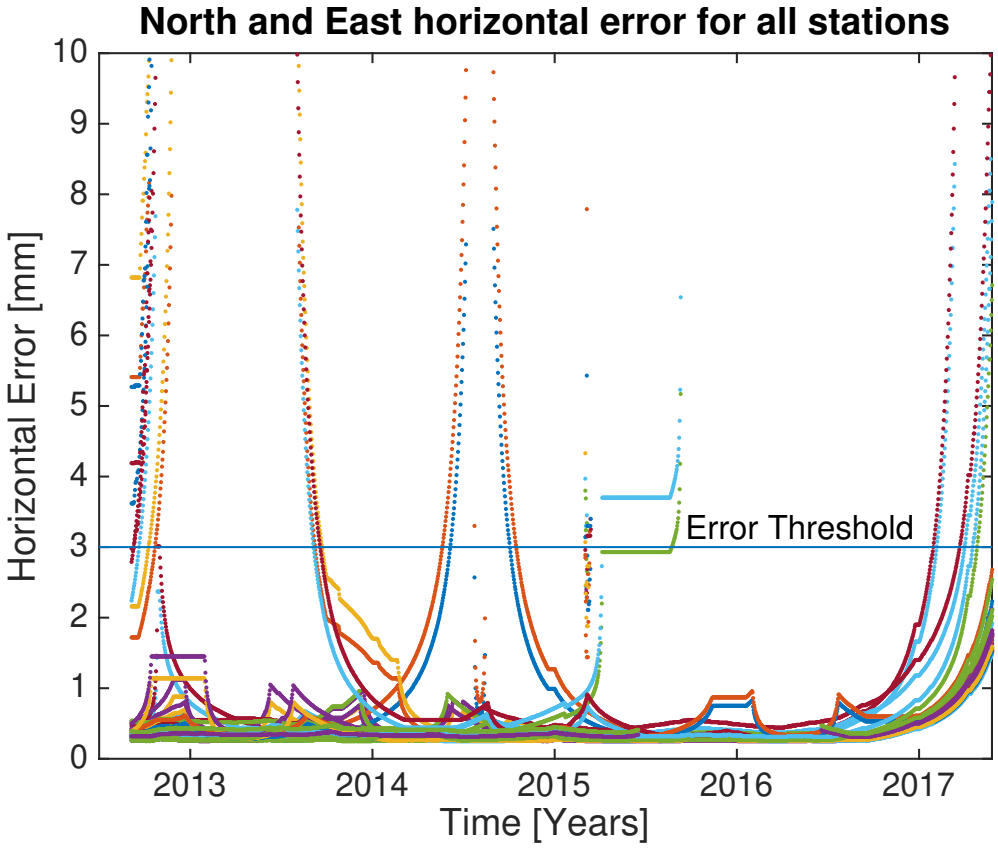

Figure B.3: North and East horizontal error [mm] for daily positions at all stations. Colors are randomly generated. Blue horizontal line represents the 3 mm error threshold used in this study. Clearly errors are largest near the start and end of data availability for any station, with a steep increase in error before and after data gaps. The threshold selected aims to preserve data from as many stations as possible while minimizing spurious datapoints.

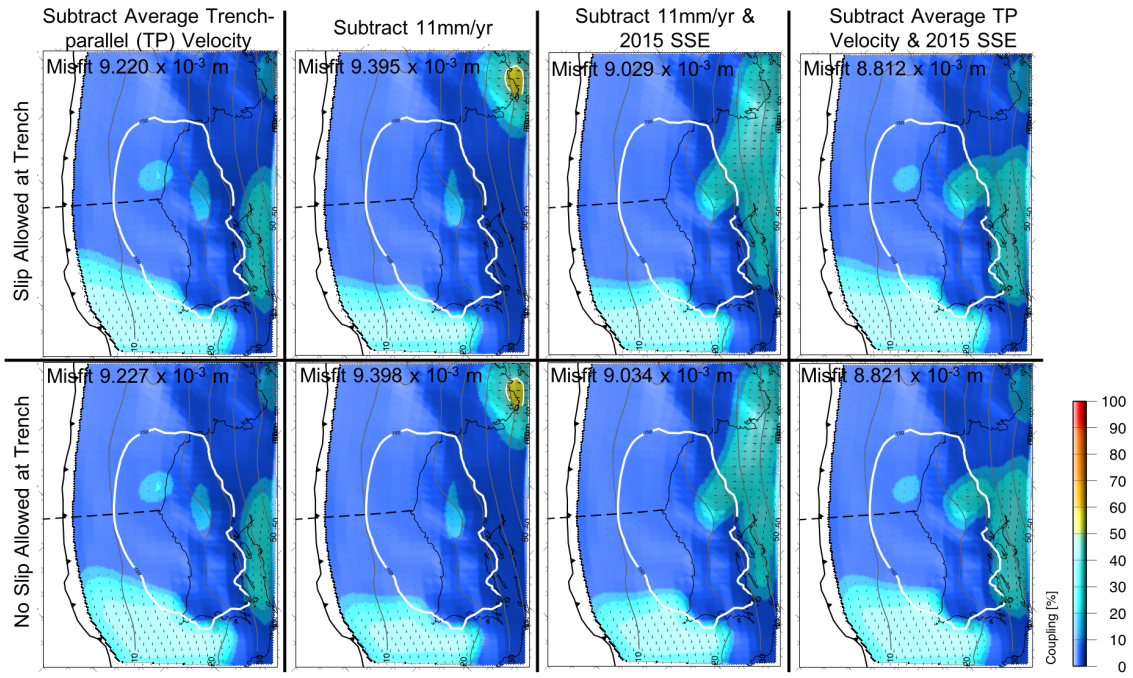

Figure B.4: Comparison of a sampling of different inversion strategies, all computed for the maximum PST time period starting at 2015.29 (green), for the same smoothing parameter. Leftmost column shows results presented in main text (Figure 3.2d), wherein the average trench-parallel velocity is subtracted prior to inversion. Far right column also subtracts the average trench-parallel motion. Center columns show the results if 11 mm/yr is subtracted instead, to represent the previously-recorded sliver transport rate (Feng et al. 2012). The two right columns shows the result where the contribution from the 2015 SSE (Voss et al. 2017) is also removed, for available stations. The top row shows the results when slip is allowed at the trench (free surface), while the bottom shows the same results where slip is set to zero at the free surface. Model misfit indicated at topleft of each panel. All results show less than 50% coupling anywhere inside the polygon of recoverability (thick white line), suggesting the results presented herein are not an artifact of the inversion strategy. The outcome is similar even with different assumptions about the rate of sliver motion and impact of slow slip event, as shown by the similar misfits. These do not constitute all possible inversions strategies, but rather are selected as a representative set to show that the key findings are the same irrespective of the inversion details.

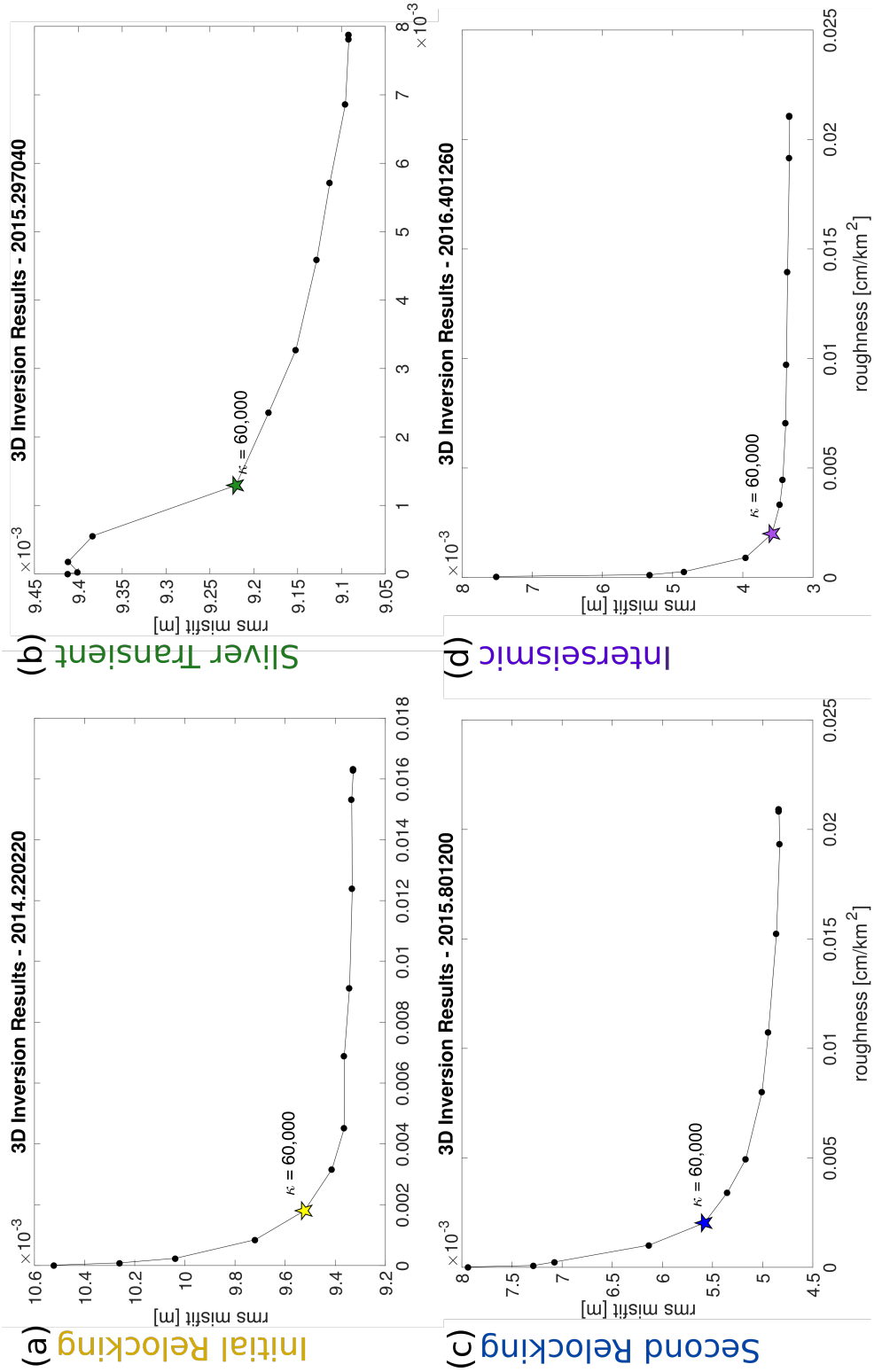

Figure B.5: L-curves of roughness versus misfit for backslip inversions at (a) 2014.22, (b) 2015.30, (c) 2015.80, and (d) 2016.40. Kappa (κ) of 60,000, indicated by stars, is selected to jointly minimize roughness and model misfit. Resulting backslips are shown in Figure 3.2.

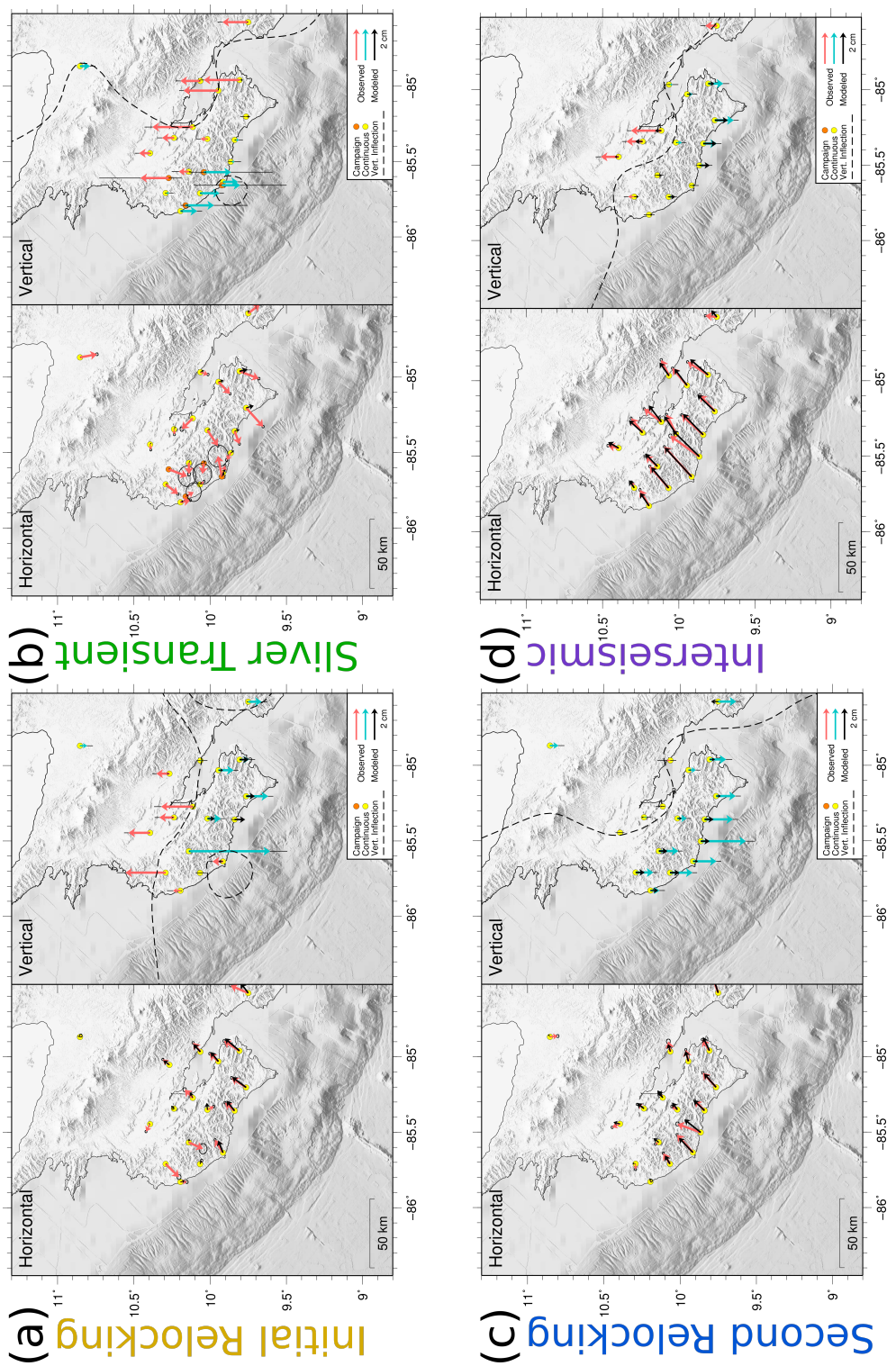

Figure B.6: Horizontal and vertical surface velocities at (a) initiation of PST, (b) maximum PST, (c) after PST completion, and (d) at the end of the study period. Observed GNSS velocities are shown in red/blue with 95% error ellipses, and velocities predicted by backslip model are shown as black vectors for horizontal components and dash-delimited zones of uplift/subsidence for the vertical.

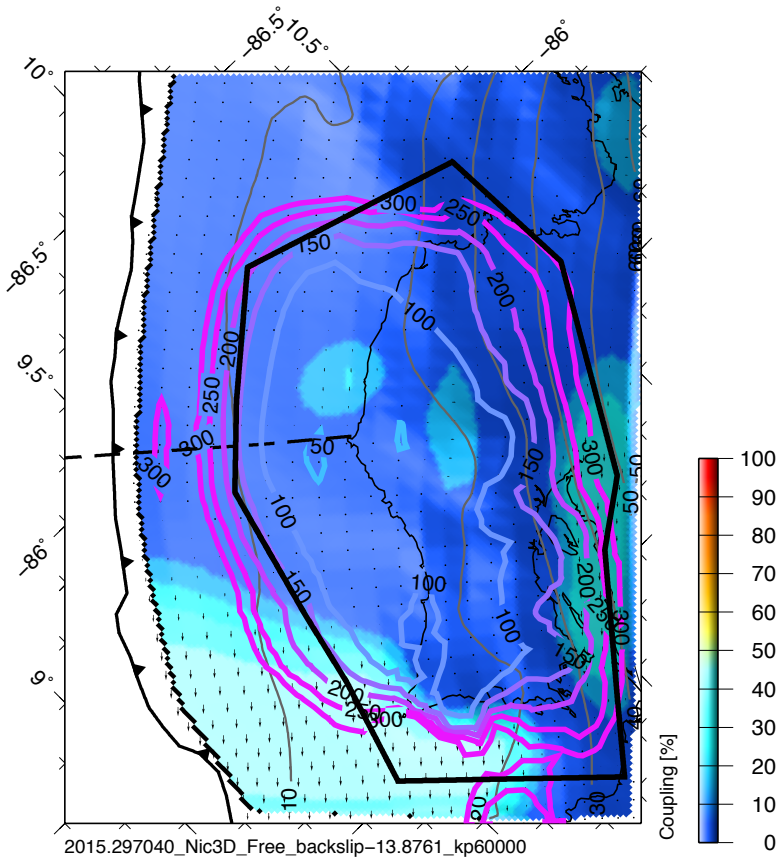

Figure B.7: Resolution spread parameter (defined in Menke (1989) and implemented in Kyriakopoulos et al. (2015) and Hobbs et al. (2017)), which demonstrates the distance over which the model is sensitive to data. Plotted over top of slip results for maximum PST (2015.30 – green) with average trench parallel motion subtracted (consistent with Figure 3.2b). A larger spread means the model is sensitive to data over a larger area. Thus, the areas over which the model is sensitive only to nearby data are the areas over which the model has better recoverability. We select the 150 km contour for plotting for the 16 stations used in this study, with a smoothing parameter (κ) of 60,000. For comparison, the thick black line shows the polygon of recoverability corresponding to resolution spread of 20-25 km from Hobbs et al. (2017), which used a smoothing parameter of 9,000 and 40 stations. Despite showing roughly the same shape, resolution is diminished both by the reduced number of stations and the high level of smoothing. The resolution spread parameter is strongly affected by the smoothing, such that the relatively large smoothing implemented in this study (Figure B.4) results in a relatively large resolution spread even though our data are still able to constrain slip in the area near the Nicoya Peninsula and immediately offshore.

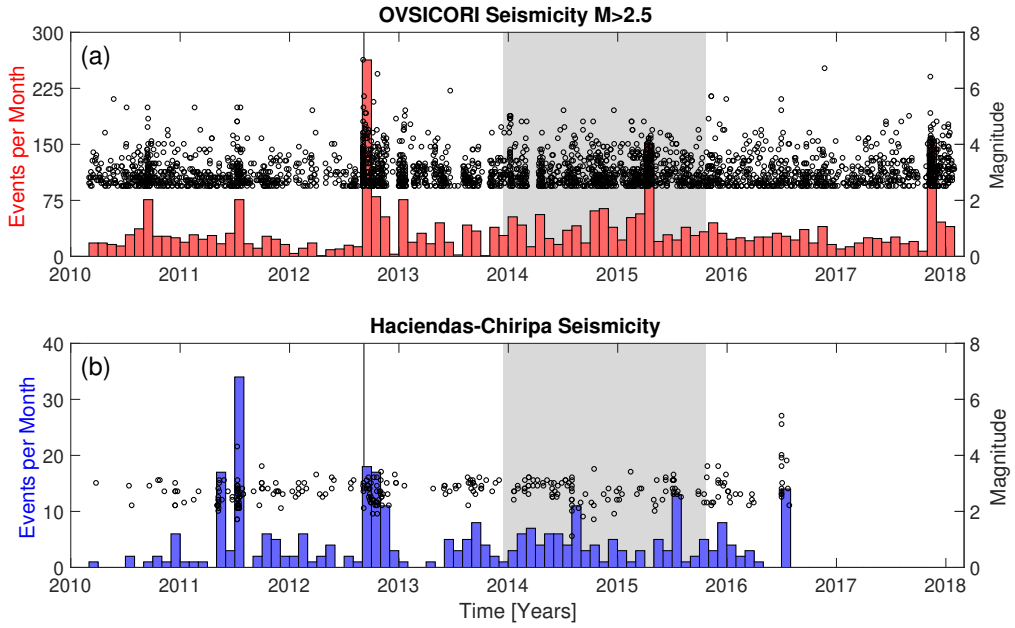

Figure B.8: Number of recorded earthquakes (bar) and their magnitudes (circle) for the (a) OVSICORI network and (b) Haciendas-Chiripa catalogue (Montero, Lewis, and Araya 2017). A M_C of $M_L \geq 2.5$ is selected from the full OVSICORI catalog. Black vertical line shows timing of the 2012 M_w 7.6 Nicoya earthquake. PST shown by grey rectangle, during which time no clear change in seismicity is observed.

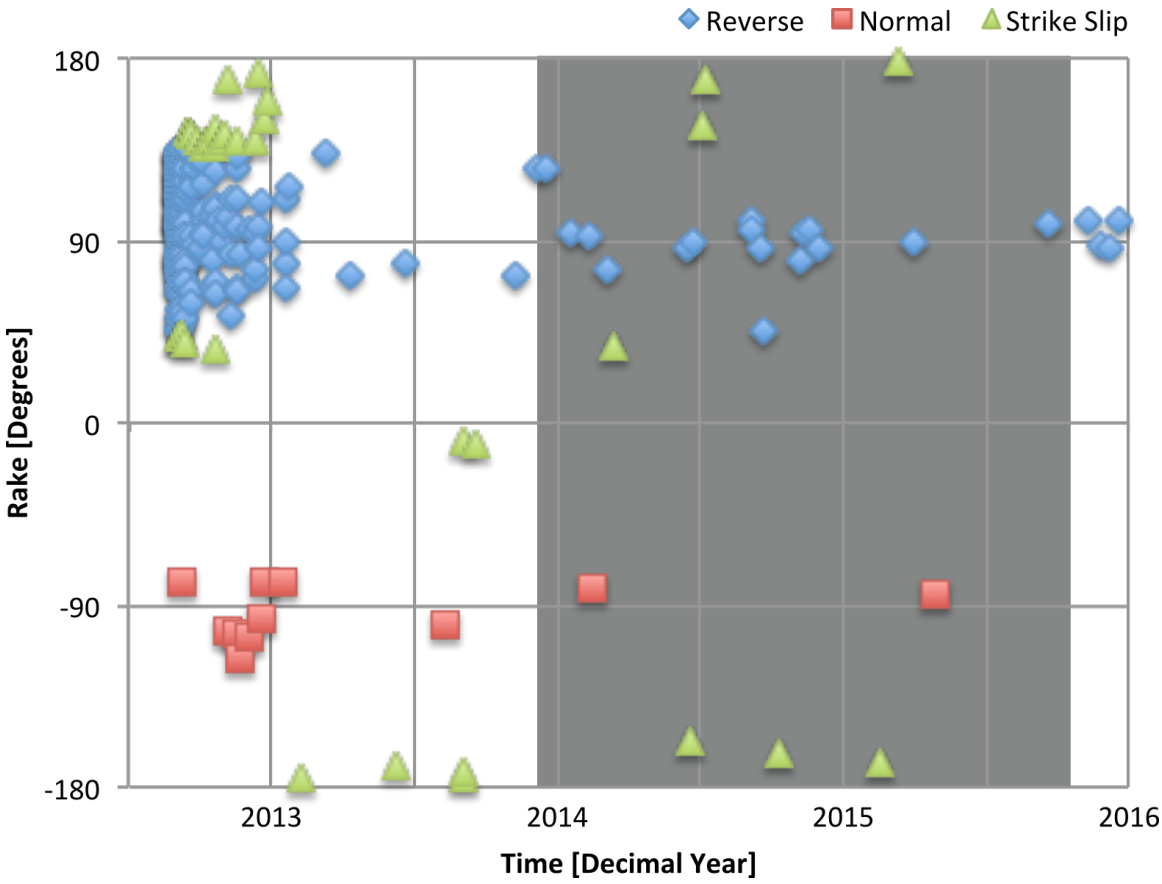

Figure B.9: Focal mechanisms for nearby events following the 2012 Nicoya mainshock (Chaves et al. 2017). Temporal evolution shows no discernable aberration during the PST (2013.95-2015.80).

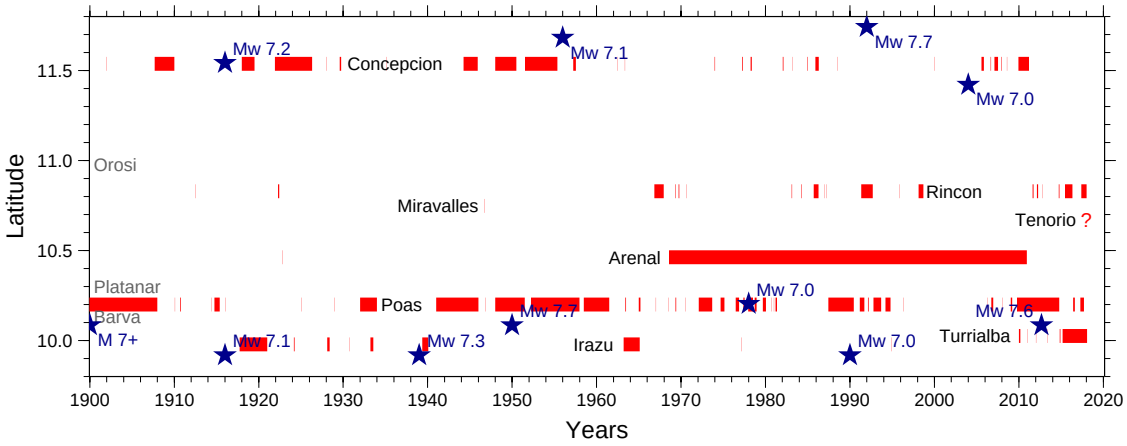

Figure B.10: Eruptions of volcanoes in study area (Fig B.1b) through the 20th century, as recorded by the Global Volcanism Program database. Volcano names are plotted at their latitude, with grey text indicating a volcano that did not erupt over the time period considered. Superimposed are megathrust earthquakes $M_w \geq 7.0$. Non-eruptive activites such as seismic swarms and fumarolic activity are not indicated here.

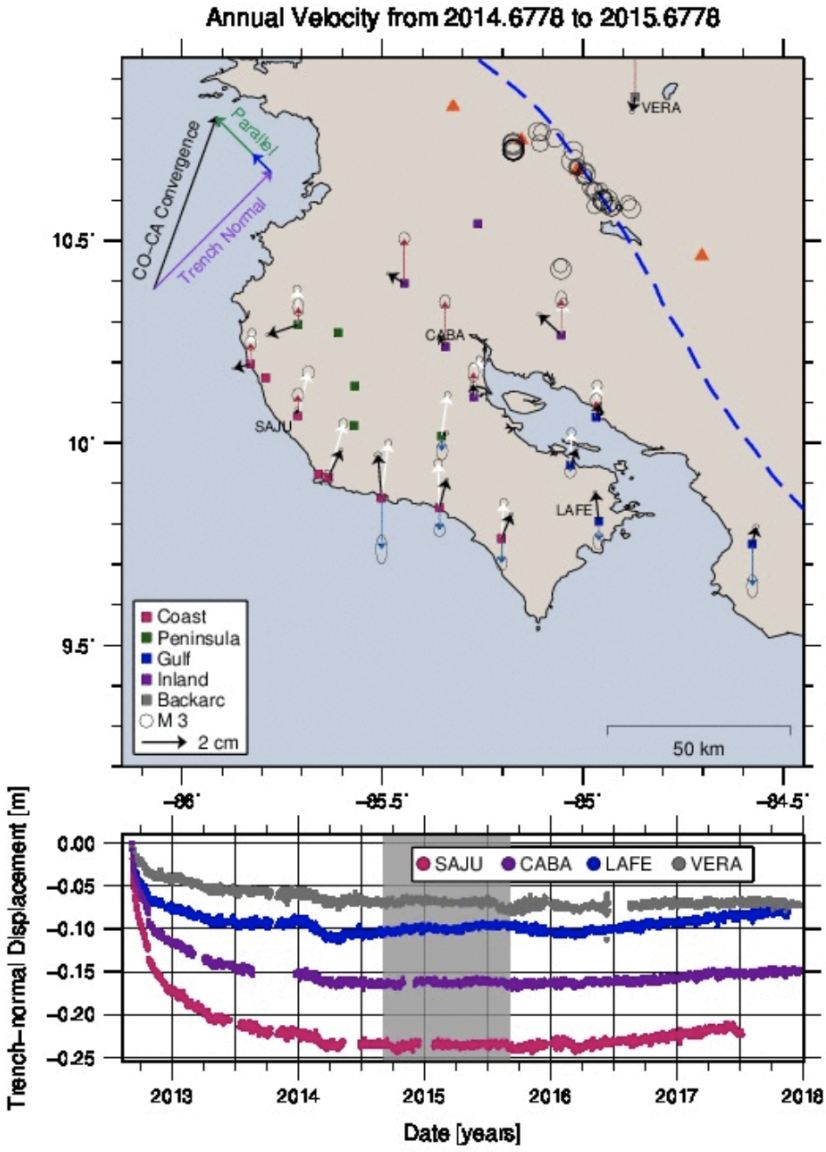

Figure B.11: Full movie can be found at `http://geophysics.eas.gatech.edu/people/thobbs/outputs/oneyear_vels_2018.gif` — above is only a still representation. Velocities, through time, at all available GNSS stations. Immediately after the 2012 mainshock velocities are large and seaward, diminishing through late 2013. Velocities are then seen to point NW, for a period of pure sliver transport in 2014 and 2015. Following this, velocities rotate landward, starting at coastal sites, to resume oblique, interseismic motions. Interseismic results of (Feng et al. 2012) shown in white. Convergence vector and its trench-normal, trench-parallel, and sliver motion components indicated in black, purple, green, and blue arrows, respectively (DeMets, Gordon, and Argus 2010). (b) Raw northward displacements (ITRF2008 reference) for selected stations, labeled in (a). Coastal stations shown in pink, Gulf of Nicoya stations in blue, and backarc station in teal. All other stations, on and around the peninsula, in purple.

Table B.1: All stations used in this study. Information is provided about the location, operating mode, number of days of data used, and regional grouping of each station.

Station	Longitude	Latitude	Mode	Days	Group
BAGA	-85.2612	10.5414	Campaign	4	Mainland
BIJA	-84.5769	9.74997	Continuous	1578	Gulf
BON2	-85.2025	9.76453	Continuous	1578	Coast
CABA	-85.3435	10.2379	Continuous	1578	Mainland
DIRI	-85.6106	10.2718	Campaign	2	Peninsula
ELVI	-85.4458	10.3947	Continuous	1573	Mainland
EPZA	-85.5681	10.1409	Continuous	1451	Peninsula
GRZA	-85.6356	9.91552	Continuous	1578	Coast
GUIO	-85.6585	9.92305	Campaign	4	Coast
HATI	-85.7101	10.2922	Continuous	1196	Peninsula
HUA2	-85.3517	10.0177	Continuous	1578	Peninsula
IND1	-85.5022	9.86462	Continuous	1212	Coast
LAFE	-84.9603	9.80706	Continuous	1578	Gulf
LEPA	-85.0312	9.94537	Continuous	1578	Gulf
LMNL	-85.0533	10.2675	Continuous	943	Mainland
MIRM	-85.5711	10.0421	Campaign	42	Peninsula
PNE2	-85.8287	10.1951	Continuous	1578	Coast
PUJE	-85.2725	10.1140	Continuous	1205	Mainland
PUMO	-84.9667	10.0645	Continuous	1578	Gulf
QSEC	-85.3573	9.84038	Continuous	1578	Coast
SAJU	-85.7106	10.0671	Continuous	1578	Coast
VENA	-85.7917	10.1611	Campaign	6	Coast
VERA	-84.8690	10.8536	Continuous	1212	BackArc

Table B.2: Average trench-parallel velocities across network for 6 representative times described in text and illustrated in Figures 3.1, 3.2, B.3, and B.4.

Date	**Date**	**Label**	**Average TP Velocity**	**Standard Deviation**
Decimal Year	YYYY MM DD		mm/yr	mm/yr
2013.000920	2013 01 01	Strong Afterslip	-2.5108	7.5742
2013.951700	2013 12 14	Afterslip	5.6685	4.5386
2014.220220	2014 03 22	Initial PST	8.8275	3.2443
2015.297040	2015 04 19	Maximum PST	13.8761	5.5283
2015.801200	2015 10 20	End PST	8.7173	3.5127
2016.401260	2016 05 26	Interseismic	8.4057	3.2334

Dataset S1 is a compressed folder of all velocity vector fields used in this study. Each file in the folder is named as"DECIMALYEAR_rneu_vels-CA.out", and has headers: Station Name ".rneu", Start Time [decimal year], End Time [decimal year], 0, Longitude [^{o}], Latitude [^{o}], Elevation [m], North Velocity [m], East Velocity [m], Upward Velocity [m], North Uncertainty [m], East Uncertainty [m], Upwards Uncertainty [m], Number of Data Points, 0, East Caribbean Velocity [mm/yr], North Caribbean Velocity [mm/yr], East Velocity in Stable Caribbean Reference Frame [m], North Velocity in Stable Caribbean Reference Frame [m]. Details described in Section 3.4.1.

REFERENCES

Audet, Pascal and Susan Y Schwartz (2013). "Hydrologic control of forearc strength and seismicity in the Costa Rican subduction zone". In: *Nature Geoscience* 6.10, p. 852.

Barbot, Sylvain, Yuri Fialko, and Yehuda Bock (2009). "Postseismic deformation due to the Mw 6.0 2004 Parkfield earthquake: Stress-driven creep on a fault with spatially variable rate-and-state friction parameters". In: *Journal of Geophysical Research: Solid Earth* 114.B7.

Barckhausen, Udo, Hans A Roeser, and Roland Huene (1998). "Magnetic signature of upper plate structures and subducting seamounts at the convergent margin off Costa Rica". In: *Journal of Geophysical Research: Solid Earth* 103.B4, pp. 7079–7093.

Barckhausen, Udo et al. (2001). "Revised tectonic boundaries in the Cocos Plate off Costa Rica: Implications for the segmentation of the convergent margin and for plate tectonic models". In: *Journal of Geophysical Research: Solid Earth* 106.B9, pp. 19207–19220.

Bedford, Jonathan et al. (2016). "Separating rapid relocking, afterslip, and viscoelastic relaxation: An application of the postseismic straightening method to the Maule 2010 cGPS". In: *Journal of Geophysical Research: Solid Earth* 121.10, pp. 7618–7638.

Beeler, NM, DL Lockner, and SH Hickman (2001). "A simple stick-slip and creep-slip model for repeating earthquakes and its implication for microearthquakes at Parkfield". In: *Bulletin of the Seismological Society of America* 91.6, pp. 1797–1804.

Ben-Zion, Yehuda and Lupei Zhu (2002). "Potency-magnitude scaling relations for southern California earthquakes with 1.0¡ M L¡ 7.0". In: *Geophysical journal international* 148.3, F1–F5.

Ben-Zion, Yehuda et al. (2003). "Key formulas in earthquake seismology". In: *International handbook of earthquake and engineering seismology* 81.

Beroza, Gregory C and Satoshi Ide (2011). "Slow earthquakes and nonvolcanic tremor". In: *Annual review of Earth and planetary sciences* 39, pp. 271–296.

Bevis, Michael and Stephen J Martel (2001). "Oblique plate convergence and interseismic strain accumulation". In: *Geochemistry, Geophysics, Geosystems* 2.8.

Biggs, Juliet et al. (2010). "Magma flux at Okmok Volcano, Alaska, from a joint inversion of continuous GPS, campaign GPS, and interferometric synthetic aperture radar". In: *Journal of Geophysical Research: Solid Earth* 115.B12.

Bilek, Susan L and Thorne Lay (2018). “Subduction zone megathrust earthquakes”. In: *Geosphere* 14.4, pp. 1468–1500.

Bilich, Andria, John F Cassidy, and Kristine M Larson (2008). “GPS Seismology: Application to the 2002 M W 7.9 Denali fault earthquake”. In: *Bulletin of the Seismological Society of America* 98.2, pp. 593–606.

Bird, Peter et al. (2002). “Plate tectonics and earthquake potential of spreading ridges and oceanic transform faults”. In:

Blewitt, Geoffrey (2008). “Fixed point theorems of GPS carrier phase ambiguity resolution and their application to massive network processing: Ambizap”. In: *Journal of Geophysical Research: Solid Earth* 113.B12.

Bourgois, Jacques et al. (1984). “The geologic history of the Caribbean-Cocos plate boundary with special reference to the Nicoya ophiolite complex (Costa Rica) and DSDP results (Legs 67 and 84 off Guatemala): A synthesis”. In: *Tectonophysics* 108.1-2, pp. 1–32.

Bürgmann, Roland and Georg Dresen (2008). “Rheology of the lower crust and upper mantle: Evidence from rock mechanics, geodesy, and field observations”. In: *Annual Review of Earth and Planetary Sciences* 36.

Cao, Aimin and Stephen S Gao (2002). “Temporal variation of seismic b-values beneath northeastern Japan island arc”. In: *Geophysical research letters* 29.9, pp. 48–1.

Chacón-Barrantes, Silvia E and Marino Protti (2011). “Modeling a tsunami from the Nicoya, Costa Rica, seismic gap and its potential impact in Puntarenas”. In: *Journal of South American Earth Sciences* 31.4, pp. 372–382.

Chan, Chung-Han and Ross S Stein (2009). “Stress evolution following the 1999 Chi-Chi, Taiwan, earthquake: consequences for afterslip, relaxation, aftershocks and departures from Omori decay”. In: *Geophysical Journal International* 177.1, pp. 179–192.

Chaves, Esteban J and Susan Y Schwartz (2016). “Monitoring transient changes within overpressured regions of subduction zones using ambient seismic noise”. In: *Science Advances* 2.1, e1501289.

Chaves, Esteban J et al. (2017). “Aftershocks of the 2012 M w 7.6 Nicoya, Costa Rica, earthquake and mechanics of the plate interface”. In: *Bulletin of the Seismological Society of America* 107.3, pp. 1227–1239.

Chen, Ting and Nadia Lapusta (2009). “Scaling of small repeating earthquakes explained by interaction of seismic and aseismic slip in a rate and state fault model”. In: *Journal of Geophysical Research: Solid Earth* 114.B1.

Chen, Ting et al. (2009). "Slip distribution from the 1 April 2007 Solomon Islands earthquake: A unique image of near-trench rupture". In: *Geophysical Research Letters* 36.16.

Chester, Frederick M et al. (2013). "Structure and composition of the plate-boundary slip zone for the 2011 Tohoku-Oki earthquake". In: *Science* 342.6163, pp. 1208–1211.

Cleveland, K Michael, Thomas F VanDeMark, and Charles J Ammon (2015). "Precise relative locations for earthquakes in the northeast Pacific region". In: *Journal of Geophysical Research: Solid Earth* 120.10, pp. 6960–6976.

ComCat, USGS (2012a). *M6.5 - Costa Rica*. `http://earthquake.usgs.gov/earthquakes/eventpage/usp000jucg#scientific_summary`. [Online; last accessed 22 Feb 2016].

ComCat, USGS (2012b). *M7.6 - Costa Rica*. `http://earthquake.usgs.gov/earthquakes/eventpage/usp000jrsw#scientific_summary`. [Online; last accessed 22 Feb 2016].

Cyranoski, David (2011). *Japan faces up to failure of its earthquake preparations*.

Daniell, James E et al. (2011). "The CATDAT damaging earthquakes database". In: *Natural hazards and earth system sciences* 11.8, pp. 2235–2251.

Davis, Earl E, Heinrich Villinger, and Tianhaozhe Sun (2015). "Slow and delayed deformation and uplift of the outermost subduction prism following ETS and seismogenic slip events beneath Nicoya Peninsula, Costa Rica". In: *Earth and Planetary Science Letters* 410, pp. 117–127.

De Gori, Pasquale et al. (2012). "Heterogeneities along the 2009 L'Aquila normal fault inferred by the b-value distribution". In: *Geophysical Research Letters* 39.15.

DeMets, Charles, Richard G Gordon, and Donald F Argus (2010). "Geologically current plate motions". In: *Geophysical Journal International* 181.1, pp. 1–80.

DeShon, Heather R et al. (2006). "Seismogenic zone structure beneath the Nicoya Peninsula, Costa Rica, from three-dimensional local earthquake P-and S-wave tomography". In: *Geophysical Journal International* 164.1, pp. 109–124.

Dieterich, James H (1972). "Time-dependent friction in rocks". In: *Journal of Geophysical Research* 77.20, pp. 3690–3697.

Dinc, A Nilay et al. (2010). "Local earthquake tomography of central Costa Rica: transition from seamount to ridge subduction". In: *Geophysical Journal International* 183.1, pp. 286–302.

Dixon, Timothy H et al. (2013). “Detailed data available for recent Costa Rica earthquake”. In: *Eos, Transactions American Geophysical Union* 94.2, pp. 17–18.

Dixon, Timothy H et al. (2014). “Earthquake and tsunami forecasts: Relation of slow slip events to subsequent earthquake rupture”. In: *Proceedings of the National Academy of Sciences* 111.48, pp. 17039–17044.

Dominguez, Luis A, Taka’aki Taira, and Miguel A Santoyo (2016). “Spatiotemporal variations of characteristic repeating earthquake sequences along the Middle America Trench in Mexico”. In: *Journal of Geophysical Research: Solid Earth* 121.12, pp. 8855–8870.

Dragert, Herb, Kelin Wang, and Thomas S James (2001). “A silent slip event on the deeper Cascadia subduction interface”. In: *Science* 292.5521, pp. 1525–1528.

Ekström, Göran, Meredith Nettles, and AM Dziewoński (2012). “The global CMT project 2004–2010: Centroid-moment tensors for 13,017 earthquakes”. In: *Physics of the Earth and Planetary Interiors* 200, pp. 1–9.

Energía, Ministerio de Ambiente y (2001). *Clima en Costa Rica — Pacífico Norte*. Tech. rep. Instituto Meteorológico Nacional, Departamento de Climatalogía e Investigaciones Aplicadas.

Energía, Ministerio de Ambiente y (2017). *Descripción del Clima Cantón de Liberia*. Tech. rep. Instituto Meteorológico Nacional, Departamento de Climatalogía e Investigaciones Aplicadas.

Feng, Lujia et al. (2012). “Active deformation near the Nicoya Peninsula, northwestern Costa Rica, between 1996 and 2010: Interseismic megathrust coupling”. In: *Journal of Geophysical Research: Solid Earth* 117.B6.

Fisher, Andrew T et al. (2003). “Abrupt thermal transition reveals hydrothermal boundary and role of seamounts within the Cocos Plate”. In: *Geophysical Research Letters* 30.11.

Freed, Andrew M (2005). “Earthquake triggering by static, dynamic, and postseismic stress transfer”. In: *Annu. Rev. Earth Planet. Sci.* 33, pp. 335–367.

Freed, Andrew M (2007). “Afterslip (and only afterslip) following the 2004 Parkfield, California, earthquake”. In: *Geophysical Research Letters* 34.6.

Fujii, Yushiro et al. (2011). “Tsunami source of the 2011 off the Pacific coast of Tohoku Earthquake”. In: *Earth, planets and space* 63.7, p. 55.

Funning, Gareth J et al. (2005). “Surface displacements and source parameters of the 2003 Bam (Iran) earthquake from Envisat advanced synthetic aperture radar imagery”. In: *Journal of Geophysical Research: Solid Earth* 110.B9.

Geist, Eric L, Vasily V Titov, and Costas E Synolakis (2006). "Tsunami: wave of change". In: *Scientific American* 294.1, pp. 56–63.

Ghosh, Abhijit et al. (2008). "Interface locking along the subduction megathrust from b-value mapping near Nicoya Peninsula, Costa Rica". In: *Geophysical Research Letters* 35.1.

Gubbins, David (2004). *Time series analysis and inverse theory for geophysicists*. Cambridge University Press.

Gutenberg, Beno and Charles F Richter (1944). "Frequency of earthquakes in California". In: *Bulletin of the Seismological Society of America* 34.4, pp. 185–188.

Harris, Robert N and Kelin Wang (2002). "Thermal models of the middle America trench at the Nicoya Peninsula, Costa Rica". In: *Geophysical Research Letters* 29.21, pp. 6–1.

Harris, Robert N et al. (2010). "Thermal regime of the Costa Rican convergent margin: 2. Thermal models of the shallow Middle America subduction zone offshore Costa Rica". In: *Geochemistry, Geophysics, Geosystems* 11.12.

Heidbach, Oliver et al. (2018). "The World Stress Map database release 2016: Crustal stress pattern across scales". In: *Tectonophysics* 744, pp. 484–498.

Helmstetter, Agnes and Bruce E Shaw (2009). "Afterslip and aftershocks in the rate-and-state friction law". In: *Journal of Geophysical Research: Solid Earth* 114.B1.

Hobbs, TE et al. (2017). "Large and primarily updip afterslip following the 2012 Mw 7.6 Nicoya, Costa Rica, earthquake". In: *Journal of Geophysical Research: Solid Earth* 122.7, pp. 5712–5728.

Holzer, Thomas L and James C Savage (2013). "Global earthquake fatalities and population". In: *Earthquake Spectra* 29.1, pp. 155–175.

Hsu, Ya-Ju et al. (2006). "Frictional afterslip following the 2005 Nias-Simeulue earthquake, Sumatra". In: *Science* 312.5782, pp. 1921–1926.

Hu, Y et al. (2004). "Three-dimensional viscoelastic finite element model for postseismic deformation of the great 1960 Chile earthquake". In: *Journal of Geophysical Research: Solid Earth* 109.B12.

Hu, Yan et al. (2016). "Stress-driven relaxation of heterogeneous upper mantle and time-dependent afterslip following the 2011 Tohoku earthquake". In: *Journal of Geophysical Research: Solid Earth* 121.1, pp. 385–411.

Huang, Hui et al. (2017). “Early aftershocks and afterslip surrounding the 2015 Mw 8.4 Illapel rupture”. In: *Earth and Planetary Science Letters* 457, pp. 282–291.

Husen, S, E Kissling, and R Quintero (2002). “Tomographic evidence for a subducted seamount beneath the Gulf of Nicoya, Costa Rica: The cause of the 1990 Mw= 7.0 Gulf of Nicoya earthquake”. In: *Geophysical Research Letters* 29.8, pp. 79–1.

Hutnak, M et al. (2007). “The thermal state of 18–24 Ma upper lithosphere subducting below the Nicoya Peninsula, northern Costa Rica margin”. In: *The Seismogenic Zone of Subduction Thrust Faults*, pp. 86–122.

Ide, Satoshi, Annemarie Baltay, and Gregory C Beroza (2011). “Shallow dynamic overshoot and energetic deep rupture in the 2011 Mw 9.0 Tohoku-Oki earthquake”. In: *Science* 332.6036, pp. 1426–1429.

Igarashi, Toshihiro, Toru Matsuzawa, and Akira Hasegawa (2003). “Repeating earthquakes and interplate aseismic slip in the northeastern Japan subduction zone”. In: *Journal of Geophysical Research: Solid Earth* 108.B5.

Ihmlé, Pierre F (1996). “Monte Carlo slip inversion in the frequency domain: Application to the 1992 Nicaragua Slow Earthquake”. In: *Geophysical research letters* 23.9, pp. 913–916.

Iinuma, Takeshi et al. (2004). “Inter-plate coupling in the Nicoya Peninsula, Costa Rica, as deduced from a trans-peninsula GPS experiment”. In: *Earth and Planetary Science Letters* 223.1-2, pp. 203–212.

Indonesia, Statistics (2011). “Population of Indonesia by Province 1971, 1980, 1990, 1995, 2000 and 2010”. In:

International Seismological Centre (2014). *International Seismological Centre On-line Bulletin*. data retrieved from `http://www.isc.ac.uk`.

Ishibe, Takeo et al. (2017). “Testing the Coulomb stress triggering hypothesis for three recent megathrust earthquakes”. In: *Geoscience Letters* 4.1, p. 5.

Ito, Takeo et al. (2016). “Co-seismic offsets due to two earthquakes (M w 6.1) along the Sumatran fault system derived from GNSS measurements”. In: *Earth, Planets and Space* 68.1, p. 57.

Jarrard, Richard D (1986). “Relations among subduction parameters”. In: *Reviews of Geophysics* 24.2, pp. 217–284.

Jiang, Yan et al. (2012). “Slow slip events in Costa Rica detected by continuous GPS observations, 2002–2011”. In: *Geochemistry, Geophysics, Geosystems* 13.4.

Johnson, Kaj M, Roland Bürgmann, and Jeffrey T Freymueller (2009). "Coupled afterslip and viscoelastic flow following the 2002 Denali Fault, Alaska earthquake". In: *Geophysical Journal International* 176.3, pp. 670–682.

Jónsson, Sigurjón et al. (2002). "Fault slip distribution of the 1999 M w 7.1 Hector Mine, California, earthquake, estimated from satellite radar and GPS measurements". In: *Bulletin of the Seismological Society of America* 92.4, pp. 1377–1389.

Jonsson, Sigurjon et al. (2003). "Post-earthquake ground movements correlated to pore-pressure transients". In: *Nature* 424.6945, p. 179.

Kanamori, Hiroo and Don L Anderson (1975). "Theoretical basis of some empirical relations in seismology". In: *Bulletin of the seismological society of America* 65.5, pp. 1073–1095.

Kanamori, Hiroo and Masayuki Kikuchi (1993). "The 1992 Nicaragua earthquake: a slow tsunami earthquake associated with subducted sediments". In: *Nature* 361.6414, p. 714.

Kaneko, Yoshihiro, Jean-Philippe Avouac, and Nadia Lapusta (2010). "Towards inferring earthquake patterns from geodetic observations of interseismic coupling". In: *Nature Geoscience* 3.5, p. 363.

Kasahara, Keichi (1981). *Earthquake mechanics*. Cambridge university press.

Kato, Aitaro et al. (2012). "Propagation of slow slip leading up to the 2011 Mw 9.0 Tohoku-Oki earthquake". In: *Science*, p. 1215141.

Kato, Naoyuki (2007). "Expansion of aftershock areas caused by propagating post-seismic sliding". In: *Geophysical Journal International* 168.2, pp. 797–808.

Khazai, Bijan and James E Daniell (2011). "The march 2011 Japan earthquake". In: *Institut für Technikfolgen-abschätzung und Systemanalyse*, p. 22.

Khazaradze, G et al. (2002). "Prolonged post-seismic deformation of the 1960 great Chile earthquake and implications for mantle rheology". In: *Geophysical Research Letters* 29.22, pp. 7–1.

Kimberlain, Todd B (2014). "The 2013 Eastern North Pacific hurricane season: Mexico takes the brunt". In: *Weatherwise* 67.3, pp. 35–42.

King, Geoffrey CP, Ross S Stein, and Jian Lin (1994). "Static stress changes and the triggering of earthquakes". In: *Bulletin of the Seismological Society of America* 84.3, pp. 935–953.

Kobayashi, Daisuke et al. (2014). “Kinematics of the western Caribbean: Collision of the Cocos Ridge and upper plate deformation”. In: *Geochemistry, Geophysics, Geosystems* 15.5, pp. 1671–1683.

Kyriakopoulos, C and AV Newman (2016). “Structural asperity focusing locking and earthquake slip along the Nicoya megathrust, Costa Rica”. In: *Journal of Geophysical Research: Solid Earth* 121.7, pp. 5461–5476.

Kyriakopoulos, C et al. (2015). “A new seismically constrained subduction interface model for Central America”. In: *Journal of Geophysical Research: Solid Earth* 120.8, pp. 5535–5548.

LaFemina, Peter et al. (2009). “Fore-arc motion and Cocos Ridge collision in Central America”. In: *Geochemistry, Geophysics, Geosystems* 10.5.

Lange, Dietrich et al. (2014). “Comparison of postseismic afterslip models with aftershock seismicity for three subduction-zone earthquakes: Nias 2005, Maule 2010 and Tohoku 2011”. In: *Geophysical Journal International* 199.2, pp. 784–799.

Lay, Thorne et al. (2005). “The great Sumatra-Andaman earthquake of 26 december 2004”. In: *Science* 308.5725, pp. 1127–1133.

Lay, Thorne et al. (2011). “Possible large near-trench slip during the 2011 M w 9.0 off the Pacific coast of Tohoku Earthquake”. In: *Earth, planets and space* 63.7, p. 32.

Lay, Thorne et al. (2012). “Depth-varying rupture properties of subduction zone megathrust faults”. In: *Journal of Geophysical Research: Solid Earth* 117.B4.

Letellier, Thierry (2005). “Etude des ondes de marée sur les plateaux continentaux”. PhD thesis. Toulouse 3.

Lin, Jian and Andrew M Freed (2004). “Time-dependent viscoelastic stress transfer and earthquake triggering”. In: *Environment, Natural Hazards, and Global Tectonics of the Earth* 2, pp. 21–38.

Liu, Chengli et al. (2015). “Rupture processes of the 2012 September 5 M w 7.6 Nicoya, Costa Rica earthquake constrained by improved geodetic and seismological observations”. In: *Geophysical Journal International* 203.1, pp. 175–183.

Liu-Zeng, Jing, Thomas Heaton, and Christopher DiCaprio (2005). “The effect of slip variability on earthquake slip-length scaling”. In: *Geophysical Journal International* 162.3, pp. 841–849.

Lundgren, Paul et al. (1999). “Seismic cycle and plate margin deformation in Costa Rica: GPS observations from 1994 to 1997”. In: *Journal of Geophysical Research: Solid Earth* 104.B12, pp. 28915–28926.

Lupi, M, Florian Fuchs, and Javier F Pacheco (2014). “Fault reactivation due to the M7. 6 Nicoya earthquake at the Turrialba-Irazú volcanic complex, Costa Rica: Effects of dynamic stress triggering”. In: *Geophysical Research Letters* 41.12, pp. 4142–4148.

Malservisi, Rocco et al. (2015). “Multiscale postseismic behavior on a megathrust: The 2012 Nicoya earthquake, Costa Rica”. In: *Geochemistry, Geophysics, Geosystems* 16.6, pp. 1848–1864.

Marone, Chris J, CH Scholtz, and Roger Bilham (1991). “On the mechanics of earthquake afterslip”. In: *Journal of Geophysical Research: Solid Earth* 96.B5, pp. 8441–8452.

Marquardt, Donald W (1963). “An algorithm for least-squares estimation of nonlinear parameters”. In: *Journal of the society for Industrial and Applied Mathematics* 11.2, pp. 431–441.

Marshall, Jeffrey S and Robert S Anderson (1995). “Quaternary uplift and seismic cycle deformation, Peninsula de Nicoya, Costa Rica”. In: *Geological Society of America Bulletin* 107.4, pp. 463–473.

Marshall, Jeffrey S, Donald M Fisher, and Thomas W Gardner (2000). “Central Costa Rica deformed belt: Kinematics of diffuse faulting across the western Panama block”. In: *Tectonics* 19.3, pp. 468–492.

Matsubara, Makoto, Yuji Yagi, and Kazushige Obara (2005). “Plate boundary slip associated with the 2003 Off-Tokachi earthquake based on small repeating earthquake data”. In: *Geophysical Research Letters* 32.8.

Matsuzawa, Toru et al. (2004). “Repeating earthquakes and quasi-static slip on the plate boundary east off northern Honshu, Japan”. In: *Earth, planets and space* 56.8, pp. 803–811.

McCaffrey, Robert (1992). “Oblique plate convergence, slip vectors, and forearc deformation”. In: *Journal of Geophysical Research: Solid Earth* 97.B6, pp. 8905–8915.

McCaffrey, Robert (2008). “Global frequency of magnitude 9 earthquakes”. In: *Geology* 36.3, pp. 263–266.

McCaffrey, Robert, S Stein, and J Freymueller (2002). “Crustal block rotations and plate coupling”. In: *Plate Boundary Zones, Geodyn. Ser* 30, pp. 101–122.

Meltzner, Aron J et al. (2015). “Time-varying interseismic strain rates and similar seismic ruptures on the Nias–Simeulue patch of the Sunda megathrust”. In: *Quaternary Science Reviews* 122, pp. 258–281.

Meng, Xiaofeng, Zhigang Peng, and Jeanne L Hardebeck (2013). “Seismicity around Parkfield correlates with static shear stress changes following the 2003 Mw6. 5 San Simeon earthquake”. In: *Journal of Geophysical Research: Solid Earth* 118.7, pp. 3576–3591.

Meng, Xiaofeng et al. (2012). “Detecting earthquakes around Salton Sea following the 2010 Mw 7. 2 El Mayor-Cucapah earthquake using GPU parallel computing”. In: *Procedia Computer Science* 9, pp. 937–946.

Menke, William (1989). *Geophysical data analysis: Discrete inverse theory*. Academic press.

Montero, Walter, Jonathan C Lewis, and Maria Cristina Araya (2017). “The Guanacaste volcanic arc sliver of northwestern Costa Rica”. In: *Scientific reports* 7.1, p. 1797.

Moore-Driskell, Melissa et al. (2013). “Integration of arrival-time datasets for consistent quality control: A case study of amphibious experiments along the Middle America Trench”. In: *Bulletin of the Seismological Society of America* 103.5, pp. 2752–2766.

Nadeau, Robert M and Thomas V McEvilly (1999). “Fault slip rates at depth from recurrence intervals of repeating microearthquakes”. In: *Science* 285.5428, pp. 718–721.

Nanjo, KZ et al. (2012). “Decade-scale decrease in b value prior to the M9-class 2011 Tohoku and 2004 Sumatra quakes”. In: *Geophysical Research Letters* 39.20.

Newman, Andrew V et al. (2002). “Along-strike variability in the seismogenic zone below Nicoya Peninsula, Costa Rica”. In: *Geophysical Research Letters* 29.20, pp. 38–1.

Nishenko, Stuart P (1991). *Circum-Pacific seismic potential: 1989–1999*. Springer.

Norabuena, Edmundo et al. (2004). “Geodetic and seismic constraints on some seismogenic zone processes in Costa Rica”. In: *Journal of Geophysical Research: Solid Earth* 109.B11.

Nuannin, Paiboon, Ota Kulhanek, and Leif Persson (2005). “Spatial and temporal b value anomalies preceding the devastating off coast of NW Sumatra earthquake of December 26, 2004”. In: *Geophysical research letters* 32.11.

Obara, Kazushige (2002). “Nonvolcanic deep tremor associated with subduction in southwest Japan”. In: *Science* 296.5573, pp. 1679–1681.

Okada, Yoshimitsu (1985). “Surface deformation due to shear and tensile faults in a half-space”. In: *Bulletin of the seismological society of America* 75.4, pp. 1135–1154.

Omori, Fusakichi (1895). “On the after-shocks of earthquakes”. In:

Outerbridge, Kimberly C et al. (2010). “A tremor and slip event on the Cocos-Caribbean subduction zone as measured by a global positioning system (GPS) and seismic network on the Nicoya Peninsula, Costa Rica”. In: *Journal of Geophysical Research: Solid Earth* 115.B10.

Ozawa, Shinzaburo et al. (2011). “Coseismic and postseismic slip of the 2011 magnitude-9 Tohoku-Oki earthquake”. In: *Nature* 475.7356, p. 373.

Pedrozo-Acuña, Adrián, J Agustín Breña-Naranjo, and Ramón Domínguez-Mora (2014). “The hydrological setting of the 2013 floods in Mexico”. In: *Weather* 69.11, pp. 295–302.

Peltzer, Gilles et al. (1998). “Poroelastic rebound along the Landers 1992 earthquake surface rupture”. In: *Journal of Geophysical Research* 103.B12, pp. 30131–30145.

Peng, Zhigang and Yehuda Ben-Zion (2005). “Spatiotemporal variations of crustal anisotropy from similar events in aftershocks of the 1999 M 7.4 Izmit and M 7.1 Düzce, Turkey, earthquake sequences”. In: *Geophysical Journal International* 160.3, pp. 1027–1043.

Peng, Zhigang and Joan Gomberg (2010). “An integrated perspective of the continuum between earthquakes and slow-slip phenomena”. In: *Nature geoscience* 3.9, p. 599.

Peng, Zhigang and Peng Zhao (2009). “Migration of early aftershocks following the 2004 Parkfield earthquake”. In: *Nature Geoscience* 2.12, p. 877.

Perfettini, H and J-P Avouac (2007). “Modeling afterslip and aftershocks following the 1992 Landers earthquake”. In: *Journal of Geophysical Research: Solid Earth* 112.B7.

Plümper, Thomas, Alejandro Quiroz Flores, and Eric Neumayer (2017). “The double-edged sword of learning from disasters: Mortality in the Tohoku tsunami”. In: *Global environmental change* 44, pp. 49–56.

Press, William H et al. (1986). *Numerical recipes: the art of scientific computing, 818 pp*.

Protti, M, F Güendel, and E Malavassi (2001). “Evaluación del potencial sísmico de la Península de Nicoya: Heredia”. In: *Costa Rica, Editorial Fundación UNA*.

Protti, Marino et al. (1995). “The March 25, 1990 (Mw= 7.0, ML= 6.8), earthquake at the entrance of the Nicoya Gulf, Costa Rica: Its prior activity, foreshocks, aftershocks,

and triggered seismicity". In: *Journal of Geophysical Research: Solid Earth* 100.B10, pp. 20345–20358.

Protti, Marino et al. (2014). "Nicoya earthquake rupture anticipated by geodetic measurement of the locked plate interface". In: *Nature Geoscience* 7.2, p. 117.

Radiguet, M et al. (2016). "Triggering of the 2014 M w 7.3 Papanoa earthquake by a slow slip event in Guerrero, Mexico". In: *Nature Geoscience* 9.11, p. 829.

Reid, Harry Fielding (1911). "The elastic-rebound theory of earthquakes." In: *Univ. Calif. Publ.. Bull. Dept. Geol.* 6.19, pp. 413–444.

Remy, Dominique et al. (2016). "Postseismic relocking of the subduction megathrust following the 2007 Pisco, Peru, earthquake". In: *Journal of Geophysical Research: Solid Earth* 121.5, pp. 3978–3995.

Ruegg, JC et al. (2009). "Interseismic strain accumulation measured by GPS in the seismic gap between Constitución and Concepción in Chile". In: *Physics of the Earth and Planetary Interiors* 175.1-2, pp. 78–85.

Ruina, Andy (1983). "Slip instability and state variable friction laws". In: *Journal of Geophysical Research: Solid Earth* 88.B12, pp. 10359–10370.

Ryan, William BF et al. (2009). "Global multi-resolution topography synthesis". In: *Geochemistry, Geophysics, Geosystems* 10.3.

Sak, Peter B et al. (2009). "Rough crust subduction, forearc kinematics, and Quaternary uplift rates, Costa Rican segment of the Middle American Trench". In: *Geological Society of America Bulletin* 121.7-8, pp. 992–1012.

Sandwell, David T and Paul Wessel (2016). "Interpolation of 2-D vector data using constraints from elasticity". In: *Geophysical Research Letters* 43.20.

Satake, Kenji et al. (1993). "Tsunami field survey of the 1992 Nicaragua earthquake". In: *Eos, Transactions American Geophysical Union* 74.13, pp. 145–157.

Savage, JC (1983). "A dislocation model of strain accumulation and release at a subduction zone". In: *Journal of Geophysical Research: Solid Earth* 88.B6, pp. 4984–4996.

Scholz, Christopher H (1998). "Earthquakes and friction laws". In: *Nature* 391.6662, p. 37.

Scholz, Christopher H (2015). "On the stress dependence of the earthquake b value". In: *Geophysical Research Letters* 42.5, pp. 1399–1402.

Schorlemmer, Danijel, Stefan Wiemer, and Max Wyss (2005). "Variations in earthquake-size distribution across different stress regimes". In: *Nature* 437.7058, p. 539.

Schurr, Bernd et al. (2014). "Gradual unlocking of plate boundary controlled initiation of the 2014 Iquique earthquake". In: *Nature* 512.7514, p. 299.

Schwartz, Susan Y and Juliana M Rokosky (2007). "Slow slip events and seismic tremor at circum-Pacific subduction zones". In: *Reviews of Geophysics* 45.3.

Shaddox, HR et al. (2017). "Spatiotemporal Relationship between Shallow Slow Slip and Repeating Earthquakes in the Northern Hikurangi Subduction Margin, New Zealand". In: *AGU Fall Meeting Abstracts*.

Shelly, David R et al. (2006). "Low-frequency earthquakes in Shikoku, Japan, and their relationship to episodic tremor and slip". In: *Nature* 442.7099, p. 188.

Steacy, Sandy et al. (2013). "A new hybrid Coulomb/statistical model for forecasting aftershock rates". In: *Geophysical Journal International* 196.2, pp. 918–923.

Stein, Seth and Michael Wysession (2003). *An introduction to seismology, earthquakes, and earth structure*. John Wiley & Sons.

Sun, Tianhaozhe et al. (2014). "Prevalence of viscoelastic relaxation after the 2011 Tohoku-oki earthquake". In: *Nature* 514.7520, p. 84.

Sun, Tianhaozhe et al. (2017). "Trench-breaching afterslip following deeper coseismic slip of the 2012 M w 7.6 Costa Rica earthquake constrained by near-trench pressure and land-based geodetic observations". In: *Earth and Planetary Science Letters* 479, pp. 263–272.

Synolakis, Costas E and Eddie N Bernard (2006). "Tsunami science before and beyond Boxing Day 2004". In: *Philosophical Transactions of the Royal Society of London A: Mathematical, Physical and Engineering Sciences* 364.1845, pp. 2231–2265.

Tarantola, Albert (1986). "A strategy for nonlinear elastic inversion of seismic reflection data". In: *Geophysics* 51.10, pp. 1893–1903.

Taylor, Waldo and Henriette Bakkar (2016). *La sismicidad del 2015 en los alrededores de los proyectos de generación eléctrica ARCOSA y Tejona (Guanacaste)*. Tech. rep. Instituto Costarricense de Electricidad.

Toda, Shingi et al. (2011). *Coulomb 3.3 graphic-rich deformation and stress-change software for earthquake, tectonic, and volcano research and teaching-user guide*. Tech. rep. US Geological Survey.

Toda, Shinji, Jian Lin, and Ross S Stein (2011). "Using the 2011 M w 9.0 off the Pacific coast of Tohoku Earthquake to test the Coulomb stress triggering hypothesis and to calculate faults brought closer to failure". In: *Earth, planets and space* 63.7, p. 39.

Toda, Shinji and Ross S Stein (2000). "Did stress triggering cause the large off-fault aftershocks of the 25 March 1998 Mw= 8.1 Antarctic Plate earthquake?" In: *Geophysical Research Letters* 27.15, pp. 2301–2304.

Todd, Erin K. (2017). "Interplay between modes of strain release along the shallow northern Hikurangi subduction zone, New Zealand". PhD thesis. University of California Santa Cruz.

Tormann, Thessa et al. (2015). "Randomness of megathrust earthquakes implied by rapid stress recovery after the Japan earthquake". In: *Nature Geoscience* 8.2, p. 152.

Towns, John et al. (2014). "XSEDE: accelerating scientific discovery". In: *Computing in Science & Engineering* 16.5, pp. 62–74.

Uchida, Naoki and Roland Bürgmann (2019). "Repeating Earthquakes". In: *Annual Review of Earth and Planetary Sciences* 47.

Uchida, Naoki and Toru Matsuzawa (2013). "Pre-and postseismic slow slip surrounding the 2011 Tohoku-oki earthquake rupture". In: *Earth and Planetary Science Letters* 374, pp. 81–91.

Uchida, Naoki et al. (2004). "Pre-and post-seismic slow slip on the plate boundary off Sanriku, NE Japan associated with three interplate earthquakes as estimated from small repeating earthquake data". In: *Tectonophysics* 385.1-4, pp. 1–15.

Utsu, Tokuji (1970). "Aftershocks and earthquake statistics (1): Some parameters which characterize an aftershock sequence and their interrelations". In: *Journal of the Faculty of Science, Hokkaido University. Series 7, Geophysics* 3.3, pp. 129–195.

Vannucchi, Paola et al. (2001). "Tectonic erosion and consequent collapse of the Pacific margin of Costa Rica: Combined implications from ODP Leg 170, seismic offshore data, and regional geology of the Nicoya Peninsula". In: *Tectonics* 20.5, pp. 649–668.

Voss, N et al. (2018). "Do slow slip events trigger large and great megathrust earthquakes?" In: *Science advances* 4.10, eaat8472.

Voss, Nicholas K et al. (2017). "Slow slip events in the early part of the earthquake cycle". In: *Journal of Geophysical Research: Solid Earth* 122.8, pp. 6773–6786.

Waldhauser, Felix and William L Ellsworth (2000). "A double-difference earthquake location algorithm: Method and application to the northern Hayward fault, California". In: *Bulletin of the Seismological Society of America* 90.6, pp. 1353–1368.

Walter, Jacob I et al. (2011). "Persistent tremor within the northern Costa Rica seismogenic zone". In: *Geophysical Research Letters* 38.1.

Walter, Jacob I et al. (2013). "The synchronous occurrence of shallow tremor and very low frequency earthquakes offshore of the Nicoya Peninsula, Costa Rica". In: *Geophysical Research Letters* 40.8, pp. 1517–1522.

Walter, Jacob I et al. (2015). "Far-field triggering of foreshocks near the nucleation zone of the 5 September 2012 (M W 7.6) Nicoya Peninsula, Costa Rica earthquake". In: *Earth and Planetary Science Letters* 431, pp. 75–86.

Walther, Christian HE (2003). "The crustal structure of the Cocos ridge off Costa Rica". In: *Journal of Geophysical Research: Solid Earth* 108.B3.

Wang, Kelin and Susan L Bilek (2011). "Do subducting seamounts generate or stop large earthquakes?" In: *Geology* 39.9, pp. 819–822.

Wang, Kelin, Yan Hu, and Jiangheng He (2012). "Deformation cycles of subduction earthquakes in a viscoelastic Earth". In: *Nature* 484.7394, p. 327.

Wang, Kelin and Anne M Tréhu (2016). "Invited review paper: Some outstanding issues in the study of great megathrust earthquakes—The Cascadia example". In: *Journal of Geodynamics* 98, pp. 1–18.

Wang, Kelin et al. (2007). "Crustal motion in the zone of the 1960 Chile earthquake: Detangling earthquake-cycle deformation and forearc-sliver translation". In: *Geochemistry, Geophysics, Geosystems* 8.10.

Waylen, Peter R and Michael Harrison (2005). "The coincidence of daily rainfall events in Liberia, Costa Rica and tropical cyclones in the Caribbean basin". In: *International journal of climatology* 25.12, pp. 1665–1674.

Wells, Donald L and Kevin J Coppersmith (1994). "New empirical relationships among magnitude, rupture length, rupture width, rupture area, and surface displacement". In: *Bulletin of the seismological Society of America* 84.4, pp. 974–1002.

Wessel, Paul et al. (2013). "Generic mapping tools: improved version released". In: *Eos, Transactions American Geophysical Union* 94.45, pp. 409–410.

Weston, J and M Shirzaei (2016). "Combining GPS and repeating earthquakes for a high resolution analysis of subduction zone coupling". In: *Tectonophysics* 667, pp. 37–47.

Wiemer, Stefan, Stephen R McNutt, and Max Wyss (1998). "Temporal and three-dimensional spatial analyses of the frequency-magnitude distribution near Long Valley Caldera, California". In: *Geophysical Journal International* 134, pp. 409–421.

Wiemer, Stefan and Max Wyss (2002). "Mapping spatial variability of the frequency-magnitude distribution of earthquakes". In: 45, pp. 259–V.

Williamson, Amy L and Andrew V Newman (2018). "Limitations of the Resolvability of Finite-Fault Models Using Static Land-Based Geodesy and Open-Ocean Tsunami Waveforms". In: *Journal of Geophysical Research: Solid Earth* 123.10, pp. 9033–9048.

Wyss, Max (1973). "Towards a physical understanding of the earthquake frequency distribution". In: *Geophysical Journal of the Royal Astronomical Society* 31.4, pp. 341–359.

Wyss, Max (2018). "Rural Populations Suffer Most in Great Earthquakes". In: *Seismological Research Letters*.

Yao, Dongdong et al. (2017). "Detailed spatiotemporal evolution of microseismicity and repeating earthquakes following the 2012 Mw 7.6 Nicoya earthquake". In: *Journal of Geophysical Research: Solid Earth* 122.1, pp. 524–542.

Yue, Han et al. (2013). "The 5 September 2012 Nicoya, Costa Rica Mw 7.6 earthquake rupture process from joint inversion of high-rate GPS, strong-motion, and teleseismic P wave data and its relationship to adjacent plate boundary interface properties". In: *Journal of Geophysical Research: Solid Earth* 118.10, pp. 5453–5466.

Zhang, Haijiang and Clifford H Thurber (2003). "Double-difference tomography: The method and its application to the Hayward fault, California". In: *Bulletin of the Seismological Society of America* 93.5, pp. 1875–1889.

Zheng, Yong et al. (2012). "5Hz GPS seismology of the El Mayor—Cucapah earthquake: estimating the earthquake focal mechanism". In: *Geophysical Journal International* 190.3, pp. 1723–1732.

VITA

Tiegan E. Hobbs was born in North Bay, Ontario. Having lived in Vancouver, British Columbia; Ottawa, Ontario; Montreal, Quebec; and Victoria, British Columbia, she currently lives in Atlanta, Georgia. For the past 5 years Tiegan has been pursuing her doctorate in geophysics, concurrently with a Master's degree in Civil Engineering. During that time she has had the opportunity to complete field work in Costa Rica, Alaska, and Antarctica. Previously, she completed a Master's degree in geophysics from the University of Victoria and a Bachelor's degree in Geology at McGill University. Following completion of her time at Georgia Institute of Technology, Tiegan will be starting a position as a postdoctoral researcher with Natural Resources Canada. There she will be assessing earthquake risk for the West Coast of Canada.

While at Georgia Tech, Tiegan was actively involved in her Department. She co-founded the Graduates in Earth and Atmospheric Sciences (EAS) Student Council, on which she served as Vice President, Chair of First Year Mentoring, and Social Chair. She also served as Science Coordinator for the EAS Graduate Student Symposium, and helped organize the EAS Science Showcase at the Ponce City Farmers Market. She was an instructor and leader for the Kids Interested In Discovering Science Club at Georgia Tech, and continues to volunteer with the Skype a Scientist program. Tiegan has also served as a freelance science writer for `http://temblor.net`, and completed training as a science communicator.

In her spare time, Tiegan enjoys endurance sports, eating mac and cheese, and going to the park with her dog, Ranger.